# The interaction of oxygen with clean and Cs predosed polycrystalline silver : an XPS-study

Hogenboom, E.H.M.

*Award date:*
1986

# The interaction of oxygen with clean and Cs predosed polycrystalline silver: an XPS-study.

E.H.M. Hogenboom

Report on a study performed during
september 1985 to september 1986 at
the Koninklijke/Shell Laboratorium, Amsterdam.

"Do not postpone till tomorrow what you
can measure today."
Variation on Murphy's law.

I am greatly endebted to Dr. H.P.C.E. Kuipers for correcting the physics and Dr. G.R. Hays for correcting the English in this report. I thank the Koninklijke/Shell Laboratorium for giving me the opportunity to perform this interesting study in their laboratory.

List of contents.

SUMMARY.

We report on an XPS study of the interaction of oxygen with clean and Cs predosed polycrystalline silver. This interaction is of major importance in catalytic research because of the uniqueness of silver as a catalyst in the epoxidation of ethene.

We identified three distinct adsorbed oxygen species on the clean silver surface after oxygen exposure. A carbonate surface species developed readily after exposing the silver to oxygen at room temperature at pressures in the range $10^{-6}$ to 10 Pa. It was characterized by an O1s binding energy of 530.0 eV, FWHM 2.0 eV and a C1s binding energy of 287.5 eV, FWHM 2.0 eV.

By activating the gas phase oxygen by means of a hot filament in line of sight with the silver sample we could generate atomic oxygen on the silver surface, characterized by an O1s binding energy of 528.4 eV, FWHM 2.0 eV. This species was reactive towards CO.

Activated oxygen exposures at elevated temperatures were always accompanied by a third form of adsorbed oxygen. It is an embedded species, termed subsurface oxygen. It was characterized by an O1s binding energy of 530.6 eV, and a somewhat larger FWHM of 3.0 eV. Elevated temperatures seem to be a prerequisite for its formation. Subsurface oxygen was also found without activating the gas phase oxygen after prolonged oxygen exposure at high pressure (500 Pa) and elevated temperature (475 K).

Investigations on pure Cs layers on the silver surface were precluded by unwanted oxygen uptake during Cs deposition. The Cs richest adlayer obtained had a stoichiometry Cs : O ≈ 2.5 : 1. The deposited mixed Cs-O layer is shown to develop as lumps on the silver surface. Upon oxidation of the Cs adlayers, the C3sd binding energy decreases from 539.5 eV to 538.2 eV, explained by an enhanced relaxation of the created Cs3d core hole. From the Cs3d intensity increase following an oxygen exposure we concluded that a spreading out of the originally present Cs-O lumps took place. At least two different oxygen species could be discerned on a Cs dosed silver surface.

The first species, responsible for the large decrease in Cs3d binding energy developed in the beginning of the oxygen exposure and is thought to be associated with an oxygen species in the direct vicinity of the Cs. It is characterized by an O1s binding energy of 530.6±0.4 eV.

The second species is characterized by an O1s binding energy of 528.6 eV and reactive to CO. It is assigned to atomic oxygen, simular to the species adsorbed at the clean silver surface. It was found only after Cs : O stoichiometries exceeding 1 : 3. A more detailed characterization of the oxygen species on the Cs dosed surface clearly requires more than one surface analysis technique.

The last decade has seen a tremendous growth of investigations concerning the surface region of solids, not in the least because of their importance in industry (corrosion, catalysis, thin-layer techniques etc.). The surface region of solids is considered here as the outermost atomic layers of the solid, comprising the first nm in the solid from the solid-gas interface. The part of science which tries to understand phenomena at surfaces (and interfaces) is appropiately called "surface science" and is a rapidly expanding field.

In this report a study is made of the interaction of oxygen and caesium with a polycrystalline silver surface. This interaction is of importance for industrial catalysis in the epoxidation reaction of ethene for which silver is a unique catalyst. The epoxidation reaction is stimulated by the presence of a silver catalyst on which's surface the epoxidation reactions take place. Total combustion of ethene to CO2 and H2O is thermodynamically favoured and is a side reaction which obviously has to be suppressed:

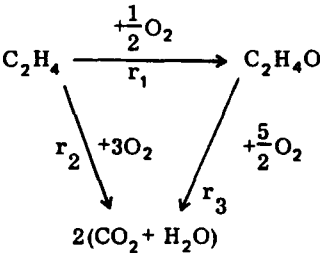


The catalyst consists of an alumina (Al2O3) carrier with a rather low specific surface area (ca. 1 $m^2/g$) over which silver particles are dispersed. The catalytic effect of silver is due to the formation of silver-oxygen complexes at the silver surface which stimulate the formation of ethene-oxide and less the combustion to CO2 and H2O. The uniqueness of silver as a catalyst is attributed to the strength of the silver-oxygen bond which appears to be just strong enough to cover the silver surface with reasonable amounts adsorbates but not so strong as to inhibit its catalytic working ("vulcano curve" of catalytic activity). The selectivity of the catalyst, defined as the percentage of the ethene originally present which is transformed into ethene-oxide, is improved by doping the silver with alkali-metals (promoters) and chlorine (inhibitor).

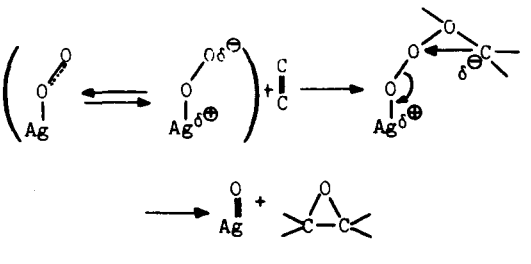

Figure 1.1: Proposed model for the epoxidation of ethene on a silver surface.

Ethene-oxide is produced in enormous quantities: the world production in 1980 totalled ca. 7 Mton. It is a versatile petrochemical which serves as

a building unit for products as diverse as detergents, synthetic fibres and paint solvents. In view of the large ethene-oxide turnover it is not surprising that a considerable effort has been spent to maximize the selectivity of the silver catalyst employed. However, the mechanism of selective ethene epoxidation and the role of the co-adsorbates in it remains as yet not completely unravelled. The improvement of the catalyst is still more or less a matter of trial and error. Hitherto, selectivities up to 80-83% have been achieved.

A number of methods have been employed to gain more insight in the two-dimensional chemistry which takes place at the silver surface, including in situ measurements as for instance with infrared spectroscopy and measurements with surface analysis techniques (like LEED, TDS, XPS) on well defined systems (single crystals) in ultra high vacuum systems (pressures below $10^{-8}$ Pa).

The usefulness of experiments on well defined systems under conditions far away from those in industrial epoxidation is exemplified by the Sachtler model for ethene epoxidation /1/ depicted in figure 1.1. In this model the entity responsible for the epoxidation reaction is molecular oxygen in a head-on configuration bound to the silver surface. The outermost silver atom of the adsorbed molecule reacts with $C_2H_4$ to $C_2H_4O$ whereas the remaining mono-atomic species is responsible for the combustion to $CO_2$ and $H_2O$. From simple stoichiometric reasoning it follows that the maximal achievable selectivity in this case is 6/7 or 85.7%.

If this model were true, commercially it would not be of great importance trying to improve the 83% selective catalyst. Thus the proposed mechanism has spurred investigations to a considerable effort to indentify molecular-oxygen-like species on a silver surface. In fact they were found with the help of modern surface analysis techniques on well defined silver systems.

However, since the introduction of the model, silver catalysts have been developed with initial selectivities exceeding 6/7. This stimulated research on the improvement of the silver catalyst. The Sachtler model clearly shows the implications that research conducted under ultra high vacuum conditions with modern surface analysis techniques may have on industrial processes which take place at pressures some 12 orders of magnitude larger.

In the rest of this report we are concerned with the interaction of oxygen with polycrystaline silver. The goal of the experiments was first to indentify the various oxygen species on the clean silver surface and secondly to study the co-adsorption layer oxygen/alkali/chlorine. We used XPS (X-ray Photo-electron Spectroscopy) to characterize the surface region. Because of experimental intricacies we were only able to study oxygen adsorption on clean silver and the oxygen/caesium co-adsorption layer within the limited time available.

Atoms at the surface of a solid exert an attractive force normal to the surface plane as a result of the sudden cut-off in the periodical arrangment at the solid-gas interface. Consequently, at this interface the concentration of molecules exceeds that in the gas phase, a proces called adsorption. This term has to be distinguished from absorption in which process the uptake of gas molecules is not restricted to the surface region.

Consider a gas consisting of molecules with mass m, at temperature T and pressure p. The rate of collisions dn/dt of gas molecules ($m^{-2}s^{-1}$) can be derived from kinetic gas theory to be:

$$(2.1) \qquad dn/dt = \frac{p}{\sqrt{2\pi mkT}}$$

If we assume that all collisions result in the accumulation of a gas molecule on the surface and the average number of surface atoms is ca. $10^{19}/m^2$, then the time t in which the whole surface is covered with adsorbed gas molecules is:

$$(2.2) \qquad t = 10^{19} / (dn/dt)$$

For simple gasses (e.g. oxygen) the whole surface will be covered within 1 second at a pressure of $10^{-6}$ Torr (1 Torr≈133 Pa). Thus it is not so surprising that a frequently used exposure unit in adsorption experiments is the Langmuir, 1 L=$10^{-6}$ Torrsec.

From this simple calculation it follows that the ambient partial pressures of background gasses in a well defined adsorption experiment must be orders of magnitude smaller than $10^{-6}$ Torr. Therefore all adsorption experiments and surface analysis studies should be performed under Ultra High Vacuum conditions (pressures < $10^{-10}$ Torr).

## 2.1: Physisorption and chemisorption.

Two types of adsorption may be discerned by the nature of the attractive forces in play: physisorption and chemisorption. In physisorption the adsorbate is held to the surface by van der Waals forces that arise from the interaction of fluctuating dipoles. The adsorbed molecules/atoms are polarized by the large electric field gradient at the metal surface. The interaction energy $\Delta W$ is proportional to $E\alpha^2$ with E the field strength and $\alpha$ the volume polarizability of the adatom. $\Delta W$ is small, in the order of 0.1 eV/atom, so substantial amounts are only adsorbed near or below the boiling point of the adsorbate.

In chemisorption charge transfer takes place between adsorbate and adsorbent. In fact, chemisorption may be considered as a chemical reaction between an adsorbate molecule and the surface array of metal atoms. We must stress that e.g. chemisorption of oxygen on a silver surface is not the same as e.g. formation of Ag2O: the latter is characterized by a three dimensional lattice, whereas the former only has a two dimensional periodicity. Chemisorption binding energies exceed those of physisorption and lie in the order of 0.5-4 eV/atom.

## 2.2: Dissociative and associative chemisorption.

Because of the strength of the chemisorption bond between atoms in a molecule and the adsorbent, the molecule may actually dissociate upon chemisorption. This is schematically depicted in figure 2.1. It envisages the one dimensional potential diagram of an oxygen molecule approaching a silver surface /2/. It suggests a shallow minimum caused by van der Waals type of physisorption O2,p (the socalled precursor state), a chemisorbed molecular oxygen state O2,a and a deeper minimum caused by the dissociative chemisorbed state Oa. It is evident that the molecule will dissociate at the intersection of the potential curves for the molecule and that for the two free atoms.

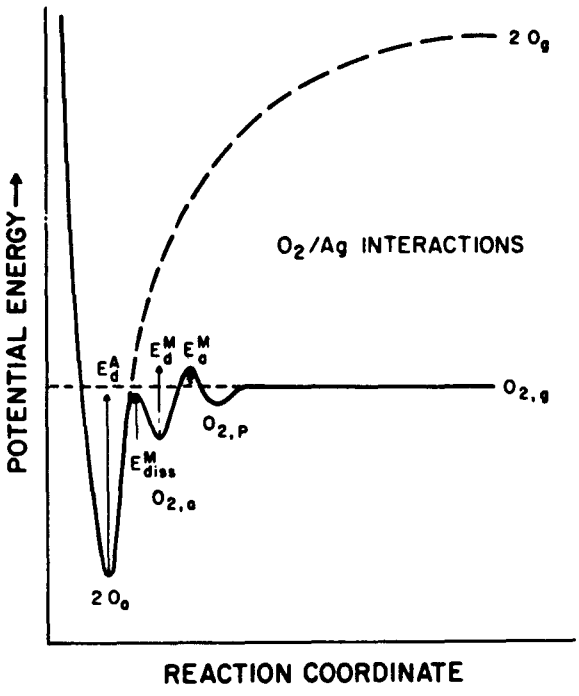


Figure 2.1: One-dimensional potential diagram for an oxygen molecule approaching a silver surface /2/.

The associative or dissociative adsorption of a di-atomic molecule depends on the adsorbate as well as the particular adsorbent and the surface temperature. For example, oxygen appears to adsorb dissociatively on most metals /3/. Molecular adsorption has been observed only on silver and platinum surfaces at low temperatures. This can be understood from figure 2.1. For most metals the dissociative adsorption heat of oxygen is so large that the cross-over point between the chemisorbed molecular and atomic state lies at sufficiently low energies to be surmounted by the admolecule. Thus all chemisorbed molecules will be immediately trapped in the chemisorbed mono-atomic state. At low temperatures only the physisorbed state will be populated as a result of the inaccessibility of the chemisorbed states because of the activation barrier.

## 2.3: Accommodation coefficent and sticking probability.

Of course there is only a finite probability that an impinging molecule will actually accumulate at the surface. It has to give up its transla-

tional energy normal to the surface plane. The probability that such a loss occurs is expressed in a so-called condensation coefficient. For most molecules on metals this coefficient approaches unity. It is the probability that the impinging molecule accommodates in the precursor state. The molecule may still be excited and desorb before being accommodated into a more strongly held chemisorption state. The ratio of finally trapped molecules to the initial amount of impinging molecules on the surface is termed sticking probability and will frequently be less than unity. For example the sticking probability of oxygen on silver lies in the order of $10^{-4}$ to $10^{-6}$, depending on the crytallographic orientation of the surface (possible explanations of this large spread in sticking probabilities of oxygen on silver will be given in chapter 4).

## 2.4: Adparticle mobility.

The depth of the chemisorption minimum depicted in figure 2.1 varies across the surface because the adatom "looks" at the surface on an atomic scale. For a perfect single crystal surface this variation is periodical, schematically depicted in figure 2.2. Adjacent potential minima are seperated by a diffusion barrier with height Edif. The residence time $\tau$ of the adparticle in a particular adsorption site is given by:

(2.3) $\tau = \tau_o \exp(Edes/kT)$

with $\tau_o$ the reciprocal vibration frequency ca. $10^{-13}$ s (see paragraph 2.9). The residence time $\tau'$ on the surface is given by:

(2.4) $\tau' = \tau_o \exp(Edif/kT)$

Since Edif is always at least a factor two smaller than Edes, $\tau$ is always much more smaller than $\tau'$ so the adparticle is able to diffuse over the surface.

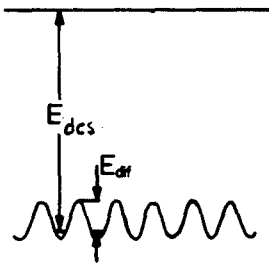


Figure 2.2: Variation of the surface potential. Edif is the activation energy for surface diffusion, Edes is the activation energy for desorption.

The mobility of the adspecies is determined by the ratio Edif/kT. If Edif>10kT the particle will be nearly immobile and trapped in the adsorption sites, if Edif<kT adparticles will move freely over the surface and can be thought of as a two dimensional gas. As a rule of thumb, the temperature at which adspecies become mobile can be taken as 2/3 of the desorption temperature.

## 2.5: Number of metal atoms involved in the chemisorption bond.

From the nature of bonding in metals it can be hardly imagined that a chemisorbed entity interacts with a single metal atom. In theoretical treatments it is common use to treat the chemisorption problem as the interaction between the adatom and a "jellium" metal model in which the metal is envisaged as a free electron gas with a uniform positive background potential to account for the positive nuclei. An example is the so-called local density functional formalism (LDF formalism) /4/.

The LDF theory reduces the many-electron problem for the ground state distribution $n(\vec{r})$ of a system of N electrons in a static external potential $V(\vec{r})$ due to adatom nucleus and positive "jellium" background to the self-consistent solution of the one-electron Schroedinger-like equation. The effective potential in this formalism is composed out of $V(\vec{r})$, an exchange correlation term and an electron-electron interaction term. To find a suitable expression for this effective potential which allows the Schroedinger equation to be solved is the challenge in this theoretical approach. Adatom binding energies, electronic screening charge distributions and adatom bond lengths can be calculated using LDF theory.

On the other hand only a limited number of metal atoms is believed to take part in the chemisorption bond. This justifies another theoretical approach namely the ab initio cluster calculations in which the adatom interacts with a small cluster of atoms (ca. 10 atoms) representing the adsorbent /4/. Adatom electron levels are calculated by performing a perturbation procedure on the original atomic levels of the element. To reduce the computational effort, clusters cannot be too large; usually less than 25 atoms are considered. The limited number of atoms in a cluster limits the accuracy of this theoretical approach. Cluster calculations allow for structural models of chemisorption in which the real substrate surface geometry can be approximated.

Theoretical modeling of chemisorption remains a difficult task. The theoretical description of the process of chemisorption is far behind the experimental characterisation of chemisorption systems. Therefore we will not review the vast collection of theoretical methods employed on different systems, the reader is referred to specialistic books in this field and references therein /4,5/.

## 2.6: The role of the crystallographic orientation of the substrate.

Because of the multi-atom configuration necessary to describe the nature of the chemisorption bond, the geometrical arangment of the substrate surface atoms must clearly have some influence on it. According to a simple picture the strength of the chemisorption bond would increase if the coordination number of the surface atoms decreases because of the larger number of 'unsaturated' valencies of the surface atom in the latter case. This would mean a lower adsorption energy on more densely packed planes relative to planes with lower Miller indices.

That this reasoning does not generally hold may be illustrated by the dissociation energies for an H atom from H2O and OH, being 50 and 43 eV respectively. Measurements of adsorption energies on various crystallographic planes of the same substrate show that the influence of the surface orientation on the energetics of chemisorption is small i.e. less than 20%. E.g. measured adsorption energies of oxygen on Ag(110) and Ag(111) are 42.5 kcal/mol and 39.9 kcal/mol respectively /2/.

However, there is a ramarkable effect on the kinetics of adsorption.For example the sticking probability of oxygen on silver(110) exceeds that of oxygen on silver(111) by two orders of magnitude.

## 2.7: Interactions between adparticles.

Since chemisorption always involves different species (namely adsorbent and adsorbate) a purely covalent bond will be exceptional and generally a dipole layer will be built up at the surface. The effective dipole moment $\mu$ (Cm) is related to the change in workfunction $\Delta\phi$ (J):

$$\Delta\phi = q\ Ns\ \mu/\varepsilon o \qquad (2.5)$$

with Ns the adparticle coverage ($m^{-2}$) and q the electron charge. Pairwise repulsive interactions between adsorbed particles will occur as a result of dipole-dipole repulsion. The interaction energy U is given by $U=\mu^2/\varepsilon o r^3$ /6/. Summation over all interacting dipoles per unit area within a uniform overlayer yields a total interaction energy per dipole W:

$$W = \tfrac{1}{2} K\ Ns^{3/2}\ \mu^2/\varepsilon o \qquad (2.6)$$

with K=9 depending only slightly on the geometrical arangment /5/. If we assume a $\Delta\phi$ of 1 eV and $Ns=10^{19}/m^2$ it follows that W=20 meV/adparticle compared to kT=25 meV at room temperature, so dipole-dipole interaction will not be a major interaction source. Furthermore, mutual screening at higher coverages will decrease dipole-dipole repulsion. Exceptional large $\Delta\phi$ values (3.5 eV) are encoutered in alkali adsorption in which case dipole-dipole repulsion may be of influence in the ordering of adparticles.

The direct interaction between adsorbates via orbital overlap depends on the orbital geometry and population but exhibits presumably characteristic features similar to those of gas phase particles /5/. These interactions are strongly repulsive on a short range scale and are described by the Lennard-Jones potential U(r):

$$U(r) = \alpha(ro/r)^{12} - \alpha(ro/r)^{6} \qquad (2.7)$$

with slightly adjusted parameters $\alpha$ and ro as compared to the gas phase. The direct interaction will eventually limit the maximum coverage ("hard sphere model") of adsorbates unless of course this limit is reached at lower values because of other long range interactions.

Because in the chemisorption of an adatom several metal atoms are involved, the adatom will modify its direct environment, that is neighbouring adsorption sites. In this way adparticles will interact indirectly by their bond with the metal surface. Modelling is more difficult /5/ but general results for different substrates are as follows:

- interactions may be repulsive as well as atractive.
- interaction energies are about one order of magnitude smaller than the binding energies involved.
- interaction strength decays rapidly within a few (2-3) lattice constants to values below kT.

In general, these indirect effects will be the major interaction source between adatoms on metals.

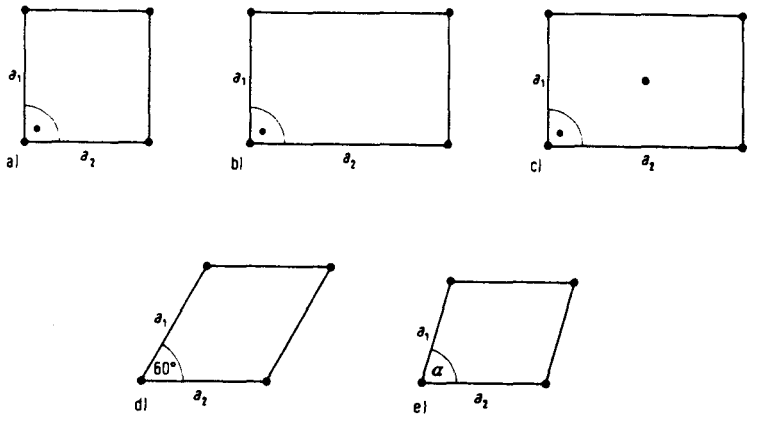


Figure 2.3: The five types of two-dimensional Bravais lattices
a) square $a_1 = a_2$, $\alpha = 90°$
b) primitive rectangular, $a_1 \neq a_2$, $\alpha = 90°$
c) centered rectangular, $a_1 \neq a_2$, $\alpha = 90°$
d) hexagonal, $a_1 = a_2$, $\alpha = 60°$
e) oblique, $a_1 \neq a_2$, $\alpha \neq 90°$

## 2.8: Ordered adlayers, LEED.

If we assume that the lattice of adsorption sites is indentical with the substrate lattice and the effective binding energy of an adsorbed particle is modified by a catch-all interaction potential $\phi(\vec{r})$ (which accounts for all interactions between adparticles e.g. as treated in paragraph 2.7) then the total energy E of the adparticles is described by:

$$(2.8) \qquad E = \sum_i b_i \varepsilon_i + \sum_{j=i} b_i b_j \phi(\vec{r}_i - \vec{r}_j)$$

with $\varepsilon_i$ the energy in adsorption site i, $b_i$ the occupation number of site i (0 or 1) and $(\vec{r}_i - \vec{r}_j)$ the distance between site i and site j. Because of the $\phi$ term the configuration with maximum entropy (random distribution) is no longer favoured and a long range order may occur.

This ordering yields valuable information about the nature of the particular surface bond. A most suitable technique for investigations concerning ordered adlayers is LEED (Low Energy Electron Diffraction). Because of its importance as a characterizational tool we will treat the technique here briefly. A more elaborate treatment is given e.g. by Ertl and Kueppers /7/.

In LEED the sample of interest is irradiated with electrons with kinetic energy of ca. 100 eV. The de Broglie wavelength of such electrons is in the order of 0.1 nm. Because interatomic seperations are of the same order of magnitude (0.2-0.4 nm), diffraction occurs at the periodical arangement of atoms in a single crystal surface. The diffraction pattern observed contains information on the arrangment of the scatterers, that is, about the surface atoms.

Periodic surface structures are classified into five two-dimensional Bravais lattices, depicted in figure 2.3. The relation between ordered adsorbate structures (basis vectors $\vec{b}_1, \vec{b}_2$) and the single crystal surface mesh (basis vectors $\vec{a}_1, \vec{a}_2$) is usually expressed as:

$$(2.9) \qquad (p,c)\ \left(\frac{|b_1|}{|a_1|} * \frac{|b_2|}{|a_2|}\right) R\phi$$

where "p" denotes aprimitive, "c" a centered unit cell and $\phi$ is the angle over which the adsorbate lattice is rotated with respect to the adsorbent's lattice. This notation, proposed by WOOD, is not completely general; it fails if the angle between $\vec{a}_1$ and $\vec{b}_1$ is different from that between $\vec{a}_2$ and $\vec{b}_2$. However, it is the most frequently encountered notation in LEED investigations and in most cases is sufficient to describe the ordered adsorbate structures.

Consider a surface with a unit cell formed by $\vec{a}_1, \vec{a}_2$, see figure 2.4. The impinging electron beam is denoted by the wavevector $\vec{k}$, the scattered beam by $\vec{k}'$. For constructive interference to occur between scattered beams stemming from adjacent scatterers, the two-dimensional Laue conditions have to be met:

$$(2.10) \qquad \begin{aligned} \vec{a}_1 \cdot \Delta\vec{k} &= h_1 \\ \vec{a}_2 \cdot \Delta\vec{k} &= h_2 \end{aligned} \qquad \Delta\vec{k} = \vec{k} - \vec{k}'\ ;\ h_{1,2} = 0,1,2,\ldots.$$

Now define the reciprocal lattice vectors $\vec{a}_i^*$ by:

$$(2.11) \qquad \vec{a}_i^* \cdot \vec{a}_j = \delta_{ij}$$

Then the directions $\Delta\vec{k}$ of interference maxima are determined by:

$$(2.12) \qquad \Delta\vec{k} = h_1\vec{a}_1^* + h_2\vec{a}_2^*$$

by definition. Thus the diffraction pattern is a direct reflection of the reciprocal lattice. The real space lattice may be easily constructed from this via equation 2.11.

In principle, a third Laue condition has to be fulfilled which contains the distance normal to the surface. If $\vec{a}_3$ denotes the periodicity in this third dimension and $\vec{k}'$ is perpendicular to the surface, this condition is:

$$(2.13) \qquad \tfrac{1}{2}\vec{a}_3 \cdot \Delta\vec{k} = h_3 \qquad h_3 = 1,2,3,\ldots.$$

However, because electrons with kinetic energies of ca. 100 eV have a very small inelastic mean free path (≈0.5 nm, that is why LEED is a surface sensitive technique) the contribution from deeper layers is small and restriction 2.13 can be relaxed. By varying the electron energy $\varepsilon$ (and with it, $\Delta\vec{k}$) maximal intensity I of the LEED spots is observed if equation

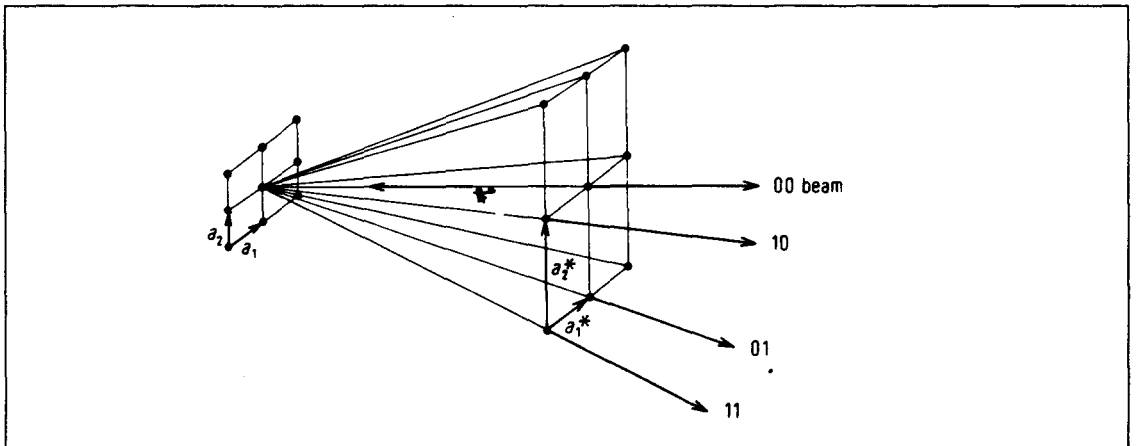


Figure 2.4: Formation of a LEED diffraction pattern.

2.13 is obeyed. Thus, I(ε) curves contain information about the position of the scatterer with respect to the layers underneath. In principle this position can be calculated (dynamical LEED calculations) but the procedure is not straightforward, and therefore mainly done by specialist groups.

## 2.9: Thermal desorption.

Desorption occurs when the adspecies acquire sufficient energy to escape from the surface. In figure 2.1 this activation energy for desorption is denoted Edes. This energy can be acquired by raising the surface temperature (thermal desorption), by irridiating the surface with particles of sufficient energy (electron-stimulated desorption, photo-desorption) or e.g. by applying a sufficiently strong external electrical field (field desorption). We will restrict ourselves to thermal desorption and treat TDS (Thermal Desorption Spectroscopy) briefly.

The desorption flux dNs/dt is straightforwardly described by:

$$(2.14) \qquad dNs/dt = Ns\ \nu\ \exp(\ -\ Edes/kT\ )$$

where Ns is again the number of adparticles per $m^2$, ν is the frequency factor of bond rupture, Edes is the activation energy for desorption and T is the surface temperature.

The desorption proces can be described in terms of a transition state complex in equilibrium with the adsorbed molecule. In the transition state, the complex vibrates along the reaction coordinate perpendicular to the surface with frequency νd. Since there is no restoring force, each vibration will result in desorption. ν can now be evaluated as:

$$(2.15) \qquad \nu = (F\#/Fa)\ \nu d$$

with F# and Fa being the complete partition functions of the transition state complex and adsorbed molecule respectively. If we separate the vibrational partition function:

$$(2.16) \qquad \frac{1}{1\ -\ \exp(-\ h\nu d/kT)}$$

from F# and approximate it by kT/hνd since νd is small, we obtain:

$$(2.17) \qquad \nu \simeq\ (kT/h)\ (G\#/Fa)$$

where G# is the partition function of the transition state complex without the vibrational mode. If further the internal degrees of freedom of complex and molecule are the same (usually the case for simple adsorbents) and νd for the adsorbed molecule is high (such that the vibrational partition function reduces to unity), G#/Fa = 1 and:

$$(2.18) \qquad \nu \simeq\ kT/h\ = 10^{13}/s$$

In Thermal Desorption Spectroscopy (TDS) the sample is heated at a constant rate β=dT/dt and the partial pressure P of expected gasses is monitored with a mass spectrometer while the vessel is pumped at a constant rate Ro. The following relations are obeyed:

$$(2.19) \qquad \begin{cases} dNs/dt = \beta\ dNs/dT = kd\ Ns \\ Ro(\ P(T)\ -\ P(To)\ ) = R'o\ P(T) = A\ kd\ Ns \end{cases}$$

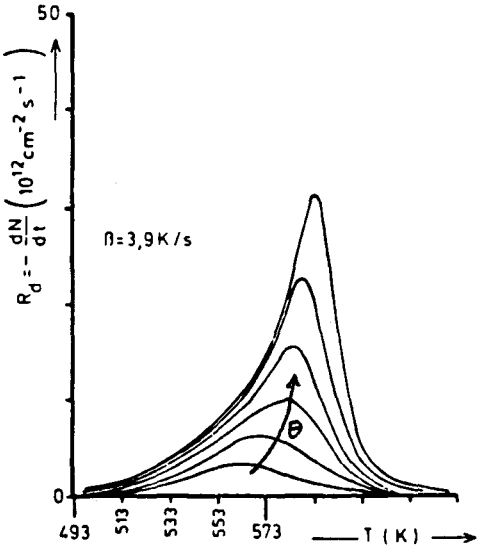


Figure 2.5: Thermal desorption curve of oxygen on silver.
Different curves represent different initial coverages θ.

with:

(2.20) $kd = \nu \exp(- Edes/kT)$

the desorption rate, A the surface area from which desorption takes place and P the pressure in the vessel. Thus:

(2.21) $P(T) = (A\beta/R'o)\ (dNs/dT) = (A\beta/R'o)\ Ns\ \nu \exp(-Edes/kT)$

A typical P against T curve is depicted in figure 2.5. The activation energy for desorption can be determined from the P(T) curve by solving:

(2.22) $dP(T)/dT \mid T=Tm = 0$

with Tm the position of the peak maximum which yields:

(2.23) $Edes \simeq kTm \{ \ln(\nu/\beta) + \ln ( Tm/(\ln(\nu/\beta)) ) \}$

This procedure, i.e. the determination of activation energies for desorption by using the maxima in thermal desorption spectra together with an "educated guess" fo the frequency factor is denoted as the "Redhead-method" /65/.

A number of surface analysis techniques are frequently used to characterize the surface region. Amongst them are LEED (Low Energy Electron Diffraction), TDS (Thermal Desorption Spectroscopy), XPS (X-ray Photo-electron Spectroscopy), AES (Auger Electron Spectroscopy), ISS (Ion scattering Spectroscopy) and SIMS (Secondary Ion Mass Spectroscopy). LEED and TDS have been described in chapter 2. In this chapter we will pay some attention to the other techniques mentioned. We will concentrate on XPS because we used this technique in our experiments. More elaborate treatments can be found in literature (e.g. /8/).

All these analytical techniques have in common that the specimen of interest is analyzed in a vacuum system (usually capable of ultimate pressures of $10^{-7}$ to $10^{-9}$ Pa) e.g. by irradiation of the samples with like X-ray photons (XPS), electrons (LEED, AES) or ions (SIMS and ISS). The UHV (Ultra High Vacuum) system is necessary to prevent contamination of the sample surface by adsorption from the ambient atmosphere (see equation 2.2). Particles leaving the surface, either electrons (LEED, AES and XPS) or ions (SIMS and ISS) are detected and energy analyzed (XPS, AES, ISS) or mass analyzed (SIMS).

In XPS, also called ESCA, Electron Spectroscopy for Chemical Analysis, the monochromatic X-radiation (ca. 1500 eV photon energy) employed liberates electrons from core levels in the specimen. The photo-electrons emerging from the surface enter an electron energy analyzer with which the photo-electron energy distribution can be measured. Peaks in this distribution correspond to unscattered photo-electrons from certain core levels in the sample. Specific elemental core binding energies can be used for elemental indentification. The surface sensitivity of XPS is due to the small (0.3 - 3 nm) mean free path of the photo-electrons with kinetic energies between 0.1-1 keV.

In AES the primary particles are electrons of energies between 1 and 30 keV kinetic energy which again can excite core levels in the specimen. The core hole created decays and one of the decay processes is the emission of an Auger electron. Emission of such an electron can be used for elemental identification because the kinetic energy of the Auger electron only depends on the binding energy of the initial core electron ionized and on the two electrons participating in the Auger process. The notation used to describe the AES signal originates from the electrons participating in the Auger process; e.g. the Cs(MNN) Auger signal denotes that the Auger electron stems from an N-subshell and has obtained its energy from another N-electron that filled the originally created M-subshell corehole. Surface sensitivity in AES is, as in XPS, due to the small mean free path of the Auger electron in the solid. The Auger process is depicted in figure 3.6c.

SIMS is performed by bombarding the sample with primary ions with an energy between 5 and 20 keV. These ions will collide with specimen atoms, some of which are ionized and gain enough energy to leave the specimen, usually with energies less than 50 eV. These secondary ions, which may be clusters of atoms, are mass analyzed and detected. Information about the composition of the specimen surface can be deduced from the recorded mass spectrum. The surface sensitivity in SIMS is due to the high cross-section for momentum transfer between the primary ions and specimen atoms.

In ISS the specimen is bombarded with monochromatic ions, usually of rare gasses, with kinetic energies of 0.5 - 5 keV. Some of the incident ions are scattered elastically by the specimen. These ions are detected and energy analyzed. The energy spectrum of the scattered ions is also a mass spectrum of the sample because the scattering event is defined by the kinematics, that is, by the masses of the incident ions and target atoms

and by the scattering angle. Surface sensitivity in ISS stems from the high neutralization probability of the rare gas ions which makes it very unlikely that scattered ions originate from deeper layers of the specimen. The virtue of ISS, besides its extreme surface sensitivity, is its ability to determine positions of atoms on the surface relative to others from either subsequent multiple scattering events or from the azimuthal anisotropy in scattered ion yield. To make full use of these virtues there is need for sensitive spectrometers with simultaneous energy and azimuthal resolving power one of which is currently in development /9/.

The four techniques are compared in table 3.1 with respect to spatial resolution (lateral as well as depth resolution), damage to the sample during measurement, elemental sensitivity and the ease of quantification.

| technique | lateral res.(μm) | depth res.(nm) | surface damage | elemental range | quanti-fication |
|---|---|---|---|---|---|
| AES | 0.05 | 0.3-3 | 0 | > Li | + |
| XPS | 150 | 0.3-3 | + | > Li | ++ |
| SIMS(static) | 0.05 | 0.3-3 | + | all | 0 |
| ISS | 100 | 0.3 | 0 | > Li | + |

Table 3.1: Comparison of four surface analysis techniques.

The principle advantages and disadvantages of the four techniques can be summarized as follows. AES is the technique with the highest lateral resolution (important in probing sub-micron devices) but is limited in use for fragile specimens which degrade under the electron beam. Furthermore there are charging problems with insulating samples. XPS can provide unique information about the chemical state of an element (by the chemical shift of photo-electron peaks) and is the technique in which the least damage is done to the sample. Its major drawback is its poor lateral resolution. With SIMS all elements can be detected, some of them in trace concentrations, and, like AES, the possibility of micro analysis exists. However, it is in principle a surface destructive technique and quantification is rather difficult. ISS is the technique with the highest surface sensitivity but the surface is also damaged during the measurement. "Static" SIMS and ISS (low lateral resolution and low dose of primary particles) should alleviate the problem of surface damage.

It is clear that there exists no "best" technique that is superior with respect to all problems. More than one surface analysis technique may be required to characterize the surface region. This will be illustrated in chapter 4. In the remaining part of this chapter we will treat XPS more thoroughly.

## 3.2: Instrumentation in XPS.

In all experiments described in chapter 6, a VG ESCA-III spectrometer was used. A schematic outline of the apparatus is given in figure 3.1. Electrons liberated from the sample (1) enter an energy analyser (2). Electrons of the selected energy are detected by a channeltron (3). An energy scan can be made by varying the potential applied to planar grids (4) in front of the energy analyser. The applied voltage determines the abcissa and the signal obtained from the channeltron theordinate of the PE-spect-

rum. The exciting X-radiation in XPS and the energy analyser will be treated in the subsequent two paragraphs.

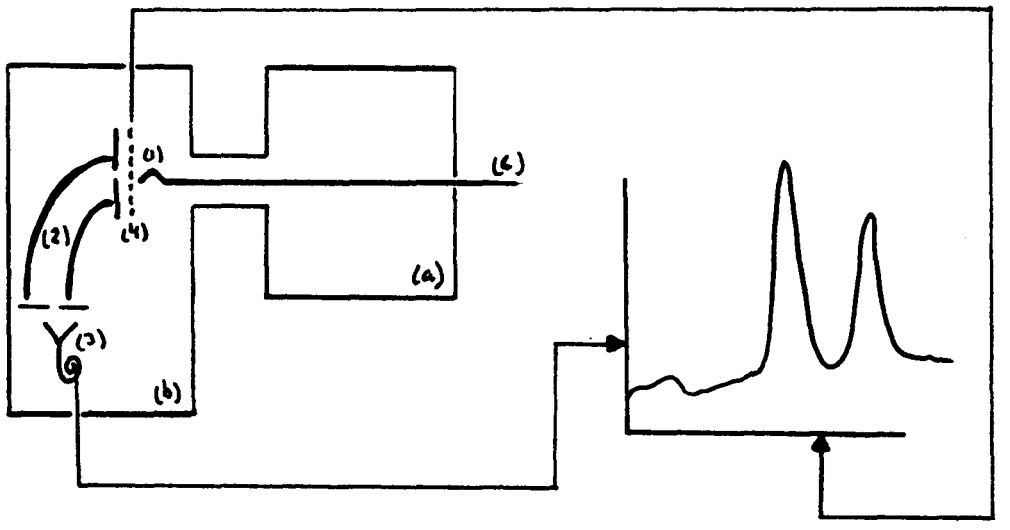


Figure 3.1: Outline of the ESCA apparatus.
(a): preparation chamber
(b): measuring chamber
(c): sample rod
Legend of numbers: see text.

### 3.2.1 The X-ray source.

X-radiation arises when matter (the anode material in an X-ray tube) is irridiated with a beam of electrons accelerated by a high voltage or with X-rays themselves. A spectrum is obtained consisting of a broad band of continuous radiation (Bremsstrahlung) superimposed on which are characteristic peaks. The position of these peaks depends only on the anode material of the X-ray tube.

The continuous radiation is a result of the deceleration of the exciting electrons (Bremsstrahlung). The distribution of the continuum as a function of the wavelength $\lambda$, $I(\lambda)d\lambda$, can be expressed in terms of excitation conditions by means of the Kramers equation /10/:

$$I(\lambda)d\lambda = K\ i\ Z\ (\lambda/\lambda min - 1)/\lambda^2\ d\lambda \qquad (3.1)$$

where $\lambda min$ is the minimum wavelength determined by the acceleration voltage, i the applied current, Z the atomic number of the anode material and K a constant.

The characteristic radiation arises from the re-arrangment of the orbital electrons following the ejection of an orbital electron from the target atom. In X-ray sources used in XPS, the anode usually consists of magnesium or aluminium. These elements have closed K and L shells. A hole in the K shell can be filled by an electron from the L-shell leaving an open L-shell with the configuration $2p^5$. With the L-S coupling scheme, this configuration gives two allowed spectroscopic terms 2P1/2 and 2P3/2 denoted LII and LIII respectively which differ slightly (0.5 eV) in energy /11/. The X-ray transition LII, LIII to K is denoted K$\alpha$1,2.

Multiply ionized Mg or Al atoms give Kα3,4... transitions which differ considerably (10-50 eV) in energy from the Kα1,2 doublet. They are responsible for the so-called X-ray satellites which appear in the XPS spectrum on the low binding energy side (BE-side) of each major photo-electron peak. In X-ray Photo-electron Spectroscopy the abcissa of the spectrum is usually expressed in terms of binding energy of the electrons in the solid, relative to the Fermi-edge. This has the advantage that the peak position is independent of the exciting radiation. The assignment can be confusing because it is of course the kinetic energy of the photo-electrons which is measured. In this report we will also refer to the BE of the photo-electrons.

The X-ray satellites and continuous radiation are responsible for an unwanted contribution to the background signal in the XP-spectrum. X-ray satellites can be subtracted quite easily because their positions and relative heights are known. Table 3.2 summarizes the major constituents of the characteristic X-ray spectrum of aluminum and magnesium. The Bremsstrahlung fraction of the total intensity of the impinging X-radiation can be made small if a sufficiently high acceleration voltage is chosen; in practice a value of 10 kV is frequently applied. Furthermore a thin (6 μm) window can be used which filters the high energy tail of the continuous Bremsstrahlung distribution, see figure 3.2.

| name | Al photon energy (eV) | relative height | Mg photon energy (eV) | relative height |
|---|---|---|---|---|
| Kα1,2 | 1486.6 | 100 | 1253.6 | 100 |
| Kα3 | + 9.8 | 6.4 | + 8.4 | 8.0 |
| Kα4 | +11.8 | 3.2 | +10.2 | 4.1 |
| Kα5 | +20.1 | 0.4 | +17.5 | 0.55 |
| Kα6 | +23.4 | 0.3 | +20.0 | 0.45 |
| Kβ | +69.7 | 0.55 | +48.5 | 0.5 |

Table 3.2: Kα(2p to 1s) and Kβ(3p to 1s) X-radiation in aluminum and magnesium.

The line width of a photo-electron peak will depend, among other factors, on the monochromaticity of the X-ray source. To avoid limitation of the achievable resolution by the X-radiation line width, it is necessary to use materials for the source anode which's line width is less than app. 1.0 eV. The Kα1,2 doublets of aluminum and magnesium, which remain unresolved in XPS, in fact have line widths of 0.85 and 0.7 eV FWHM respectively. This is one of the reasons why these two X-radiations are commonly applied in XPS.

### 3.2.2 The electron energy analyser.

The electron energy analyser used in the ESCA-III is a concentric hemispherical analyser (HSA), schematically shown in figure 3.3. Two hemispherical surfaces with radii R1 and R2 are positioned concentrically. A potential difference ΔV is applied between the surfaces, the inner sphere positive, the outer sphere negative. Entrance and exit slits are positioned at a distance R0 from the centre of curvature, $R0=\frac{1}{2}(R1+R2)$. The HSA acts as an electron monochromator; only electrons with a kinetic energy

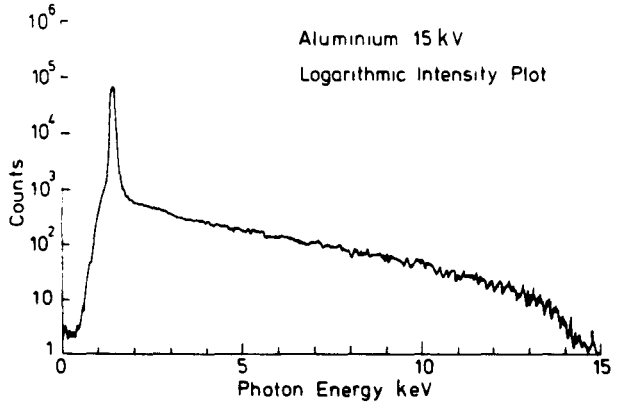


Figure 3.2: A typical frequency spectrum of the exciting radiation in XPS after filtering trough a Be-window of 7 μm. X-ray source operating at 15 kV, aluminium anode.

E0±ΔE can pass the HSA. Energy scans can be performed by varying the potential of planar retarding grids in front of the entrance slit.

The energy resolution ΔE/E0 (FWHM) obtained can be written as /12/:

$$(3.2) \qquad \Delta E/E0 = w/2R0 + \alpha^2$$

with w the slit width and α the half angle of admission in the energy dispersing plane. The resolution is a constant for a given geometry so it increases linearly with decreasing E0. However, when resolution increases, sensitivity decreases because the latter is proportional to $(E0/\Delta E)^2/\varepsilon$ with ε the kinetic energy of the electrons before retardation /12/. A good compromise between sensitivity and resolution is a setting of the pass energy to 50 eV at the ESCA-III. The analyser resolution thus obtained is approximately 1.2 eV.

### 3.2.3 The spectrometric workfunction.

Essentially, the kinetic energy KE of the photo-electrons is given by:

$$(3.3) \qquad KE = h\nu - BE$$

with hν the photon energy and BE the binding energy of the electron in the solid. In an actual experiment, KE is measured with respect to the ground potential of the analyser. If the sample is a conductor, there exists a contact potential between analyser and sample. The measured kinetic energy KE' is therefore:

$$(3.4) \qquad KE' = h\nu - BE - e(\phi sp - \phi s)$$

where the contact potential $\Delta\phi$ is the difference in workfunction between spectrometer ($\phi sp$) and sample ($\phi s$). To circumvent the determination of $\Delta\phi$, binding energies are usually referred to the Fermi level, see figure 3.4. Equation (3.4) becomes:

$$(3.5) \qquad KE' = h\nu - BE' - e\phi sp$$

with $BE' = BE - e\phi s$. The spectrometric workfunction $\phi sp$ can be determined from a calibration experiment with a clean sample of an element with known binding energy.

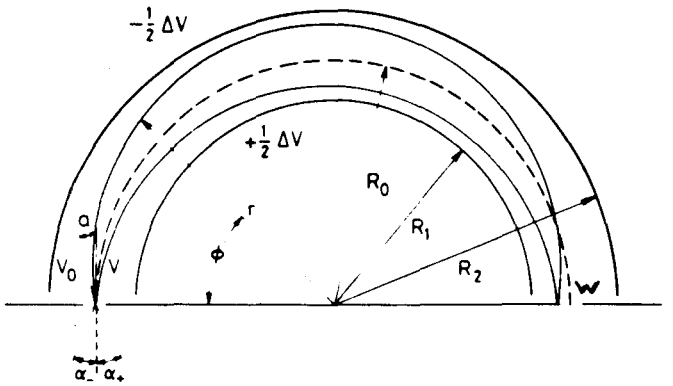


Figure 3.3: The hemispherical electron energy analyser (HSA).

For insulators the situation is more complex as photo-emission leads to a positive charging of the sample making absolute measurements virtually impossible. The most commonly used reference is the C1s peak of adventitious carbon species usually present on the surface.

## 3.3: Fundamental concepts.

### 3.3.1 Creation and relaxation of the core hole.

A number of processes are responsible for the attenuation of X-rays as they proceed through matter. In general, electromagnetic radiation interacts with the electrons as well as the nuclei of the solid. For low energy X-radiation only the interaction with the electrons of the atoms has to be considered.

If a free electron is irradiated by an electromagnetic wave, classical electrodynamics predicts emission from the accelerated electron. The induced radiation has the same frequency as the incident wave but not necessarely the same direction so that the whole process can be thought of as a scattering of the incident radiation. The differential cross section $d\sigma/d\Omega$, describing the scattering of a plane monochromatic electromagnetic wave by a free electron, is given by Thompson's formula /6/:

$$(3.6) \qquad d\sigma/d\Omega = e^2 (1 + \cos^2\theta) / 2mc^2$$

where e is the charge of the electron, m is its mass, c is the velocity of light and $\theta$ is the scattering angle. This formula is a purely classical one. It breaks down at high photon energies where the electron recoils during the collision and the scattered radiation is shifted towards lower frequencies (Compton scattering). At photon energies below 10 keV Compton scattering becomes negligible.

The electrons cannot be thought of as being in one place at a certain time but must be described by wave functions which only allow for an electron density description. Scattering takes place by the time averaged electron distribution. Furthermore, the inner electrons of heavier elements have binding energies in the order of the X-ray photon energies and therefore cannot be considered as free particles. However, to get an impression of the total scattering cross section involved, the integral Thompson cross section is taken as a measure for the scattering by each electron. In this way, the total cross section for an element with atomic number Z

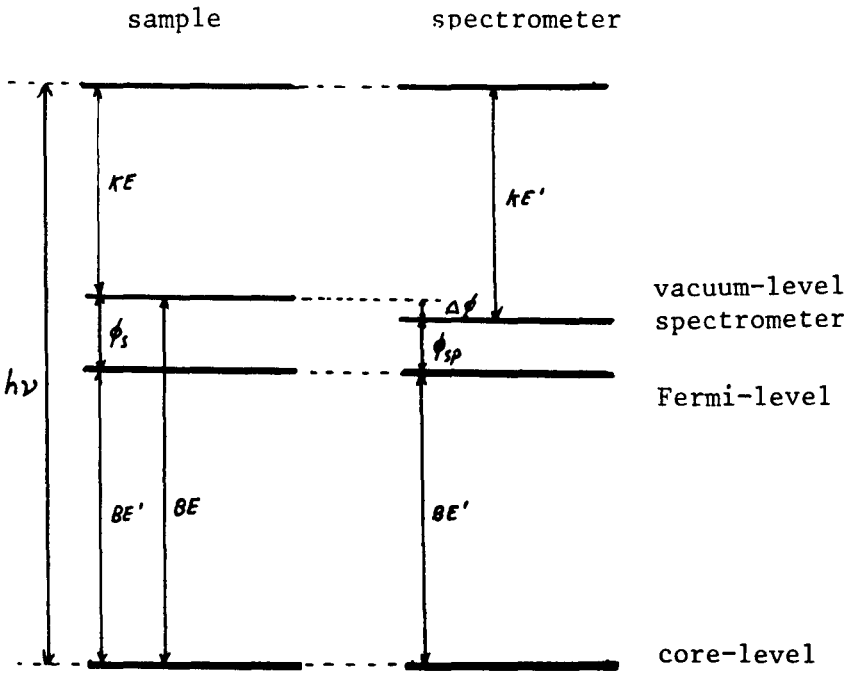


Figure 3.4: The measured kinetic energy KE' differs from the initial kinetic energy KE by an amount $\Delta\phi$. To circumvent the determination of $\Delta\phi$, binding energies BE are not referred to the vacuum level (which is different for sample and spectrometer) but to the common Fermi levels. Of course the figure only depicts the situation with conducting samples.

becomes Z times 0.665 barn (1 barn=$10^{-28}$ $m^2$), the integral Thompson cross section for one electron.

The dominant attenuation process for low energy X-ray photons is the **photo-ionization** of core levels by virtue of which XPS signals are generated. The photo-emission of an electron can be described by a photo-electric cross section. This cross section is a function of the transition matrix element Pk-i for a transition from an initial state k to a final state i in the atom. SCOFIELD /13/ calculated photo-ionization cross sections at the commonly used photon energies of 1254 and 1487 eV (MgKα and AlKα radiation respectively).

These calculations were carried out relativistically using the single-potential Hatree-Slater atomic model /14/ in which the potential is determined self consistently for the neutral atom occupations of the subshells. A relativistic treatment was necessary because of the high (≃ hundreds eV) energy of the electrons involved.

The inaccuracy in the Hartree-Slater model is caused by the approximate manner of treating the electron-electron interaction. Furthermore, it is a frozen orbital model in which relaxation effects are neglected. However, for not too high Z elements, it has been found that the calculated total cross-sections agree with compilations of measured data within 5 percent. Experimental results on individual subshell cross-sections are far too fragmentary for a good comparison with theory.

The calculated cross-sections range from $10^2$ to $10^6$ barn, exceeding the Thompson cross-sections at least by two orders of magnitude. The photo-ionization process is thus certainly the dominant attenuation effect for low energy X-rays as they pass through matter. Attenuation lengths can be calculated to be in the order of 200 nm in silver for Al or MgKα radiation which are several hundred atomic layers.

## Relaxation effects.

In a single electron picture of photo-emission, the total energy hν of the absorbed photon is taken up by a single electron. Essentially this means that all the remaining electrons are not influenced by the removal of the inner shell electron under consideration. The binding energy BE of the photo-electron in equation (3.3) then equals the initial orbital energy of the core electron, according to Koopmans' theorem /15/ (frozen orbital approximation or sudden approximation).

If the electron is taken out and the ionized system left behind is allowed to adjust to the ionized state, it will relax to a lower energy state by adjusting the orbitals of the remaining electrons to the altered electrostatic field, a process called intra-atomic relaxation. When the photo-emitting atom is imbedded in a polarizable medium another relaxation effect occurs. The positive charge created by the photo ionization process attracts electrons that tend to screen it, resulting in a lowering of the total energy of the system left behind, a process termed extra-atomic relaxation. These relaxation energies are partially carried away by the photo-electron which thus appears at higher kinetic energy as compared to the frozen orbital approximation. These relaxation energies are in the order of several eV /16/.

The dipole varying with time which appears as a result of the outgoing electron and positive hole left behind can excite the losely bound valence electrons of the system. This may involve the transition of one of the valence electrons to a higher unfilled level (shake-up process) or to an unbound continuum state (shake-off process). The energy required for such a transition is taken from the primary photo-electron, which is said to have suffered intrinsic losses. These processes lead to structures on the high BE side of the photo-electron (PE) peak, referred to as shake-up respectively shake-off satellites.

Discrete amounts of energy are required to promote an electron to a higher unfilled valence level as in the shake-up process, whereas in the shake-off process any amount of energy beyond the binding energy of the electron can be absorbed. Therefore, the former will lead to a peak-like structure while the latter comprises a rather featureless inelastic tail on the high BE side of the photo-electron peak.

In metals where electrons at the Fermi level can acquire any amount of energy, these excitations will lead to broadening of the photo-electron line on the high BE side. The degree of asymmetry depends on the density of states at the Fermi level. A metal like silver with a low density of states at the Fermi-level will have rather symmetric XPS peaks, a metal like platinum with a high density of states at the Fermi-level will have rather asymmetric XPS-peaks. Photo-electron peaks of silver (3d doublet) and platinum (4f doublet) are depicted in figure 3.5. Electrons which have suffered intrinsic losses must be accounted for in the total area of the photo-electron peak if Scofields' cross-sections are used to quantify the peak intenity (paragraph 3.4). If not, the estimated amount of photo-emitting material under consideration will be too low.

A core hole has a finite lifetime and will be eventually filled in by an electron from a higher filled level. An electron from a higher shell fill-

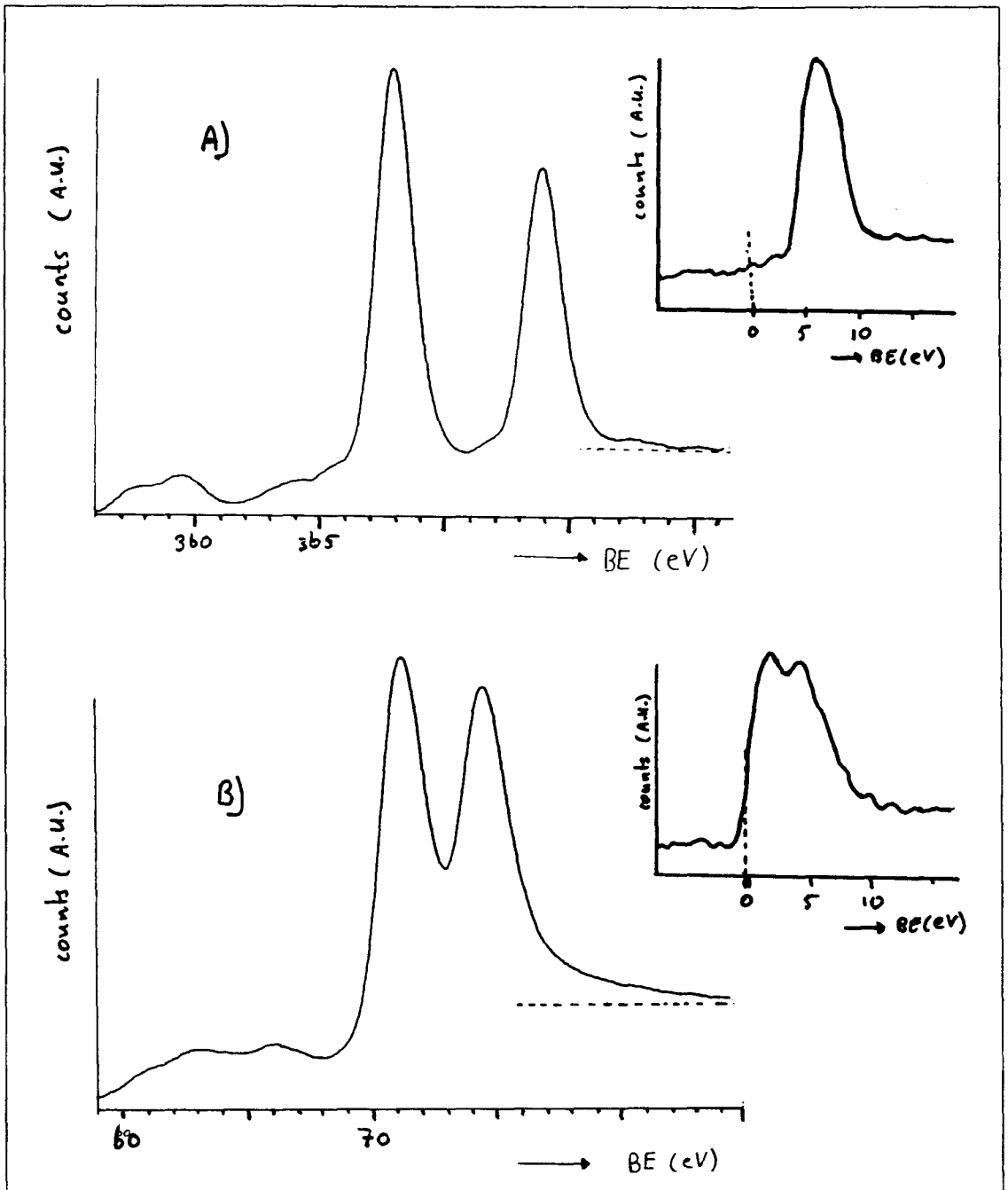


Figure 3.5: A) The silver 3d doublet. Note the symmetrical peak shape.
B) The platinum 4f doublet. Note the asymmetrical peak shape as a result of the high density of states at the Fermi-level compared to silver (see insets).

ing the hole can release its excess energy in two competing ways. Either this energy is transferred to a second electron by a radiationless process which then is emitted as a so-called Auger electron or the excess energy is eradiated directly as an X-ray photon (X-ray fluorescence). The ratio of probabilities for Auger electron production and X-ray generation decreases with increasing binding energy of the core electron originally released. For the first transition row of the periodic table the two processes roughly have the same probability. Both processes are indicated in figure 4.6. Thus in an X-ray excited PE-spectrum also Auger electrons are encountered. To distinguish between primary photo-electrons and Auger electrons a different exciting source can be used so that the KE of only the primary photo-electrons will vary.

### 3.3.2 The chemical shift

Once the inherent complications of the final state of the photo-emitting system are understood, the observed kinetic energy of the photo-electrons may be used to deduce information on the undisturbed initial state of the system. The binding energy of a core electron in this initial state depends on the average charge around the atom e.g. on the occupation of the valence levels of the photo-emitter. Therefore the BE is influenced by a different chemical environment. This leads to shifts in binding energies, a result of the alternation of the electrostatical fields in the vicinity of the core as will be shown below.

Binding energy shifts are small (1-10 eV), a few percent of the core level energies (100-1000 eV), but easily detected. Binding energy shifts as a result of a different chemical environment are called **chemical shifts** and can be used to gain information about the chemical environment of the photo-emitting atom. This indirect measurement of the redistribution of the valence electrons has the advantage of being rather straightforward as compared to the direct spectroscopy of the valence shell (e.g. UPS measurements). A qualitative description of the chemical shift is given by Gelius /17/.

Neglecting relaxation effects, the chemical shift $\Delta E_i$ for a core electron i of atom $\alpha$ equals the difference in Hartree-Fock energies $\Delta\varepsilon_i(HF)$ of a reference level of an element or compound and the level under consideration:

$$\Delta E_i = -\Delta\varepsilon_i(HF) \qquad (3.7)$$

The Hartree-Fock orbital energy $\varepsilon_i(HF)$ may be written as:

$$\varepsilon_i(HF) = \langle i|\ -\tfrac{1}{2}\nabla^2\ |i\rangle + \sum_\beta \langle i|\ -\frac{Z\beta}{r\beta}\ |i\rangle + \sum_j (2J_{ij} - K_{ij}) \qquad (3.8)$$

in which the first term describes the kinetic energy of the core electron i, the second term gives the nuclear attraction summed over all nuclei $\beta$ and the third term expresses the electron-electron repulsion with J and K the Coulomb and exchange integrals. We consider the core orbitals constant under reorganisation of the valence electrons, omit the exchange between core electrons of different nuclei and between core and valence electrons and let the inner electrons of all atoms $\beta$ shrink into their respective nuclei. The interaction of the core electron i with the nuclei and core electrons of atoms $\beta$ may then be regarded as between point charges charges. The remaining expression for the shift $\Delta E_i$ in the binding energy of core electron i of atom $\alpha$ is:

$$\Delta E_i \simeq -\Delta\varepsilon_i(HF) = \Delta\left(-\sum_{\substack{j=\text{val.}\\ \text{orbital}}} 2J_{ij} + \sum_{\beta=\alpha} \frac{Z'\beta}{r\alpha\beta}\right) \qquad (3.9)$$

with $Z'\beta$ the effective nuclear charge ($Z\beta$ - number of core electrons) and $R\alpha\beta$ the internuclear distance between atom $\alpha$ and $\beta$. Equation (3.9) shows

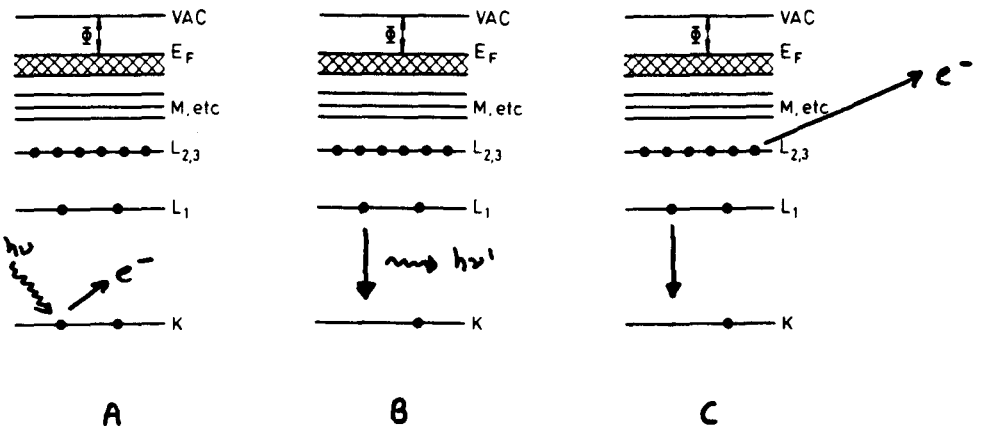


Figure 3.6: A) Photo-ionization of a core level by an incident photon hν.
B) X-ray fluoresence: the core hole is filled by an electron from a higher level which emits a photon hν'. hν' reflects the energy difference between the two levels.
C) The Auger process: the core hole is filled by an electron from a higher level and gives its energy to another electron. This electron, the Auger electron, is emitted.

that the chemical shift is well described by the variation in electrostatical potential involving all valence electrons.

From this model we can easily predict the direction of chemical shifts. The BE of core electrons will increase if the corresponding valence electrons of the atom will be transferred to another atom (the increase in BE will further be corroborated by orbital contraction following partial ionization of the atom, an effect neglected in the derivation of eq. 3.9). Absolute BE of core electrons in different compounds referred to the Fermi level can be found in several handbooks (e.g. /64/).

### 3.3.3 The angular distribution of the photo-electrons.

Usually the energy analyzer employed in XPS has a small acceptance angle. Thus only a small part of the emitted photo-electrons will be detected. If this small part is taken as a measure for the abundance of certain species relative to one-another, the angular distribution of the photo-electrons has to be taken into account.

Assuming an electric dipole interaction, it can be shown /18/ that the angular distribution of photo-electrons ionized by unpolarized light impinging on a nl-subshell dσnl/dΩ is given by:

$$\frac{dnl\sigma(\varepsilon)}{d\Omega} = \frac{\sigma nl(\varepsilon)}{4\pi} \{ 1 - \tfrac{1}{2}\beta nl(\varepsilon) P2(\cos\theta) \} \qquad (3.10)$$

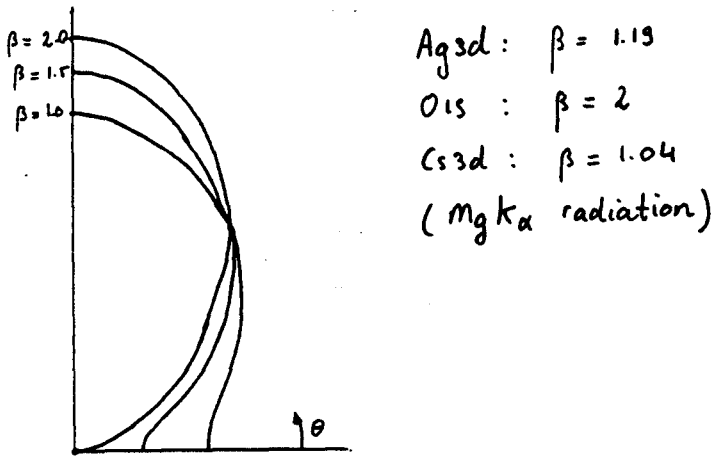


Figure 3.7: Polar plot of the angular distribution of photo-electrons originating from different core levels as a function of β calculated by REILMAN /19/

where ε is the photo-electron energy, σnl is the crossection for photo-ionizing an nl subshell electron, θ is the angle between photon and photo-electron direction and P2 is the Legendre polynomial of order 2. βnl(ε) is called the asymmetry parameter dependent on the details of the wave functions employed.

By using Hartree-Slater wave functions, REILMAN et al. /19/ calculated βnl(ε) for MgKα and AlKα radiation over a broad range of atomic numbers. For "deep" core shells (BE>200 eV) usually ionized in XPS, it is expected that the obtained results will be excellent.

However, it is not known if these asymmetry parameters are appropiate for solid surfaces. They are well tested for gasses but experiments on solids have not as yet yielded conclusive results so far. Because of the rather small correction involved (typically 5 %), we will use the values of βnl(ε) as calculated in ref. 19 to account for the angular asymmetry.

The determination of the angular asymmetry parameter can be completely circumvented by acquisition of the photo-electrons at 54.74° which angle coincides with the node of P2(cosθ) and is frequently called the 'magic angle'.

### 3.3.4 Extrinsic energy losses of the photo-electrons.

The mean free path for X-ray photons in solids is much larger than the scattering length of photo-electrons they liberate, so the electron mean free path will limit the escape depth of the photo-emitted electrons. The mean free path of the photo-electrons for various materials and as a function of their kinetic energy still remains the least well known parameter in photo-electron spectroscopy. So far, the results of theoretical evaluations /20-22/ and curve fitting on compilations of measured data /23/ deviate considerably, which may be due to oversimplified models or experimental intricacies.

An example of the theoretical approach stems from PENN /20,21/, whereas the semiempirical determination of inelastic mean free paths will be exemplified by the popular model of SEAH et al. /23/.

i) theory after PENN.

The inelastic processes that define the mean free path of 'hot' electrons (electrons with kinetic energies exceeding kT) are electron-electron, electron-phonon and electron impurity scattering. For electron energies of several hundred eV, as encountered in XPS, electron-electron interaction accounts for the major contribution to the mean free path /24/.

Electron-electron interaction may involve the excitation of a single electron or a plasmon excitation, a collective many body excitation. Both processes lead to a large energy transfer, a few eV for the former and in the order of 10 eV, the plasmon energy hνp, for the latter. This implies that it is possible to distinguish experimentally between scattered and unscattered electrons, scattered electrons will be well separated from the unscattered electrons in the PE spectrum.

The primary cause of the electron attenuation is the inelastic scattering from the valence electrons. PENN calculated electron mean free paths in free-electron-like materials which he defines as materials that show predominant losses due to plasmons with an energy ωp close to the free electron value:

$$\omega p = \sqrt{(4\pi\eta e^2/m)} \qquad (3.11)$$

with $\eta$ the density of the valence electrons, e their charge and m their mass. For such a material the inelastic mean free path due to valence band excitations depends only on the kinetic energy $\varepsilon$ of the hot electron and on the average electron density $\eta$. PENN showed that the mean free path $\lambda v$ due to these excitations can be written as:

$$\lambda v = \frac{\varepsilon}{Av\,(\ln\varepsilon + Bv)} \qquad (3.12)$$

with Av and Bv functions of the electron concentration $\eta$.

In his calculation, PENN neglects the contribution due to surface plasmon excitation (which is reasonable because of the rather large mean free paths involved) and core electron excitation. The excitation of the core electrons has been worked out by POWELL /22/ who finds an isomorphic formula for $\lambda c$, the mean free path due to core electron excitation:

$$\lambda c = \frac{\varepsilon}{Ac\,(\ln\varepsilon + Bc)} \qquad (3.13)$$

if we further neglect the contribution of all but the highest core level. Ac is dependent only on the density $\rho$, the atomic number A and the average core electron excitation energy $\Delta E$, Bc is solely dependent on $\Delta E$. The contribution of core electron excitation is of minor importance, $\lambda c \approx 10\,\lambda v$.

The total mean free path $\lambda t$ of the photo-electrons can now be evaluated from $1/\lambda t = 1/\lambda v + 1/\lambda c$ and the constants A and B tabulated by PENN /20/ and POWELL /22/. It is expected that in the case of free-electron-like materials the mean free path should be accurate to 5%, for non-free-electron-like materials it may be up to 40% larger.

ii) the universal curve by SEAH et al.

SEAH et al. /23/ derived a "universal curve" which fits a compilation of all published measurements till 1980 on mean free paths in solids for energies in the range 0 - 10 keV. For elements they found:

$$\lambda = 538 \frac{t}{\varepsilon^2} + 0.41\, t^{3/2} \sqrt{\varepsilon} \qquad (3.14)$$

with $\varepsilon$ the electron energy in eV and t the monolayer thickness in nm:

$$t^3 = 10^{24} A/\rho Na \qquad (3.15)$$

with A the atomic mass, $\rho$ the bulk density (kgm-3) and Na Avogadro's number.

Equation (3.14) was recommended by the authors as a covenient means of estimating IMFP's in solids for which no measurements had been made. A simular fitformula for $\varepsilon<300$ eV on measurements made in a single laboratorium was found by WAGNER et al. /25/. They found an energy power dependence of 0.54-0.81 dependent on the material studied. Although PENN's equation is somewhat more complex, the energy dependence he derives also follows a power dependence on the electron energy $\varepsilon$ with exponents in the range 0.7-0.8. The square root dependence derived by SEAH et al. and the power dependence derived by PENN seem to give the lower and higher bound of the energy power dependence found till to date.

The material dependence in equation (3.14) is questioned by POWELL /26/ who calculated IMFP's of 100-2000 eV electrons in various materials. He found a stronger material dependence.

Equation 3.14 provides a simple and convenient means of estimating IMFP's in materials for which no measurements or specific calculations have been made. However, there can be significant deviations from the assumed energy and material dependence. Further work is required to make quantitative predictions of these variations.

Equation (3.14) is shown graphically in figure 3.8 for silver and caesium, together with (3.12,13).

### 3.3.5 Example: the silver PE-spectrum.

Figure 3.9 depicts a wide scan spectrum of a clean silver surface obtained using AlKα radiation and the HSA operating in the constant pass energy mode. A series of peaks is observed on a background which increases to low kinetic energy. All components of the incident radiation (that is Bremsstrahlung, characteristic radiation and X-ray satellites, see paragraph 3.2) contribute to the photo-electron emission according to equation (3.3). In writing this equation it is assumed that the photo-electrons have not undergone any extrinsic losses, that is, have not suffered energy losses between their photo-emission and their detection. Photo-electrons that have undergone losses will appear on the high BE side of the elastic photo-electron peak in the XPS spectrum and account for the stepwise increase of the background after each major photo-electron peak.

Note that photo-electrons are generated till deep in the sample because of the large X-ray attenuation length and that therefore the tail of a photo-electron peak of a semi-infinite sample extends to hundred eV to the high BE side of the PE peak.

The series of peaks in figure 3.9 reflects the ionization of the silver core levels. The AlKα radiation applied is only energetic enough to probe

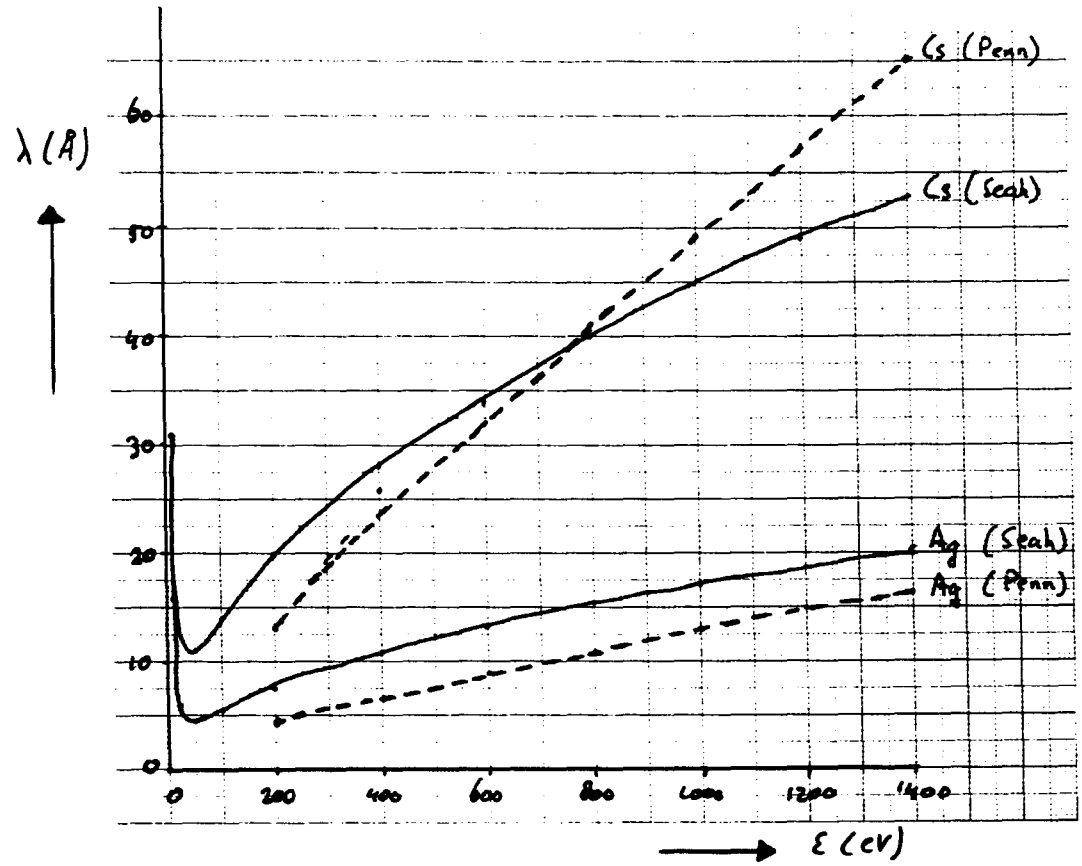


Figure 3.8: Mean free paths in elemental Ag and Cs as a fuction the electron kinetic energy, calculated by PENN /20/ and SEAH /23/.

the core levels of silver down to the 3s shell. The core levels have variable intensities and widths and the non-s orbitals are doublets. The doublets arise from spin-orbit coupling, the energy difference between two states reflects the parallel or anti-parallel alignment of the spin and orbital angular momentum of the remaining electron. For example, the filled $3d^{10}$ subshell of silver, upon ionization, can give rise to a j=3/2 and j=5/2 configuration in a j-j coupling scheme. The relative intensities of the doublet peaks are given by the ratio of their respective degeneracies, 2j+1.

The peak width, defined as the full width at half maximum (FWHM) ΔE is a convolution of several contributions which approximately add as:

$$\Delta E = \sqrt{(\Delta En^2 + \Delta Ep^2 + \Delta Ea^2)} \qquad (3.16)$$

with ΔEn the natural energy width of the core hole, ΔEp the width of the X-ray line (≃ 1 eV for AlKα) and ΔEa the analyzer (absolute) resolution. ΔEa is a constant and equals ≃ 1.2 eV when the HSA is sett to a pass energy of 50 eV. ΔEn is a direct reflection of the lifetime Δt of the core hole:

$$\Delta En\ \Delta t = \hbar \qquad (3.17)$$

which is governed by the core hole decay process (Auger process, X-ray fluoresence). For a frequently encountered FWHM of 2.0 eV (50 eV pass energy, AlKα exciting radiation) it follows that the lifetime of the core hole must lie in the order of $10^{-14}$ s.

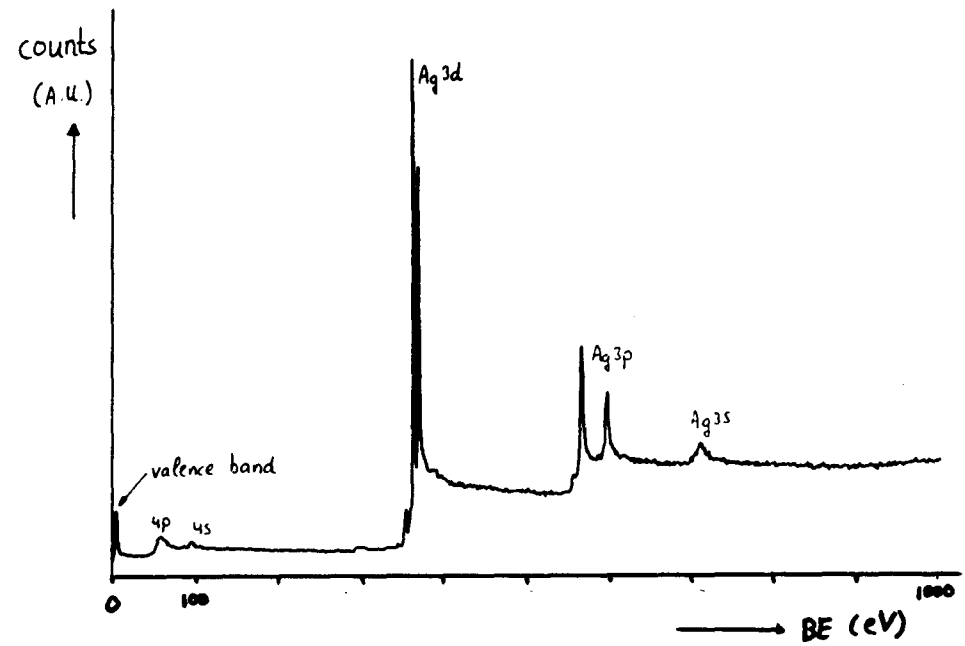


Figure 3.9: A wide (0-1000 eV BE) scan of a clean silver surface. All silver levels up to 3s can be detected. The exciting radiation was AlKα, the analyser pass energy 50 eV. The 4p doublet is not resolved.

### 3.4: Quantification of the XPS signal.

The description of the XPS technique given until now has been rather qualitative. However, as already pointed out in paragraph 3.1, XPS can provide also quantitative information about the surface region. In the next three paragraphs an expression is derived for the adsorbate coverage on a homogeneous sample as a function of their respective XPS signal intensities. Some attention is paid on the determination of these signal intensities from the measured spectrum.

#### 3.4.1 Assumptions made.

The electron intensity I obtained in XPS can be written in a formal straightforward way as /12/:

$$I = \sigma(h\nu)\, D(\varepsilon) \int_{\gamma}\int_{\phi} L(\gamma) \int_{x}\int_{y} Jo(x,y,\gamma,\phi,\varepsilon) \int_{z} N(\vec{x}) \exp\left(-\frac{z}{\lambda\cos\theta}\right) d\gamma\, d\phi\, d\vec{x} \qquad (3.18)$$

In this equation, $\sigma(h\nu)$ is the cross-section for emission of a photo-electron from the relevant inner shell per atom by a photon of energy $h\nu$, $D(\varepsilon)$ is the detection efficiency for an electron transmitted by the electron spectrometer, $\gamma,\phi,x,y$ and $z$ are given in figure 3.10, $L(\gamma)$ is the angular asymmetry of the intensity of the photo-emission from each atom, $Jo(x,y)$ is the X-ray characteristic line flux intensity at point $(x,y)$ on the sample, $T(x,y,\gamma,\phi,\varepsilon)$ is the analyzer transmission and $N(x,y,z)$ is the atomic

density of the photo-emitting atoms at (x,y,z). $\lambda(\varepsilon)$ is the mean free path of the characteristic XPS electrons of energy $\varepsilon$ and $\beta$ is the angle of emission of the electron from the surface normal.

If the electrons are detected by a pulse count mechanism in which every single electron is detected individually, as is the case in the VG ESCA III, $D(\varepsilon)$ reduces to unity for all $\varepsilon$.

We now consider a semi-infinite homogeneous sample. In this case, the integral over z just becomes $N \lambda \cos\beta$. A number of additional assumptions are made:

- The HSA employed in the ESCA III has a small acceptance angle. Therefore the integrals over $\gamma$ and $\phi$ can be omitted. What remains is the value of L at the collection angle $\gamma$, in the ESCA III 105°.
- The sample is illuminated uniformly by the X-rays. The constant Jo can be taken before the integral over x and y. What remains is the surface integral over the transmission function usually called the analyzer's etendue. The energy dependence of the etendue can be taken &prop. $1/\varepsilon$ for the VG ESCA III operating at a constant pass energy /27/.

(3.18) now becomes:

$$(3.19)\quad I \propto \sigma(h\nu)\, L(\gamma)\, N\, Jo\, \lambda(\varepsilon)\, \cos\beta\, /\, \varepsilon$$

### 3.4.2 The fractional overlayer on a homogeneous sample.

We now consider the special case of a fractional overlayer on a homogeneous substrate (see figure 3.11). We will use the subscript i for element i in supported compound k and p for element p in support s. We want to know how much i is present in the surface region. From the proposed model and the measured peak areas Ii,k and Ip,s an expression for $\theta k$, the coverage of k on support s, can be derived.

The photo-electron peak intensity Ii,k is proportional to the coverage $\theta k$. Compared to the signal I i,k acquired for a semi-infinite sample k, the

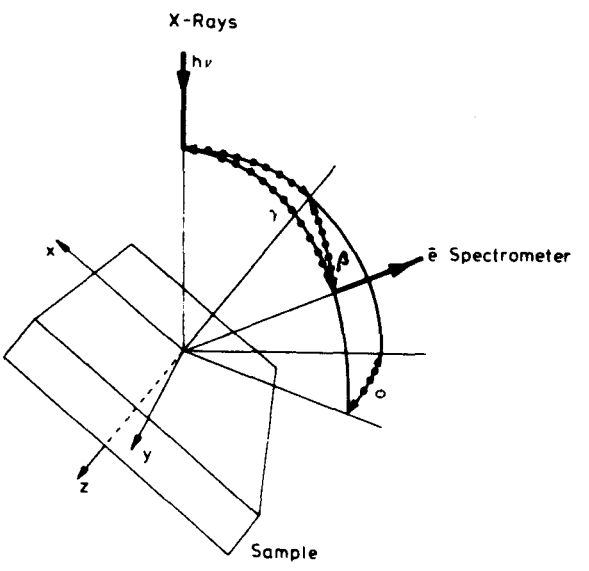


Figure 3.10: Geometry of the XPS analysis configuration.

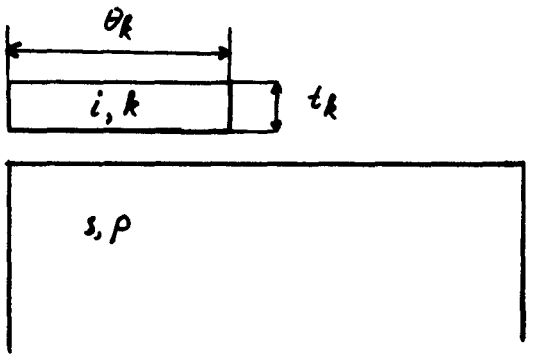


Figure 3.11: A homogeneous substrate s with element p, an adsorbate k with element i. k covers θk of s.

signal Ii,k is smaller due to the finite overlayer thickness tk. Ii,k can be expressed as:

$$(3.20) \qquad I_{i,k} = I_{i,k}\,\theta_k \{ 1 - \exp(-t_k/\lambda_{i,k}) \}$$

with $\lambda_{i,k}$ the mean free path of photo-electrons stemming from i through the matrix of k. We have made the assumptions that the sample is perfectly flat and all electrons are collected along the surface normal ($\beta=0^\circ$). The photo-electron attenuation is described by the exponential function.

The intensity Ip,s acquired for element p in support s is attenuated with respect to I p,s (semi-infinite sample of s) by an amount proportional to θk and dependent on the overlayer thickness tk. Ip,s becomes:

$$(3.21) \qquad I_{p,s} = I_{p,s} \{ 1 - \theta_k(1-\exp(-t_k/\lambda_{p,k})) \}$$

with $\lambda_{p,k}$ the mean free path of photo-electrons from p in the matrix of overlayer k. The signal ratio Ii,k/Ip,s is written as:

$$(3.22) \qquad I_{i,k}/I_{p,s} = I_{i,k}/I_{p,s}\; T(\theta_k, t_k)$$

with T(θk,tk) describing the geometry of the underlying case. I i,k/I p,s can be calculated (3.19) or determined experimentally with an accuracy of 10 to 50 %, depending on the sample.

Until now we used an exponential function to account for the attenuation of the photo-electron intensity. If however the sample is not perfectly flat, we cannot assume a single collection angle β. Surface roughness comprises an averaging with respect to the collection angle β as will be immediately clear from figure 3.12. For a true random distribution of collection angles (e.g. powder samples) this means that the simple exponential attenuation function has to be replaced by Γi,k given by /28/:

$$(3.23) \qquad \gamma_{i,k} = 2 \int_0^{\frac{1}{2}\pi} \sin\beta \cos\beta \exp\left(-\frac{t_k}{\lambda_{i,k} \cos\beta}\right) d\beta$$

which can be approximated by:

$$(3.24) \qquad \Gamma_{i,k} \approx \exp(-t_k/\lambda_{i,k}) \;/\; \{2 - \exp(-t_k/\lambda_{i,k})\}$$

The average escape depth of photo-electrons in true random samples is smaller than compared to that of perfectly flat samples with $\beta=0^\circ$ by a factor of 0.75 /28/. The replacement of the exponential attenuation func-

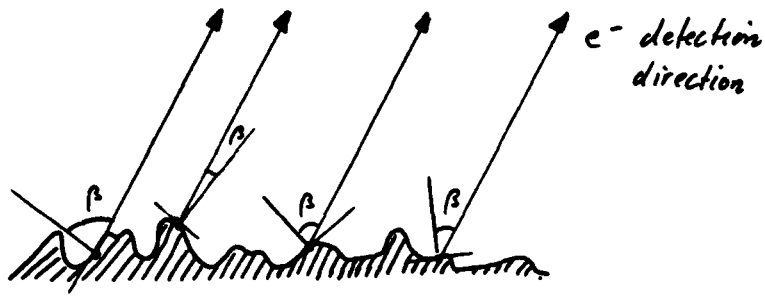


Figure 3.12: Angular averaging as a result of surface roughness.

tion by Γi,k thus influences the apparent coverage θk. The largest apparent coverage at constant intensity ratio Ii,k/Ip,s will be found with the exponential attenuation function at an collection angle of 0° (smallest surface sensitivity). The smallest apparent coverage will be found by collecting photo-electrons from a perfectly flat sample at an angle β near 90° (highest surface sensitivity). In practice, samples are not perfectly flat. Therefore we will use as the lower limit for the apparent coverage θk at constant intensity ratio Ii,k/Ip,s the value obtained with the Γ-attenuation function, and as upper limit the value obtained with the exponential attenuation function at a collection angle β=0°.

In order to estimate the uncertainty introduced by the unknown surface roughness, we assume tk<<λ which allows the exponential functions to be approximated by the first two terms of their power expansions. This requirement is fulfilled for adsorbate monolayers.

In the case of a perfectly flat sample we obtain with the exponential attenuation function by use of (3.22) for T(θk,tk):

$$(3.25) \quad T(\theta k,tk) = \frac{tk\theta k \,/\, \lambda i,k}{1 \;-\; tk\theta k \,/\, \lambda p,s}$$

With the true random sample and the Γ attenuation function approximated by (3.24) we obtain from (3.22):

$$(3.26) \quad T(\theta k,tk) = \frac{2tk\theta k \,/\, \lambda i,k}{1 \;-\; 2tk\theta k \,/\, \lambda p,s}$$

In deriving equation (3.26), we have made the additional approximation 1/(1-X)=1+X, X=tk/λ<<1. For a sample displaying intermediate surface roughness we write T(θk,tk) as:

$$(3.27) \quad T(\theta k,tk) = \frac{\alpha tk\theta k \,/\, \lambda i,k}{1 \;-\; \alpha tk\theta k \,/\, \lambda p,s}$$

with $1<\alpha<2$.

This means that the principle uncertainty in the determination of the amount of supported compound k from the intensity ratio Ii,k/Ip,s is a factor of two. In the case of the VG ESCA III, the collection angle of the photo-electrons is approximately 45°. Bearing in mind that (3.24) was obtained assuming a collection angle of 0°, the uncertainty at 45° is somewhat smaller because in this case $\sqrt{2}<\alpha<2$. However, this cannot be

extrapolated to angles much larger than 45° because then the assumption $tk \ll \lambda \cos\beta$ used to derive (3.25,26) no longer holds.

If we apply equation (3.19) for Ii,k and Ip,s and solve (3.27) for θk we obtain:

$$\theta k = \frac{\lambda p,s/\alpha tk}{\lambda p,s/\lambda p,k \quad + \quad \xi \; Ip,s/Ii,k} \qquad (3.28)$$

$$\xi = \sigma i \; Li \; \varepsilon p \; Ni,k \; / \; \sigma p \; Lp \; \varepsilon i \; Np,s$$

Ni,k is the number of atoms i per unit volume in compound k. In adsorption experiments, k is an adsorbate stemming from the gas phase. Therefore we assume the atomic density Ni,k equal to Ns, the density of the substrate. In fact this comprises the definition of the coverage θk as a stoichiometric rather than a geometrical one. So we finally define ξ as:

$$\xi = \sigma i \; Li \; \varepsilon p \; / \; \sigma p \; Lp \; \varepsilon i \qquad (3.29)$$

In our calculations we will assume α to be 1.7±0.25 to account for the unknown surface roughness.

Table 3.3 lists the values of the parameters we have used in equation 3.28 to evaluate surface Cs and oxygen coverages from the measured peak intensity ratios ICs3d/IAg3d and IO1s/IAg3d. Figure 3.13 gives a graphical representation of θCs and θO as a function of these ratios. Cross-sections σ are taken from SCOFIELD /13/, angular asymmetry factors L from REILMAN et al. /19/. Kinetic energies ε are calculated with equation 3.5, values of λ are taken as the average of the values of PENN and SEAH (see figure 3.8). Note that only λp,s has a significant influence in equation 3.28, which value is relatively well known. λAg,O is estimated from measured mean free paths in SiO2, see appendix. As layer thickness tk we take the covalent diameter of the element. However, the ionic diameters of Cs and O differ considerably from these values and are also given.

| peak | σ ($10^5$ barn) | L | ε (eV) | λAg,.. (nm) | tk (nm) |
|---|---|---|---|---|---|
| Cs3d3/2 | 3.51 | 1.21 | 514 | 4.3 | 0.47/0.34 |
| | 2.24 | 1.23 | 745 | 5.0 | 0.47/0.34 |
| Cs3d | 8.60 | 1.21 | 517 | 4.3 | 0.47/0.34 |
| | 5.47 | 1.23 | 750 | 5.0 | 0.47/0.34 |
| O1s | 0.63 | 1.40 | 720 | >3.0 | 0.146/0.28 |
| | 0.40 | 1.40 | 953 | >3.0 | 0.146/0.28 |
| Ag3d | 4.00 | 1.24 | 882 | 1.4 | 2.68 |
| | 2.45 | 1.24 | 1115 | 1.6 | 2.68 |

Table 3.3: Parameters used in equation 3.27. Values for MgKα (upper values) and AlKα radiation are given.

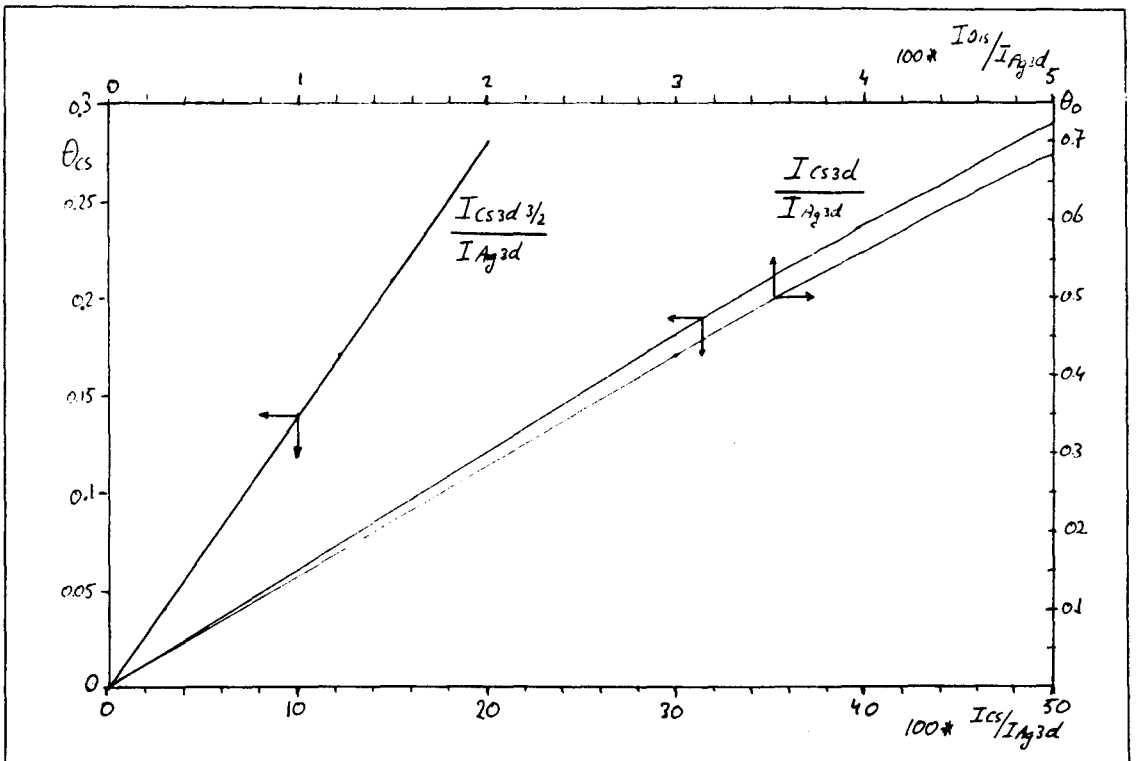


Figure 3.13: Oxygen and caesium coverages as a function of the indicated intensity ratios.

### 3.4.3 Peak intensity determination.

As a measure for the intensity of the relevant XPS signal we take the total peak area of the primary photo-electrons which comprises those electrons that are not ineleastically scattered. The use of peak heights as a measure for the peak intensity is not advisable because changes in peak width and background can cause serious errors in this sort of measurement /29/.

Features in the PE-spectrum generally appear on a continuous background due to multiple inelastic scattering of photo-electrons with initially higher kinetic energies, see paragraph 3.3.5. This continuous background can be easily corrected for by a simple extrapolation from low to high binding energy, as shown in figure 3.14 by the dotted line.

As can be seen in figure 3.14 there is an increase of the background to the high BE side of the PE-peak under the peak envelope. Shirley /30/ attributed this increase to inelastic scattering of photo-electrons from the PE-peak under consideration. This leads to the conclusion that the background under the peak is proportional to the number of primary photo-electrons contributing to it, that is proportional to the fractional peak area. An iterative procedure then yields the appropiate background which is the S-shaped curve shown in figure 3.14. For insulators, where the smallest energy loss of the electrons is the band-gap energy, Shirley's background must be corrected for by a band-gap energy of the S-shaped curve to higher binding energies.

Note that Shirley assumes that a photo-electron can suffer an infinitesimal energy loss. This is a simplification of reality as the main energy loss process is excitation of plasmons with energy 5-10 eV.

A simplification of the Shirley method is to replace the S-shaped curve by a straight line drawn between two points adjacent to the PE-peak. For sharp, narrow peaks either method will give an adequate result /31/. For

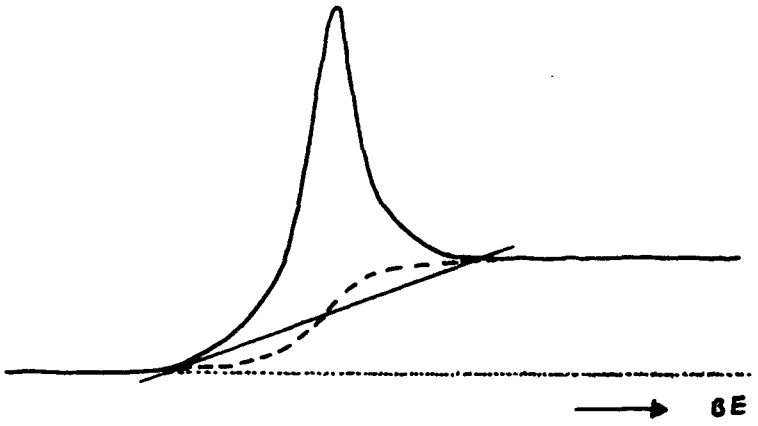


Figure 3.14: Peak area determination, background substraction:
continuous background
Shirley background
straight line method.

general analysis no comparison of the two techniques has yet been made of their respective accuracies over a range of different types of samples.

On the VG ESCA-III the background can be approximated by the straight line method and we will use it troughout our experiments to obtain quantitative results. The accuracy obtained will vary from peak to peak but will be in the order of 5-10%.

### 3.4.4: Compositional depth information in XPS.

Because the XPS signal is not only due to the outermost atomic layer, the XPS spectra contain information about the in depth composition of the material studied. Most commonly used are methods which extract this information from the variation of the inelastic mean free path $\lambda$ with some parameter like electron kinetic energy $\varepsilon$ or detection angle $\beta$. Recently, a method has been suggested which uses the background increase after each photo-electron peak /32-34/.

Another frequently used method is to combine XPS with sputtering, which removes subsequent layers from the sample. However, the latter method is not so reliable (preferential sputtering of some elements, mixing of subsequent layers etc.), is time consuming and essentially destructive to the surface. We will discard this method and describe the other mentioned techniques briefly.

#### Depth information from the energy dependence of the IMFP.

This method relies on the fact that the inelastic mean free path $\lambda$ of the photo-electrons depends on their kinetic energy $\varepsilon$, see figure 3.8. For kinetic energies exceeding 50 eV, $\lambda$ increases monotonically with increasing energy. Thus the ratio of peak intensities of two well (a few hundred eV) seperated photo-electron peaks in the XPS spectrum (with consequently different kinetic energies of the photo-electrons) is sensitive to the depth of the emitting atom underneath the surface.

If I denotes the peak area ratio of two photo-electron peaks of atom α, the depth d at which α is situated onderneath the surface is related to I by:

$$I \propto \frac{\exp(-d/\lambda 1)}{\exp(-d/\lambda 2)} \qquad (3.30)$$

where λ1, λ2 denote the inelastic mean free path of the photo-electrons from the two different levels. This functional dependence is depicted in figure 3.15 for several values of the ratio λ1/λ2.

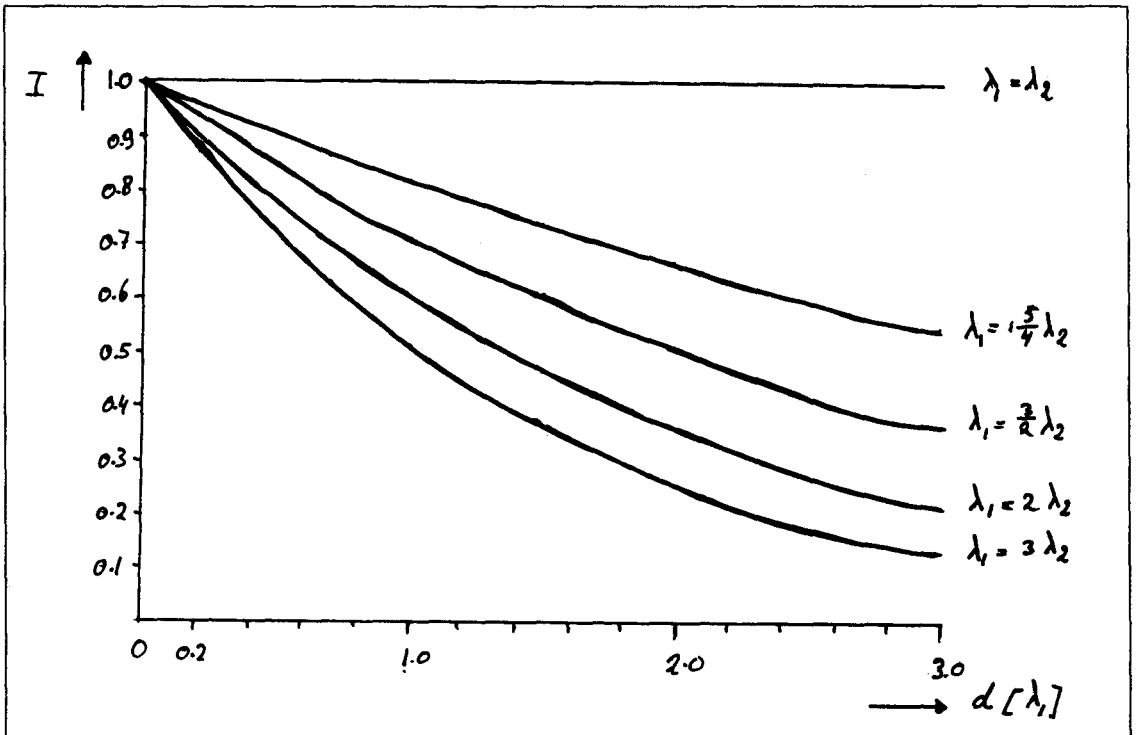


Figure 3.15: Dependence of the intensity ratio I1/I2 of two photo-electron peaks. The photo-electrons have IMFP's of λ1 and λ2 respectively and travelled a distance d in the solid.

Depth composition info from the angular dependence of the signals.

If the electron energy analyser employed has a small acceptance angle, depth information may be obtained from varying this detection angle with respect to the surface normal. With a perfectly flat sample the average escape depth of the photo-electrons is λcosβ with β the angle between surface normal and photo-electron detection direction. So if β is increased, the surface sensitivity is enhanced. The growth of XPS signals from species on top on the surface will exceed that of species underneath the surface, if the latter species is situated too deep underneath the surface its associated XPS signal will even decrease with increasing detection angle. Surface roughness will limit the highest usable angle and therefore the surface sensitivity.

Unfortunately, in the ESCA-III, the detection angle is fixed with respect to the surface normal so we were not able to use this method.

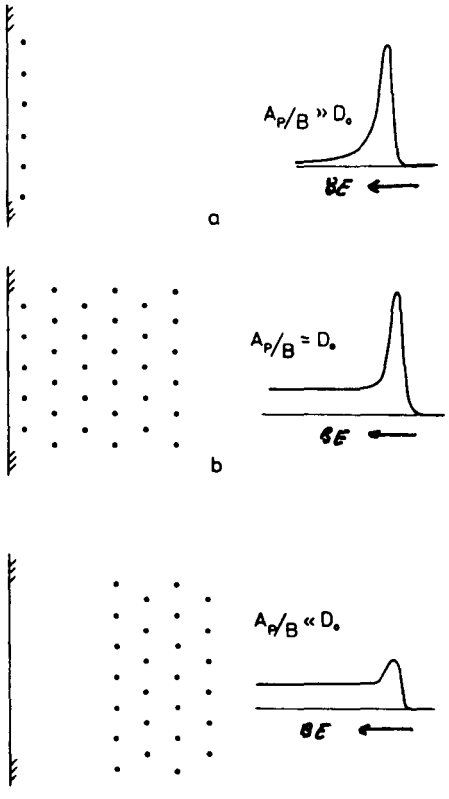


Figure 3.16: The parameter D as a function of the depth composition of the photo-electron emitters
Ap = photo-electron peak area
B = background increase 30 eV to the high BE side.

**Compositional depth information from the inelastic background in XPS.**

This method relies on the fact that photo-electrons originally excited at some depth in the solid lose energy on their way out to the solid surface. The resulting destortion of the energy distribution of emitted electrons depends on the path length travelled by the electrons. Consequently, depth information is contained in the rise of the background to the high BE side of the PE peak.

Recently, TOUGAARD et al. /32-34/ suggested a method to extract this depth information from the measured photo-electron spectrum. They considered the spectrum in the vicinity of the XPS peak where the total energy loss is small (< 50 eV).

The typical energy loss of a photo-electron in an inelastic scattering event is 10-20 eV so inelastically scattered electrons in the vicinity of the PE-peak typically have suffered a limited number of scattering events and will therefore originate from just below (in the order of the inelastic mean free path of the electron) the solid surface.

TOUGAARD defines a parameter D which is essentially the photo-electron peak area divided by the increase in background towards the high BE side of the photo-electron peak. For homogeneous transition metals, D was found to be to first order independent of elemental concentration, peak shape,

metal, peak energy and impurities in the host metal. For these systems, D is a universal constant Do.

Of course the value of Do depends on the method of peak area determination. For a simple straight line background substraction, suggested by TOUGAARD, the theoretical value for Do is 25.2 eV.

For inhomogeneous metals, D is a strong function of the depth composition of the photo-electron emitters, see figure 3.16. It can be used in a qualitative way to determine whether the photo-emitters are burried underneath a layer of dimensions comparable to the IMFP of the photo-electrons or not. Tougaard even suggests a quantitative analysis which allows for the measurement of the layer thickness /32/.

## 3.5 Ultraviolet Photo-electron Spectroscopy (UPS)

Because we used UPS as an additional characterization technique we will briefly treat the elements of this form of photo-electron spectroscopy. In principle, UPS is the same technique as XPS, the difference being that less energetic photons are used as an excitation source. In UPS He-I and He-II radiation is used with photon energies of 21.22 eV and 40.80 eV respectively. He-I and He-II radiation are the result of the transitions:

$$\begin{array}{lll} 2p \longrightarrow 1s & He^{\circ} & h\nu = 21.22 \text{ eV} \\ 2p \longrightarrow 1s & He^{+} & h\nu = 40.80 \text{ eV} \end{array} \qquad (3.31)$$

e.g. in a 1 kV, 10-100 Pa He plasma. The FWHM of this exciting radiation is small (a few meV) compared to the Al,MgKα doublets used in XPS so that high resolutions (ca.10 meV) can be obtained. The relative abundance of He-I and He-II radiation is strongly dependent on experimental plasma conditions (cleanliness of the tube, discharge pressure) but can be judged by the color of the plasma (yellowish white: predominantly He-I, pinkish blue: more He-II). The set-up is depicted in figure 3.17.

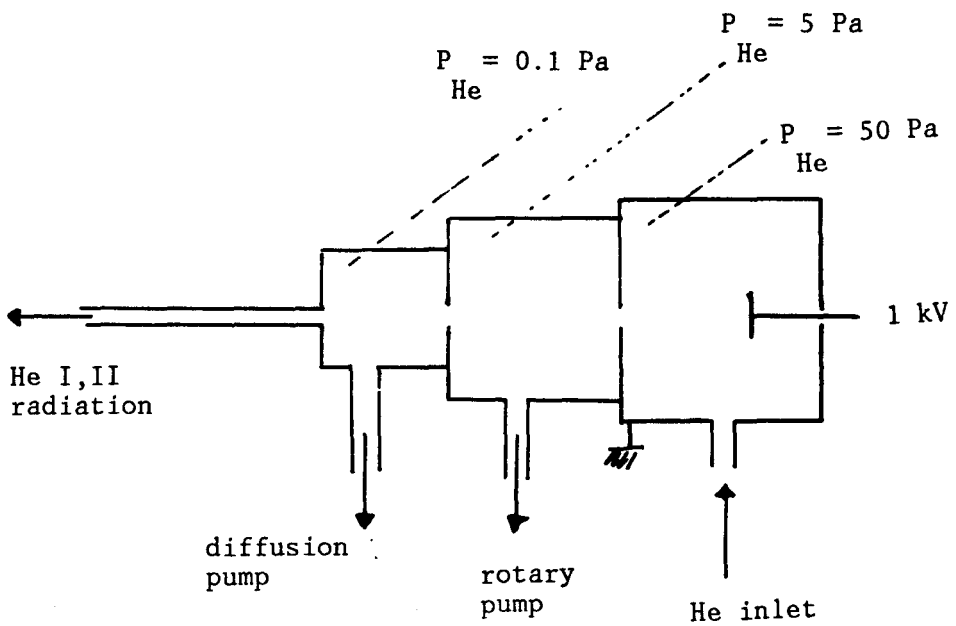


Figure 3.17: Set-up of the He lamp in the VG ESCA-III.

Due to the low photon energy in UPS only valence electrons can be ionized. This precludes a facile element indentification. Also quantification of the UPS signal is more difficult than in XPS, e.g. because of pronounced angular effects in the photo-emission process or resonance effects in the structured final state region of photo-electrons /8/. However, because of its superiour S/N ratio and excellent energy resolution, it can reveal much greater details in the valence band region than XPS. This can be important in certain cases.

We used UPS as an additional technique in the characterization of Cs adalyers on silver; in all other cases we used XPS.

In this chapter a short review is given on recent literature concerning oxygen adsorption on silver. It was not our aim to be complete, a selection was made out of a vast collection. We concentrated on investigations on well defined systems, usually single crystal surfaces, in which modern techniques of surface analysis are used. Besides oxygen adsorption on clean silver surfaces, we will treat the coadsorption system oxygen/caesium briefly.

As said, most recent investigations concern principal single crystal planes like Ag(111) and Ag(110). The (111) and (110) surfaces of silver are depicted in figure 4.1. These surfaces of silver are unreconstructed surfaces so they are equivalent with the correspondig planes in bulk silver. The Ag(110) surface exhibits a relaxation in which the Ag-Ag distance normal to the surface is slightly (2 %) reduced.

The Ag(111) surface comprises a closed packed structure whereas the Ag(110) is more open and exhibits grooves in the (110) direction. The number of surface (first plane) silver atoms is $1.38 \cdot 10^{15}/cm^2$ and $0.85 \cdot 10^{15}/cm^2$ at these faces respectively. Adatom coverages are usually normalized to these numbers.

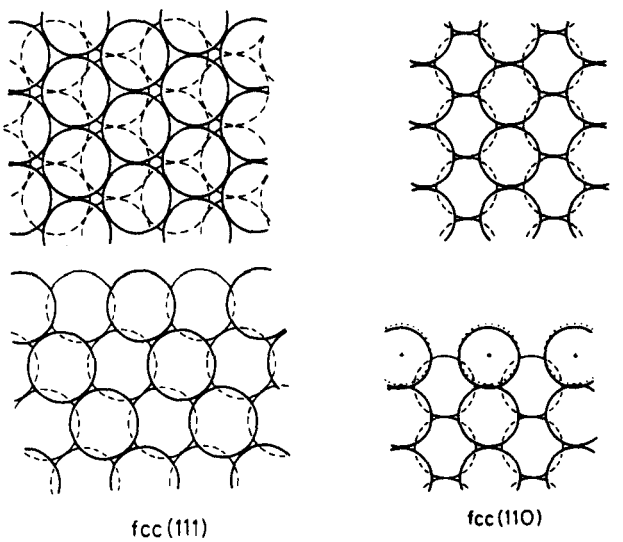


Figure 4.1: The unreconstructed (111) and (110) planes of an fcc lattice like silver in top view (top diagrams) and side view (bottom diagrams). Arrows indicate atomic relaxation.

Although there is no general consensus in what forms oxygen is chemisorbed on different crystal faces and how they can be characterized, it is commonly agreed that at least three different chemisorbed species can be distinguished on a silver surface:

- molecularly chemisorbed oxygen.
- chemisorbed oxygen atoms on top of the silver surface.
- sub-surface oxygen, this is a dissolved form of atomic oxygen restricted to the first atomic layers underneath the surface.

The three species mentioned will be treated seperately in paragraphs 4.1 to 4.3. The influence of co-adsorbed alkali metals will be scrutenized in paragraph 4.4. Because of the inconsistency in literature we will also pay attention to the assignment methods used by the different groups.

## 4.1: Molecular oxygen adsorption on silver.

Adsorbed molecular species are characterized by the presence of an oxygen-oxygen bond co-existing with oxygen-silver bonds. The oxygen-oxygen bond comprises that the adsorbed oxygen must be seen as a form of molecular oxygen on the silver surface. This feature is used to distinguish this species from other adsorbed entities.

BARTEAU and MADIX /35/ were the first to report the existence of adsorbed molecular oxygen on the (110) face of silver. The molecular oxygen state could only be detected by exposing the silver surface to oxygen at low temperature (T<150 K) as the species was not stable at temperatures exceeding 190 K. BARTEAU and MADIX indentified the molecular species by the absence of the 34 amu signal in the mass resolved thermal desorption spectrum of the silver crystal after exposing it to a mixture of $^{18}O2$ and $^{16}O2$ at low temperature.

This method is often used to determine whether dissociative or associative adsorption of poly-atomic molecules has taken place. Consider the underlying case of exposing the silver surface to a mixture of $^{18}O^{18}O$ and $^{16}O^{16}O$. If the chemisorption on the surface is associative the oxygen-oxygen bond will not be broken. After subsequent thermal desorption, the desorbed oxygen will either be $^{18}O^{18}O$ or $^{16}O^{16}O$. If however, the chemisorption is dissociative, the oxygen-oxygen bond is not preserved. After subsequent thermal desorption, desorbed oxygen will be either $^{18}O^{18}O$, $^{16}O^{16}O$ or $^{18}O^{16}O$. The absence of the 34 amu signal excludes mixing of the the oxygen isotopes which means that the indentified adsorbed oxygen species must be considered as being molecularly adsorbed. The low desorption temperature (190 K) of molecular oxygen indicates that it is a weakly bound species.

Atomic oxygen was also found in the low temperature adsorption experiments. This species was more firmly held and desorbed at 580 K. BARTEAU and MADIX found that a sequential filling took place of atomic and molecular adsorption sites respectively. The ratio of coverages of both species was shown to be a strong function of both oxygen exposure and dosing temperature.

BACKX et al. /36/ studied low temperature oxygen adsorption on silver (110) by means of high resolution EELS (Electron Energy Loss Spectroscopy). With this technique, vibrations of adsorbed species can be exited by irradiation of the sample with low energy monochromatic electrons (low energy: eV range). The energy loss of the electrons reflects the excitation energy of specific adsorbate vibrations.

After exposing the single crystal to oxygen at low temperature (113 K) two loss peaks at 30 and 78 meV appeared in the electron energy spectrum. BACKX et al. assigned these peaks to oxygen-metal and oxygen-oxygen vibrations respectively. Due to the presence of the oxygen-oxygen vibration, the adsorbed species was identified as molecular oxygen. The peaks dissapeared after heating the crystal above 170 K at which temperature a new loss peak at 39 meV appeared. In TDS an oxygen desorption peak was seen at this temperature. The peak at 39 meV was assigned to atomic oxygen. It dissapeared at 583 K, at which temperature another oxygen peak was observed in the desorption spectrum. BACKX et al. concluded from this that molecular oxygen partly desorbed and partly dissociated at 170 K. The assignment of the adsorbed species was further substantiated by iso-

topic exchange experiments: no scrambling occured at the 170 K desorption peak whereas total scrambling was observed at the 583 K desorption peak.

The molecular species was truly chemisorbed rather than being physisorbed: the oxygen-oxygen bond of the adsorbed species was considerably weakened (Oxygen-oxygen vibration at 77 meV compared to 194 meV for gas phase oxygen). Furthermore, a saturation coverage of atomic oxygen prior to oxygen adsorption at low temperature precluded the formation of any recognizable amount of molecularly adsorbed oxygen. This shows a marked difference in first and second layer adsorption not encountered in physisorption.

The gross features of these results agree with those obtained by BARTEAU and MADIX /35/. In contradiction with the latter, BACKX et al. found no atomic oxygen adsorption at temperatures below 170 K: no loss peak at 39 meV in EELS could be found at those temperatures.

From their EELS measurements, BACKX et al. derived a model for the nature of the molecular oxygen adsorption. The proposed model is an oxygen molecule lying flat in the grooves of the (110) surface, having a C2v symmetry: any lower symmetry would produce more than two peaks in the ELS spectrum. The proposed model is indicated in figure 4.2.

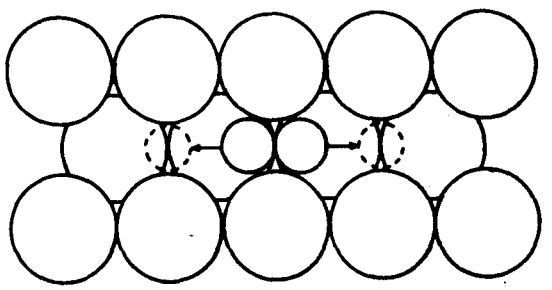

Figure 4.2: Proposed structural model for molecular oxygen chemisorption on Ag(110).

CAMPBELL and PAFFET /37/ studied molecular oxygen adsorption on Ag(110) by means of XPS and TDS. They also found evidence for a molecularly adsorbed species by dosing at low temperature (135 K). With TDS two desorption peaks were recorded, one at 187 K and one at 600 K, reflecting molecular and atomic oxygen adsorbed species. With XPS, the molecularly adsorbed species was characterized by an O1s binding energy of 529.3 eV with a FWHM of 1.5 eV (unmonochromatized MgKα radiation, pass energy 100 eV) relative to Ag3d5/2 at 367.95 eV, FWHM 1.6 eV. In accordance with BACKX et al. cited above, CAMPBELL and PAFFET found no dissociation of molecular oxygen at 130 K. As BACKX et al. indicated, both desorption and dissociation occured at 187 K with relative probabilities of 2:1 respectively. The narrowness of the O1s peak led them to the conclusion that the oxygen molecule must lie flat in the surface; a head-on configuration would produce two O1s peaks or a broader one than observed as a result of the heterogeinity introduced in this configuration.

Molecular oxygen adsorption on Ag(111) is studied less than on Ag(110). GRANT and LAMBERT /38/ claim the existence of a stable di-oxygen species, termed α-state, based on isotopic exchange experiments. Remarkably, the species desorbed at 380 K and could be detected by dosing at 300 K. These values lie 200° above those obtained for Ag(110). The α-state could only be populated if the oxygen dosing pressure exceeded $10^{-2}$ Torr and was

always accompanied by a much larger (app. 8 times larger) amount of a so-called β-state, desorbing at 580 K and indentified as atomic oxygen. The population of the α-state could be enhanced by increasing the amount of sub-surface oxygen in the sample.

In XPS the two states could be distinguished from their O1s binding energies: 532.6 and 529.8 eV for the α and β-state respectively. The larger width (app. 2.5 eV) of the 532.6 eV signal as compared to the 529.8 eV signal was explained assuming a head-on configuration of the oxygen molecule on the surface (see above). By increasing the electron detection angle with respect to the surface normal, GRANT and LAMBERT found an increase of the 532.6 eV signal and a decrease of the 529.8 eV and O(KLL) Auger signal. They concluded that the α-state resided on top of the surface whereas the β-state was an embedded species.

GRANT and LAMBERT explained the minimal pressure needed to obtain the α-state as follows. The assumption is made that molecular oxygen adsorption requires a single isolated adsorption site whereas neighbouring two-fold sites are filled with atomic oxygen. If further the assumption is made that atomic oxygen has a rather low surface mobility at 300 K, at low pressure the net accumulation rate of atomic oxygen is sufficiently low to allow the overlayer formed to relax. With attractive lateral interactions between atomic oxygen species /39/ this means the vanishing of single adsorption sites needed for molecular oxygen adsorption. At higher pressures, the atomic oxygen accumulation exceeds the relaxation rate, so single vacancies are created and molecular adsorption can take place.

CAMPBELL /2/ duplicated the experiment of GRANT and LAMBERT (dosing at 300 K, 1 Torr) but was unable to find a di-oxygen species desorbing at 380 K. His thermal desorption spectrum showed a peak at 580 K, indicative of atomic oxygen and broad desorption peaks at 350 - 450 K assigned to induced impurities as a result of the exposure conditions. However, the discrepancy between the work of CAMPBELL and GRANT and LAMBERT cannot solely be attributed to impurities as the latter showed clear evidence for the existence of a di-oxygen species. More experimental work is needed to shed some light on this discrepancy.

By dosing at 147 K CAMPBELL found simular results as obtained with Ag(110) /35-37/. An adsorbed di-oxygen species desorbed at 217 K, at a somewhat higher desorption temperature compared to Ag(110) (170-190 K). Little disociation (2%) took place during desorption as was evident from a small desorption peak at 580 K (atomic oxygen). The sticking probability of the species was much lower than on Ag(110) since saturation required a 200-fold increase of dose. A saturation dose of approximately $5\ 10^{5}$ L yielded a coverage of 0.5, simular to a reported value of 0.6 for Ag(110) /10/. With this calibration an initial sticking probability of $5\ 10^{-6}$ was derived for Ag(111) at 147 K as compared to $7 \cdot 10^{-4}$ for Ag(110) at 130 K.

Finally, CAMPBELL /2/ proposed a three step adsorption process for oxygen on silver (111) and (110): a physisorbed state O2,p, a chemisorbed molecular state O2,a and a chemisorbed atomic state Oa which are sequentially accessed, see figure 2.1:

$$O2,g \rightleftharpoons O2,p \rightleftharpoons O2,a \rightleftharpoons Oa$$

The physisorbed state desorbs below 50 K /61/ with very little dissociation. Its desorption temperature suggests a heat of adsorption less than 12 kJ/mol. CAMPBELL explained the low sticking probability of molecular oxygen chemisorption by assuming a potential barrier between the physisorbed and chemisorbed state which makes the molecular chemisorption an activated process with respect to the gas phase. The calculated activation barrier is 12 and 6 kJ/mol for Ag(111) and Ag(110) respectively. The bottleneck of accomodation of oxygen atoms on the silver surface is therefore the transition from the physisorbed precursor to the chemisorbed molecular state rather than the transition from the chemisorbed molecular to

chemisorbed atomic state. According to his evaluation, the transition from molecular to atomic oxygen is not activated.

This is corroborated by measurements of GRANT et al. /38/ who showed that no appreciable increase in sticking probability occured after sputtering the silver surface. If the transition from chemisorbed molecular to chemisorbed atomic oxygen would be activated (and therefore the bottle neck) the induced adsorption sites induced by sputtering having higher adsorption energies (steps, kinks etc.) would lower this activation barier and hence would increase the sticking probability.

However, the transition between O2p and O2a can hardly be imagined to be activated because of the rather shallow potential wells involved and the small separation between them on the raction coordinate /40/. Another possible explanation of the small dissociative sticking probability of oxygen on silver and the large difference found on Ag(110) and Ag(111) may be the influence of steric factors in the accomodation process of chemisorbed molecular oxygen.

In a similar way as in the desorption process (see paragraph 2.9) the transition from the precursor O2p state to the chemisorbed O2a state depends on the frequency of bond rupture, which depends on the ratio of partition function of the physisorbed O2p complex and that of the transition complex to the chemisorbed O2a state.

If we now assume that the transition complex has a much smaller number of degrees of freedom, the frequency $\nu$ in equation 2.15 would be correspondingly lower and most molecules would leave the precursor state before they could be transferred into the O2a state. The decrease in degrees of freedom may be envisaged as a certain stereographic orientation of the precursor molecule required in order to enable it to make the transition to the O2a state.

Also the much lower sticking probability on the Ag(111) surface can be explained by this hypothesis. We only have to assume a larger number of degrees of freedom of the precursor state on the Ag(111) surface, which is reasonable because of the less pronounced variation in surface potential (see figure 2.2) on the more densely packed and atomically smooth Ag(111) surface.

From the reviewed literature the following characteristics of molecular oxygen adsorption on silver can be derived:

- On Ag(110) molecular oxygen is adsorbed at temperatures below 150 K. The reported desorption temperatures are 170-190 K. The adsorbed molecular species is chemisorbed and lies flat in the grooves of the (110) surface. The XPS binding energy of the species is 529.3 eV. The sticking probability is ca. $7 \cdot 10^{-4}$.

- On Ag(111) contradicting results are found. A molecular species is reported which desorbs at 380 K, with a XPS BE of 532.6 eV and in a head-on configuration. Other groups report desorption temperatures simular to those obtained on Ag(110). These contradictions as yet have not been convincingly explained. Reported values of sticking probabilities on Ag(111) are low: ca. $5 \cdot 10^{-6}$

## 4.2: Atomic oxygen adsorption on silver.

The dissociative sticking probability for oxygen on silver is low. With a value of $5\text{-}30\cdot10^{-4}$ it is largest on Ag(110) among the principal crystal faces. Because of the easier characterization of adsorbates with higher sticking probabilities, the Ag(110) surface is studied in most detail.

MENZEL et al. /41,42/ made an extensive LEED study of the oxygen uptake of Ag(110) at room temperature and above, complemented with AES and work function measurements. A succesion of patterns due to (n*1), n=7.....2 LEED structures developed with increasing oxygen exposure at room temperature, which were believed to represent ideal coverages of 1/n. An exposure in excess of $10^4$ L was neccessary to obtain the saturation (2*1) structure. All superstructures dissapeared irreversably after heating the crystal above 550 K. Slightly heating the crystal to temperatures below 470 K, to enhance the mobility of the adatoms, led to a conversion of the sharp LEED spot pattern to streaks, showing good order in the [100] direction, perpendicular to the grooves in the (110) surface and poor order in the [110] direction, along these grooves.

From these LEED results MENZEL et al. concluded that oxygen atoms form chains perpendicular to the grooves in the (110) surface, even at low coverages, which shows an attractive interaction in the [110] direction. The distance between the chains were always as many lattice constants as the coverage allowed for (n for $\theta=1/n$), showing repulsive interaction along the surface channels. The model is depicted in figure 4.3a.

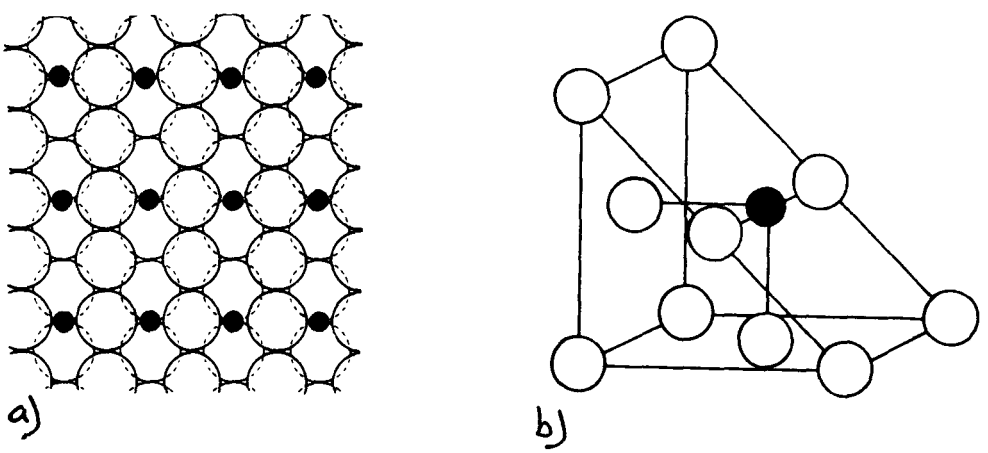


Figure 4.3: a) Proposed structural model for atomic oxygen chemisorption on Ag(110) on the basis of the LEED (2*1) structures.
b) Position of the oxygen atom in the (110) groove according to ISS measurements.
Oxygen atoms are indicated by full circels.

HEILAND et al. /43/ studied the oxygen adsorption on Ag(110) by means of low energy $He^+$ scattering (ISS), LEED, and AES. Studying the LEED p(2*1) oxygen overlayer structure with ISS they found a strong azimuthal anisotropy in the scattered $He^+$ yield. The scattered ion intensity in the [110] direction, parallel to the throughs in the Ag(110) surface, by far exceeded that in the [100] direction, perpendicular to these channels.

An obvious explanation for this feature is that the oxygen atoms are shadowed by surrounding silver atoms. According to the authors the oxygen atom is situated between two ridge silver atoms, bridging two second plane sil-

ver atoms at the bottom of the through. The height of the oxygen atom was calculated as slightly below or in the plane of the first layer silver atoms, depending on the scattering potential adopted. The model proposed is depicted in figure 4.3b. Clearly in this configuration the oxygen atom is shadowed in the [100] direction by the ridge silver atom whereas no shadowing takes place in the [110] direction.

To arrive at their model, the authors excluded the possibility of an oxygen induced reconstruction of the silver surface. This assumption was based on the fact that a drastically different azimuthal dependence occured in previous ISS work on the p(2*1) oxygen overlayer on Ni(110) in which case reconstruction does take place /44/. Another argument against reconstruction was that the sequential appearance of the (n*1) LEED structures (n=7....2) with increasing oxygen exposure would mean a continuous reordering of the silver surface, which is not very credible. These ISS results corroborate the findings of MENZEL et al. cited above.

ROVIDA et al. /45/ studied the Ag(110)/oxygen system with LEED and AES together with TDS albeit at higher oxygen pressures (0.1-1 Torr). They could reproduce the p(n*1) n=4.....2 LEED structures found by MENZEL et al. but only pursued a detailed analysis of the p(2*1) structure at high oxygen adsorption pressure. Both AES and TDS indicated that relative to the (n*1), n>2 structures too much oxygen was contained in the (2*1) pattern to account for the model of ideal 1/n coverage (for which two times as much oxygen should be contained in the (2*1) structure than in the (4*1) structure). To explain the (2*1) structure, they proposed a mixed silver-oxygen adlayer roughly corresponding to a surface Ag2O phase and resulting in a coverage of unity. This structure would explain the high oxygen amount found by AES and TDS. The proposed model is depicted in figure 4.4.

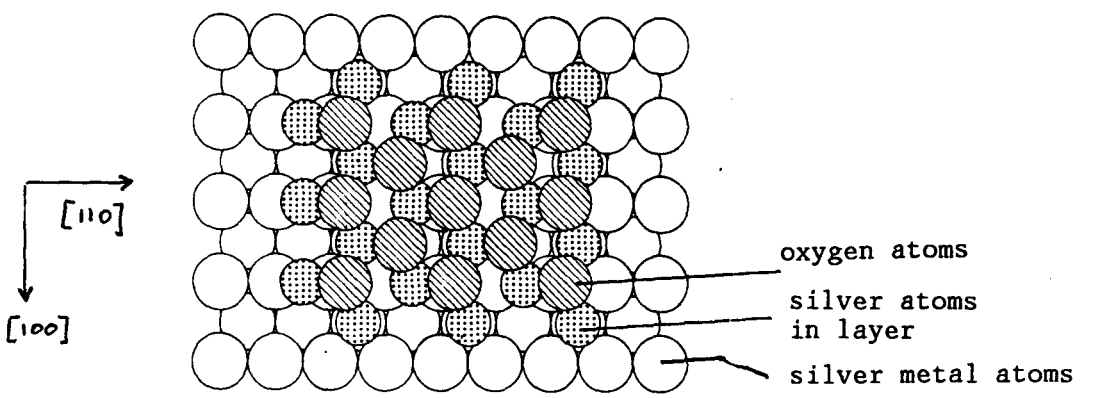


Figure 4.4: Proposed model for an oxygen reconstructed silver (110) surface as explanation of the observed (2*1) LEED pattern.

According to CAMPBELL et al. /37/ a more obvious explanation for this feature is island formation in the LEED sructures with n>2 leading to an overestimation of the actual coverage if θ=1/n is assumed. Island formation is substantiated by the shift to higher desorption temperatures with increasing oxygen coverages /39/, indicative of a corresponding increase in heat of adsorption hence in a thermodynamical driving force for island formation.

Moreover, CAMBELL et al. indentified a new form of oxygen adlayer structure characterized by a LEED c(6*2) pattern by dosing at 485 K and 50 Torr oxygen. Because of their previous calibration of the oxygen TDS peak area to the p(2*1) O pattern, for which θ=0.5, they were able to calculate the oxygen coverage in this newly formed adlayer to be 0.67. This may sound

peculiar because of the rather large mesh involved. However, the observed c(6*2) pattern only means a long range order of this type, short range order may be of another more densely packed type. These islands of higher coverage cannot be seen in LEED because of the coherence lengths involved. What remains is the long range order best visualized by superimposing (6*2) meshes in a random fashion.

By heating the c(6*2) structure to 560 K, it changed into the well known p(2*1) structure. In TDS, the c(6*2) structure showed an additional peak at 560 K to the spectrum of the (2*1) structure, which showed a single peak at 605 K.

In XPS the newly formed oxygen adlayer was characterized by a composite O1s peak which could be syntesized with the usual low coverage atomic oxygen peak at 528.1 eV (FWHM 1.7 eV) and a slightly shifted contribution at 528.3 eV (FWHM 1.9 eV) attributed to the additional oxygen in the c(6*2) structure. The above mentioned finding severely undermines the model proposed by ROVIDA et al. The obtained coverage of 0.67 by CAMPBELL et al. must be considered as the maximum value achieved till to date.

Atomic oxygen on Ag(111) is difficult to prepare /41/ because of the very low dissociative sticking coefficient for oxygen adsorption on this plane. Values of $10^{-5}$ to $10^{-6}$ for the initial sticking probability So have been reported /2,46,47/.

For dissociative chemisorbed oxygen on top of the surface it is known that it readily reacts with CO to produce CO2 /47/. The background CO pressure, enhanced during oxygen exposure because of reaction of oxygen with contaminants adsorbed on the walls of the vacuum system, together with the low sticking probability of oxygen on silver(111) can completely inhibit the formation of any recognisable amount of adsorbed oxygen. From simple kinetic gas theory it follows that, assuming a reaction probability of unity and an initial sticking probability of oxygen on silver of So, the oxygen pressure during the adsorption experiment must exceed the CO background pressure by a factor of approximately 1/So to obtain an oxygen adlayer (see also equation 2.1). If the sticking probability decreases with increasing coverage, competition of CO can limit the maximal achievable oxygen coverage.

ROVIDA et al. /49/ made an extensive study of the Ag(111)/oxygen system with several techniques under which LEED, AES and thermal desorption. No oxygen uptake could be measured at pressures less than $10^{-3}$ Torr. By dosing at higher pressures, an oxygen desorption peak was seen at 550 K, indicative of adsorbed atomic oxygen. With LEED a p(4*4) superstructure was found only at dosing temperatures exceeding 375 K. No other LEED structures could be indentified, not even after dosing at 10 Torr oxygen pressure.

According to the authors, ordening into the (4*4) structure did not occur at temperatures below 400 K, probably the result of unsufficient mobility of the adatoms at these temperatures. Figure 4.5 indicates the visibility range of the (4*4) structure as a function of dosing pressure and temperature. The ordered oxygen adlayer pertained to exist till its desorption temperature (550 K).

The authors interpreted the (4*4) structure as the (111) face of a single slab of Ag2O. Ag2O has a so-called cuprite structure in which the oxygen atoms lie on a bcc lattice and the silver atoms are on a fcc lattice such that every silver atom is half-way between two oxygen atoms, see figure 4.6a. The Ag(111) structure consists of a trilayer repeat unit stacked as ABCABC..... Each trilayer consists of a hexagonal Ag layer (Ag-Ag distance 0.335 nm) surrounded by two hexagonal oxygen layers (O-O distance 0.669 nm) at 0.068 nm distance, see figure 4.6b. The diagonal of the unit mesh of the oxygen layer in Ag2O(111) is within 0.5% four times the edge of the

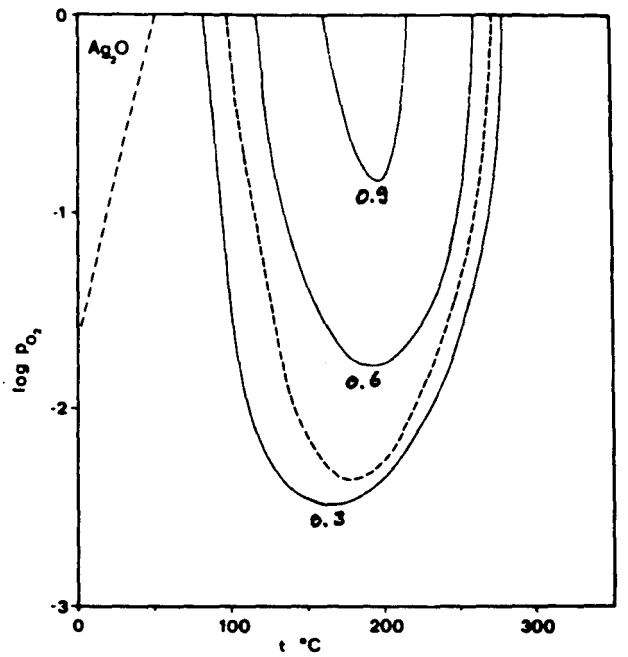


Figure 4.5: Visibility range of the (4*4) LEED structure on Ag(111) together with the stability of bulk Ag2O. Also shown are lines of constant oxygen coverage θ.(—)

unit mesh of the Ag(111) surface. The (4*4) structure therefore would be the periodic element in common between the Ag(111) and Ag2O(111) planes.

GRANT and LAMBERT /38/ also found the (4*4) structure after dosing at elevated temperatures (400-450 K) and high pressures (1-2 Torr). They substantiated the model outlined above by their XPS results. The O1s peak at 529.8 eV BE, which they attributed to atomic oxygen, decreased with increasing off-normal detection, indicative of an embedded rather than an "on top" adsorbed entity. The BE of the species is 1.5 eV higher than of the corresponding oxygen species on Ag(110). However, the picture resembles that of the adsorbed state of oxygen on Cu were incorporation in the metal occurs on the (111) surface but no embedding was found on the (110) face /38 and references therein/. Furthermore, the O1s BE of bulk Ag2O is 529.0 eV which also points to shifting towards higher BE values in an Ag2O like environment.

GRANT and LAMBERT further pointed out that the unordered oxygen uptake at 300 K obeys classical Langmuir kinetics, in which the sticking probability $S(\theta)$ is given by $S(\theta)=So(1-\theta)^2$ for dissociative adsorption of a di-atomic molecule. This means that the oxygen adatom must be immobile at this temperature, in agreement with the proposal of ROVIDA et al. /49/.

CAMPBELL /2/ studied the oxygen uptake of Ag(111) with TDS, AES, XPS and LEED. His TDS and LEED results after dosing at 490 K and 5 Torr, 20 seconds, are in agreement with those described above. The measured AES O(KVV) to Ag(MNN) ratio was the same ($2 \cdot 10^{-2}$) as that obtained with the c(6*2) pattern previously reported for Ag(110), for which $\theta=0.67$ /37/. This allowed him to calculated the oxygen coverage in the well developed (4*4) structure as 0.41.

The p(4*4) structure could be seen at much lower coverages (e.g. after desorbing most of the adsorbed oxygen amount) indicating nucleation of the adatoms into (4*4) islands, in agreement with the finding of GRANT et al. /38/ of attractive lateral interactions between the oxygen adatoms.

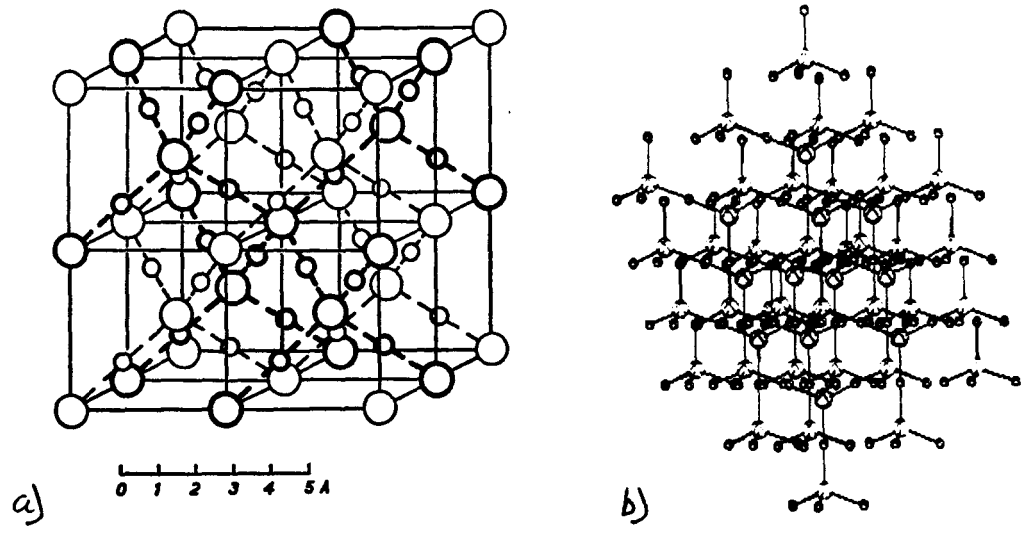


Figure 4.6: a) The cuprite structure of Ag2O. Small spheres represent Ag, larger ones oxygen atoms.
b) Looking along the (111) plane of Ag2O.

Campbell questions the assignment of the (4*4) structure to the formation of an Ag2O slab. To be consistent with the oxygen coverage he derives for the (4*4) structure (0.41), a trilayer of Ag2O must be assumed. Such a structural model can not explain the absence of any significant reactivity difference with CO of the two oxygen layers whereas also in XPS two peaks might be expected. In XPS, the O1s BE of the atomic oxygen species found by CAMPBELL is 528.2 eV, close to the value of 528.1 eV on Ag(110) measured by the same author /37/, in contradiction to the value reported by GRANT and LAMBERT (529.8 eV). This discrepancy as yet has not been convincingly explained.

From the above, a number of properties of atomically adsorbed oxygen can be summarized:

- On Ag(110) oxygen atoms form ordered adlayers in the form of chains perpendicular to the surface grooves, showing atractive interaction in this direction and repulsive interaction along the grooves. The oxygen atom location is depicted in figure 3.3. Atomic oxygen desorbs at 580-605 K. In XPS atomic oxygen is characterized by a BE of 528.1 eV. The initial sticking probability is small ($5\text{-}30 \cdot 10^{-4}$).

- On Ag(111) only one ordered structure was seen, explained by formation of a single Ag2O slab. However, this explanation is not commonly agreed upon. Reported O1s binding energies differ: as well as 529.8 eV as 528.2 eV was observed. The oxygen species at 529.8 eV seems to be related to an imbedded species whereas the 528.2 eV may tentatively be assigned to a species adsorbed on top of the surface. Measured sticking probabilities are small: in the order of $5 \cdot 10^{-6}$

## 4.3: Subsurface oxygen on silver.

From the three chemisorbed oxygen species on silver, subsurface oxygen remains the most poorly characterized species. It is referred to as "unreactive" oxygen, dissolved oxygen or subsurface oxygen. We have adopted this last name because it reflects best the very nature of the species.

ROVIDA et al. /49/ were the first to make a systematic investigation on subsurface oxygen on Ag(111). Measurable quantities of subsurface oxygen developed after dosing at temperatures greater than about 475 K. The species was characterized by a broad desorption peak around 775 K, whereas the atomically adsorbed oxygen, characterized by its LEED (4*4) structure, desorbed already at 550 K. After desorbing only this latter species by heating to 550 K, the workfunction remained 0.2 eV higher than that on the clean silver surface. Complete recovery of the surface characteristics was attained only after heating above 775 K. The high temperature desorption peak oxygen never give rise to any recognisable LEED pattern. The formation of bulk oxide was excluded because of its instability at the temperatures and pressures used, see figure 3.5.

BACKX et al. /36/ made an extensive study of subsurface oxygen on Ag(110). After dosing 800 L oxygen at 300 K, a single desorption peak at 583 K was measured, indicative of atomic oxygen. Repeating the treatment enhanced the desorbed amount by 70%. Only after six adsorption-desorption cycles, the amount of desorbed oxygen did not increase any more. Sputtering and annealing the sample before adsorption restored the initial imbalance. BACKX et al. explained their findings by assuming a diffusion of atomic oxygen into subsurface sites during thermal desorption (heating rate during TDS: 4.6 K/s) until all subsurface sites were occupied. Mere dissolution into the Ag bulk was excluded from the described saturation behaviour.

BACKX et al. substantiated their theory by dosing $8 \cdot 10^4$ L $^{16}O^{16}O$ at 475 K on sputtered and annealed Ag(110) (without subsurface oxygen). After subsequent evacuation and thermal desorption up to 725 K, $^{16}O^{16}O$ desorbed at 583 K. No oxygen could be detected anymore with LEED and EELS after the heat treatment. Next the crystal was exposed to 800 L $^{18}O^{18}O$. In the recorded TDS spectrum $^{18}O^{18}O$, $^{18}O^{16}O$ and $^{16}O^{16}O$ were seen at 583 K. So a considerable amount $^{16}O$ remained on Ag(110) after dosing $^{16}O$ and subsequent TDS to 725 K. This oxygen did not reside on top of the Ag(110) surface as was evident from LEED and ELS. These findings convincingly show the presence of a subsurface oxygen species, which exchanges with atomic surface oxygen. From the weakening of the 39 meV loss in EELS, indicative of atomic oxygen, when heating the crystal to temperatures above 425 K, they concluded that diffusion into subsurface sites commences at the latter temperature.

Subsequent investigations of BACKX et al. /50/ revealed the presence of a second type of subsurface oxygen after exposing the Ag(110) face to $10^3$ Pa oxygen for 30 minutes at 470 K. After cleaning off the atomic oxygen formed with CO, no adsorbed oxygen was found on the surface anymore (LEED, EELS). Heating the crystal to 470 K resulted in the reappearance of atomic oxygen on the surface (LEED, EELS) which obviously was stored in subsurface sites. This subsurface oxygen (termed weakly bound) differed from the previously reported /36/ (termed tightly bound) by its transfer ability to surface atomic oxygen at elevated temperature. The tightly bound subsurface oxygen was now believed to be related to impurities in the silver such as silicon. These impurities became visible in EELS after the treatment at $10^3$ Pa oxygen and heating in a TDS scan.

No evidence was found for weakly bound subsurface oxygen after dosing oxygen at UHV pressures so probably a minimum coverage and thus pressure is a requisite for its formation.

CAMPBELL /37/ too reported on subsurface oxygen on Ag(111). This species was characterized by an oxygen-TDS desorption peak at 590 K. The subsurface oxygen could be transferred to the surface to yield surface atomic oxygen as became evident by cleaning it off with CO and following the CO2 evolution. CO2 continued to be formed over a broad temperature range (460-630 K). In XPS, the subsurface oxygen was characterized by an O1S BE of 528.5 eV, FWHM 2.0 eV.

This O1s BE for subsurface oxygen was not found by JOYNER and ROBERTS /51/. They observed a subsurface oxygen species on silver foil at a binding energy of 530.3 eV in an in situ XPS measurement. It developed after high pressure (1 Torr) oxygen admittance at 473 K. The subsurface nature was evident from the associated signal intensity decrease with increasing off-normal detection.

Till to date, the structural model for subsurface oxygen remains vague. This is not so surprising since the very nature of the subsurface species precludes indentification with techniques determinating structure like LEED and ISS.

BACKX et al. /50/ suggest bonding in dislocation planes or directly beneath the outermost layer of silver atoms for their weakly bound subsurface oxygen. The latter suggestion is corroborated by the enhancement of adsorption of species like ethene when subsurface oxygen is present. However, the sticking probability of oxygen is not altered by the presence of subsurface oxygen.

The situation of subsurface oxygen underneath the first atomic layer would require a major reorganisation of silver atoms because of the densely packed structure at the surface e.g. the "holes" in the (111) face which at first glance might be suitable as subsurface sites are far too small to accommodate an oxygen ion or even an oxygen atom.

More investigations on subsurface oxygen are necessary to reveal its structural incorporation in the silver lattice. A technique such as SEXAFS (Surface Extended X-ray Adsorption Fine Structure) seems a suitable tool to scrutinize the direct surrounding of an embedded species like subsurface oxygen. To our knowledge, till date no such investigations have been reported.

In summary, subsurface oxygen is characterized by the following:

- It has a high desorption temperature: reported values vary from 590 K to 775 K. The variation may be due to different kinds of this species, namely a tightly bound and a weakly bound form.
- Subsurface oxygen exchanges with atomic oxygen (both sorts) and can be transferred to atomic oxygen at elevated temperatures (only weakly bound).
- The location of subsurface oxygen remains vague, a situation underneath the outermost surface atomic layer is suggested.
- In XPS subsurface oxygen was characterized by a BE of 528.5 eV (CAMPBELL) and 530.3 eV (JOYNER).

### 4.4: Oxygen adsorption on alkali predosed silver.

Adsorption of alkalis on the silver surface drastically influences the latter's properties with respect to oxygen chemisorption. Several groups investigated various alkali-oxygen co-adsorption systems on silver, ranging from Li-O till Cs-O /52-59/. The smaller alkalis (Li, Na, K, ionic radii 0.08, 0.10, 0.13 nm) are shown to diffuse readily into the Ag bulk /52,57,58/.

GARFUNKEL et al. /52/ studied the coadsorption of sodium and oxygen on Ag(100) by means of XPS, UPS and HREELS (High Resolution EELS). Upon Na adsorption they found a monotonic decrease in work function to a value of 2.4 eV below that for clean Ag(100). Such a decrease is known to occur

because of strong ionic chemisorption of alkali metals (see paragraph 2.7).

Subsequent oxidation of an Na adlayer (θNa=0.2) resulted in an immediate increase in workfunction (0.8 eV) and decrease in Nals BE (also 0.8 eV) during the first Langmuir oxygen exposure. In XPS an Ols peak developed around 529.8 eV which broadened to the low BE side upon prolonged oxygen exposure. Heating the co-adsorption layer showed a decrease in Nals intensity but less than in the oxygen free case, implying a cooperative interaction between oxygen and sodium, may be mutual dissolution into the Ag bulk.

Garfunkel et al. concluded that oxygen adsorption on Na predosed Ag(100) occured in two stages. The first stage compromises formation of a sort of NaOx complex, characterized by a large increase in workfunction and a large decrease of Nals BE. In the second stage oxygen adsorption on silver takes place, both atomically and molecularly (evident from an HREELS peak at 77 meV).

The larger alkalis (Rb, Cs, ionic radii 0.15 and 0.17 nm) do not show pronounced dissolution albeit that some groups indicate diffusion into subsurface sites /54,56/.

GRANT and LAMBERT /55/ examined the Ag(111)/Cs/oxygen system by LEED, TPD and AES. They followed the Cs uptake at the Ag(111) surface by AES and found that Cs multilayers developed beyond θCs=0.12. They concluded this from distinct breaks seen in the Cs uptake against the Cs deposition curve and the development of additional low temperature peaks in the thermal desorption spectrum which yielded an desorption energy of 90 kJ/mol, close to the Cs bulk sublimation enthalpy (78.6 kJ/mol). Dissolved Cs was excluded based on the absence of a high temperature Cs desorption peak.

Saturation of the formed Cs adlayers with oxygen ($5 \cdot 10^7$ L) changed the Cs adlayer drastically. At low Cs coverages (θCs=0.05) the oxygen-TDS spectrum resembled that of clean Ag(111) as reported earlier by the same authors /75/. Even at high Cs loadings (beyond a monolayer), the characteristic clean-silver-oxygen desorption peak was seen, together with complex additional peaks. Additionally, the Cs desorption peak shifted towards higher temperatures; Cs desorption started only after virtually all oxygen was thermically removed from the surface. The Cs to O stoichiometry was calculated as 4.4 to 1.

As an explanation for the oxygen associated with bare Ag sites, even at high Cs loadings, GRANT and LAMBERT introduced an oxygen induced redistribution of the original Cs films, resulting in the growth of three dimensional micro crystallites of a CsO phase. Decomposition of Cs-oxides would then explain the complex oxygen desorption features seen at high Cs coverages. A similar assignment was made in previous work by GODDARD et al. on the Ag(111)/Rb/O system /56/. The shift towards higher Cs desorption temperatures after exposure of the Cs adlayer to oxygen was explained by the formation of a Ag-Cs surface alloy during thermal decomposition of the Cs oxides.

CAMPBELL /54/ investigated the Ag(111)/Cs/O system with XPS,AES,LEED and TDS. In contrast to GRANT and LAMBERT he could not find Cs multilayer formation at room temperature. However, Cs multilayers were formed by Cs deposition at 160 K. These multilayers desorbed in a sharp peak at 320 K, yielding a desorption energy of 78.1 kJ/mol.

Cs sub-monolayers showed a broad desorption peak extending from 320 K to beyond 800 K. A saturation coverage at 300 K resulted in a LEED (2*2) pattern after cooling the sample to 200 K to reduce the mobility of the Cs adatoms. The LEED pattern was interpreted as a uniform coverage of 0.25, giving a Cs-Cs spacing 95% of that in Cs metal.

After exposing the Cs adlayer to ethylene epoxidation reaction conditions (20 Torr ethylene, 150 Torr oxygen) Cs and oxygen were found on the silver surface with AES. By calibration to the O(KVV) intensity acquired earlier for the (4*4) oxygen overlayer on clean Ag(111) for which $\theta$=0.41 /2/, oxygen coverages could be calculated as being in the range 0.70-0.78 depending on the Cs loading. The stoichiometry of the formed Cs-O compound was CsO3, in agreement with the XPS findings of AYYOOB et al. /53/. The AES O(KVV) and Cs(MNN) signal shapes were markedly different from the ones observed for the adsorbed atomic oxygen on clean Ag(111) and pure Cs adlayers respectively, indicating a change in chemical nature of the adsorbed species.

The CsO3 compound gave a Cs-TDS exhibiting three distinct peaks, around 600 K ($\alpha$ and $\beta$ peak) and around 700 K ($\gamma$ peak). The $\alpha$ and $\beta$ peak were attributed to the decomposition of Cs oxides whereas the $\gamma$ peak revealed the presence of dissolved Cs. The latter assignment was substantiated by the reduced detectibility of this species with AES as compared to TDS. The oxygen TDS showed two desorption peaks almost in coincidence with the $\alpha$,$\beta$ Cs doublet. All oxygen was removed at 650 K.

With LEED, the CsO3 compound gave rise to a $(2\sqrt{3}*2\sqrt{3})R30^{\circ}$ pattern. This pattern could also be obtained in UHV by dosing oxygen to a Cs overlayer. The TDS spectrum of the so formed co-adsorption layer was similar to the one described above.

The similarity between oxygen desorption temperatures on clean Ag(111) (580 K) and Cs dosed Ag(111) (ca. 600 K) led CAMPBELL to the conclusion that the major bond of this species must still be with the silver substrate. Obviously, the simultaneous desorption of Cs and oxygen can be attributed to the decomposition of the CsO3 compound.

The findings of both groups are contradictionary in many respects. As yet the discrepancies have not been convincingly explained. We summarize as follows:

- GRANT and LAMBERT find Cs multilayer formation at room temperature for coverages exceeding 0.12. The oxygen saturated Cs layer has a stoichiometry of Cs4.4O. Bare silver sites are available even at high Cs loadings. No evidence was found for dissolved oxygen; the high temperature Cs desorption peak was assigned to a Cs-Ag surface alloy.

- CAMPBELL finds multilayer desorption at 320 K. A saturated Cs adlayer has a coverage of 0.25 (LEED). The oxygen saturated Cs layer has a stoichiometry of CsO3. The major bond of the oxygen is still with silver, not with Cs. The high temperature Cs desorption peak was assigned to dissolved Cs.

## 5.1: Data acquisition.

The spectrometer depicted in figure 3.1 is controlled by a PDP-11 computer system. The user only has to transfer the sample from the preparation vessel to the analyzer chamber and define the measurement conditions like excitation source (either MgKα or AlKα), analyser pass energy and binding energy regions of interest. The PDP-11 system acquires the intensity distribution of the selected regions and stores the result on floppy disk. All spectra were acquired using AlKα radiation and the analyser pass energy was set to 50 eV unless stated otherwise.

The spectra could be modified after acquisition. All spectra were corrected for X-ray satellites and mildly smoothed to improve the S/N ratio. Smoothing was done via an n-point (n=3.....15) Savitzky-Golay /60/ method. The spectrometric workfunction was regularly calibrated by use of the Ag3d5/2 binding energy set to 368.0 eV.

## 5.2: Sample manipulation

The sample consisted of pure (99.99 %) silver shaped into a form suitable for XPS analysis, see figure 5.1. The shaded area indicated in figure 5.1 is analysed in XPS; the X-radiation source illuminates an area of approximately 0.3 $cm^2$. The shaded area was polished with diamond paste with grains of 0.3 μm to obtain a mirror finish. The sample was then mounted on the sample rod and inserted into the vacuum system. The sample's position was optimized for maximal Ag3d signal strength in XPS. The signal strength appeared to be a strong function of the axial distance to the electron analyser. To avoid a large scatter in measured intensities, the precise axial position of the sample rod in the optimal position was marked which allowed the signal to be reproduced to within ca. 3-5%.

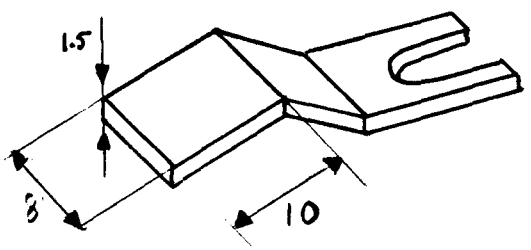


Figure 5.1: The silver sample used in the experiments. The shaded area polished and analyzed in XPS (dim. in mm.).

The position of the sample perpendicular to the sample rod axis was secured by a ring placed in the analyzer chamber into which the sample rod exactly fitted. Care had to be taken not to displace this ring by the thermally expanded top end of the sample rod. Usually, the sample was

cooled to room temperature before transferring the sample into the analyzer.

The first XPS scan showed large amounts of accumulated carbon and oxygen on the silver surface. These could be removed by bombarding the sample with argon ions (2 keV kinetic energy, current density 10 $\mu A/cm^2$). After sputtering the sample's surface was allowed to anneal at elevated temperature (725 K) for 10 minutes. At this temperature the silver surface atoms acquire enough mobility to smooth sputtering induced roughing of the surface. After several sputtering-annealing cycles, no impurities could be detected anymore in XPS.

In order to be able to heat the sample, a coil which could be energized from outside the vacuum system was placed in the direct vicinity (5 mm) of the sample in the sample rod. The sample and, unfortunately, the top end of the sample rod could thus be elevated in temperature above 875 K by indirect resistive heating. Temperature was measured with a chromel-alumel thermocouple with the reference side at room temperature, connected to a temperature control unit. The latter mantained the temperature constant within 2 K. The real temperature of the sample will be slightly lower than the value indicated by the thermocouple because of heat losses. However, because of the small distance thermocouple-sample and the good heat conductivity of silver, the sample's temperature will not differ much from the thermocouple reading.

To accelerate the cooling of the sample after turning off the heating current, cold air was blown through the top end of the sample rod. Heating and cooling rates depended on the sample temperature but were estimated at 1-2°/s and 0.2-1 K/s respectively in the range R.T.-775 K. The rather slow heating rate excludes TDS performance with the fitted mass spectrometer. Furthermore the aplicability for this technique was hampered by the heating configuration in which also the top end of the sample rod is heated, thus giving rise to the desorption of impurities.

### 5.3: The vacuum system

Both the preparation chamber and analyzer chamber are seperately pumped by oil diffusion pumps equiped with additional baffles cooled with liquid nitrogen. Cooled baffles are necessary to obtain the lowest possible pressures; the baffles prevent backdiffusion of water and oil cracking products from the oil diffusion pump into the UHV-part of the spectrometer.

Pressures were measured by ionization gauges placed near the oil diffusion pumps which are capable of measuring pressures down to their X-ray limit, approximately 8 $10^{-11}$ Torr. The lowest achievable pressures were 8 $10^{-10}$ Torr (preparation chamber) and 8 $10^{-11}$ Torr (analyzer vessel) and could be obtained only after baking the system for 48 hours at 475 K. The system was baked every weekend. All filaments present in the vacuum system (X-ray source, mass spectrometer, ionization gauges) were thoroughly outgassed after each bake-out. These precautions had to be taken in order to keep the vacuum system as clean as possible. As will be pointed out later, cleanliness of the vacuum system is of the utmost importance in adsorption experiments involving adsorbents with low sticking probability (like oxygen on silver).

The residual gass in the vacuum system consisted mainly of CO and CO2 and little H2O if any. The partial pressures of these gasses are in such a region (<$10^{-10}$ Torr) that adsorption rates become neglegible.

## 5.4: Oxygen admittance and Cs deposition.

All adsorption experiments with the silver sample were performed in the preparation chamber of the spectrometer which was isolated by a valve from the analyzer compartiment.

Oxygen gas (99.995 %) was admitted to the sample by means of a leak valve connected to a manifold filled with 1 Torr O2. The preparation chamber remained pumped by the oil diffusion pump if the oxygen pressure did not exceeded $10^{-5}$ Torr, at higher pressures the pump was closed and the preparation chamber remained unpumped during oxygen exposure.

Caesium was deposited by means of an SAES getter source placed approximately 25 cm from the sample. The getter source consisted of a metal box which contained pure caesium. Upon resistive heating of the whole container to 875-975 K, Cs diffused over a wire, placed into a slit in the box to the UHV side of the spectrometer, see figure 5.2.

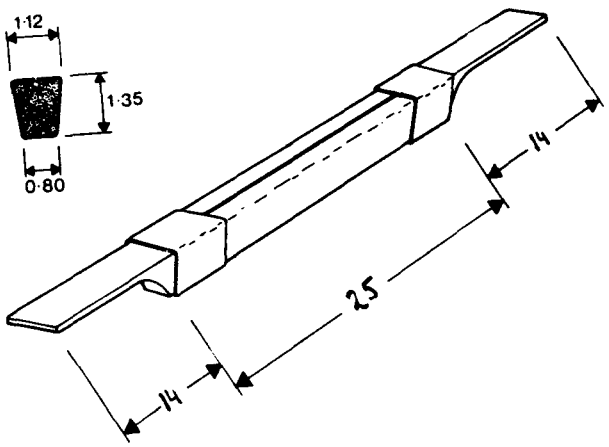


Figure 5.2: The caesium getter source. Dimensions in mm.

In order to obtain reproducible results, every Cs exposure was performed in the following way. First the getter source was outgassed for 10 minutes at 775 K while the sample was in the measuring cell, out of line of sight of the getter source. After outgassing the temperature of the getter source was raised to the desired value, usually 925 K, by raising the heating current. The temperature of the source was allowed to adjust for one minute. During this period the sample was transferred into the preparation chamber with its polished face turned away from the getter source. At the start of the exposure, the polished face of the sample was turned quickly towards the getter source and at the end of the exposure was again quickly turned away from it.

During Cs deposition pressure in the preparation chamber increased to $10^{-8}$ Torr. The mass spectrum showed H2, CO and CO2 desorption from the hot container. Cleanest caesium depositions (that is formation of pure Cs adlayers on silver without considerable amounts of oxygen) were made after the getter source got sufficiently aged.

Oxygen exposures in this chapter will be given in the unit Langmuir (L), 1 L = $10^{-6}$ Torrsec. For practical reasons, exposure times were kept in the 100-1000 second region. Coverages are calculated with help of the expressions derived in chapter 3. XPS binding energies quoted are with reference to the Ag3d5/2 peak at 368.0 eV, FWHM 1.7 eV.

## 6.1: Oxygen adsorption on clean polycrystalline silver.

First we have examined the interaction of oxygen with the pure polycrystalline silver sample at room temperature. At this temperature, oxygen is known to adsorb dissociatively on a silver surface, see chapter 4. The dissociative sticking probability of oxygen on a well annealed polycrystalline silver surface may be compared with that of an Ag(111) surface (ca. $10^{-6}$) since this surface is thermodynamically the most favoured one.

Adsorbed oxygen could be detected after exposures exceeding ca. $10^3$ L by the development of a symmetric O1s peak at ca. 530.0 eV, FWHM 1.9 eV. With increasing exposure, the peak became more intense but did not shift notably in BE, see figure 6.1. Together with the development of this O1s peak, a C1s peak developed at 287.5 eV. Peak area measurements revealed that the stoichiometry of the O1s(530.0 eV) to C1s(287.5 eV) species was ca. 3 to 1. Thus, it became clear that a surface carbonate (CO3) species had developed instead of a pure oxygen adlayer. The carbonate adlayer is the result of the reaction:

$$(6.1) \qquad CO_2 + \langle O \rangle_{ad} \longrightarrow \langle CO_3 \rangle_{ad}$$

The symmetric peak shape and the width of the O1s peak make it very unlikely that other oxygen species than the carbonate had developed.

The development of surface carbonate species is also mentioned in literature /37,62,63/. O1s and C1s binding energies are consistent with the results reported here. In figure 6.2 an estimation is given of the carbonate coverage as a function of the oxygen exposure. The measured values scatter considerably. This may be due to the varying amount of CO in subsequent exposures, which gives rise to the competitive CO "cleaning-off" reaction. The maximum oxygen coverage obtained was ca. 0.29.

Despite the fact that the admitted oxygen was very pure (99.995%) and the partial pressure of CO2 gas before oxygen exposure was ca. $10^{-10}$ Torr (at which pressure adsorption rates become negligible) it is well known that oxygen admittance can enhance the partial pressure of gasses like CO and CO2 by several orders of magnitude. We observed an enhancement of a factor of $10^2$ of the partial CO and CO2 pressures during admittance of $10^{-5}$ Torr of oxygen into the preparation chamber. Note that a partial CO2 pressure of $10^{-8}$ Torr is enough to transform all generated atomic oxygen at a $10^{-5}$ Torr oxygen pressure to carbonate because of the low dissociative sticking probability of oxygen on silver.

Unrecognised CO and CO2 side reactions, the low dissociative sticking probability of oxygen together with the low sensitivity of XPS for carbon (due to the low photo-ionization crossection of the C1s electron) may be the cause for the inconsistency in the assignment of O1s peaks observed in literature. Several groups (e.g. Campbell et al., /2/) use needle dosers to direct a stream of oxygen on the sample in order to keep the partial CO and CO2 background pressure as small as possible.

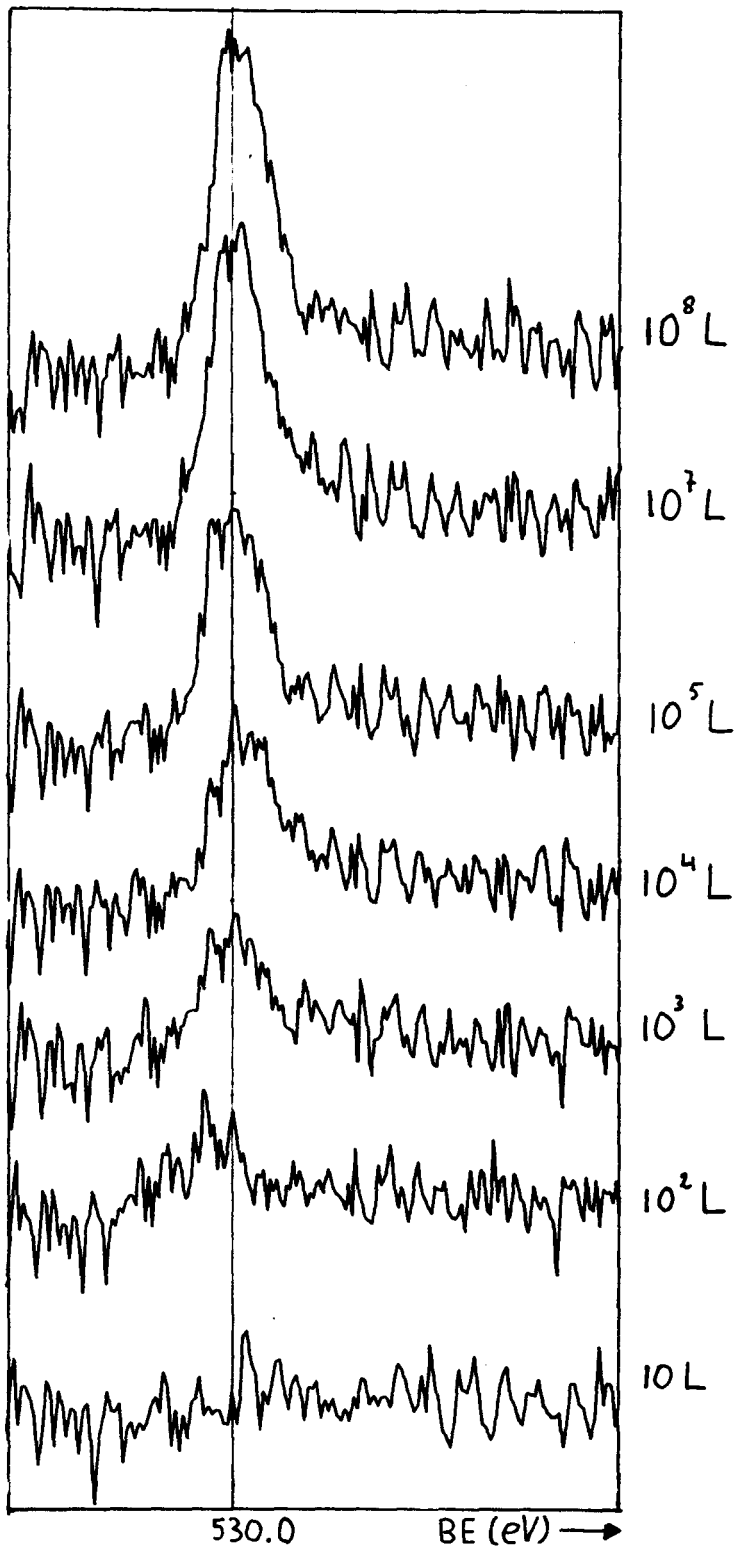


Figure 6.1: Development of the O1s peak as a function of the oxygen exposure, indicated on the right.

From literature /37/ it is known that surface carbonate species on silver decompose above 440 K. Thus the temperature of the silver sample was raised until 440 K and the adsorption experiment was repeated. The development of the O1s peak as a function of the oxygen exposure is given in figure 6.3. Again a peak centered at ca. 530.0 eV was observed. The O1s intensity remains small, the intensity at a $10^8$ L dose is ca. a factor 3

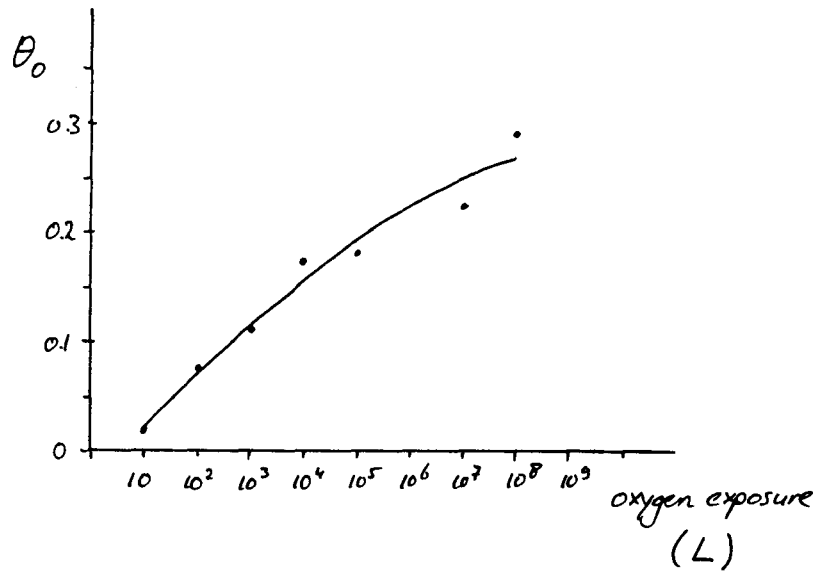


Figure 6.2: Estimated oxygen coverage as a function of the oxygen exposure at room temperature.

lower than after a corresponding dose at room temperature. After the $10^4$ L dose there is some evidence for a peak at lower binding energy. At the $10^8$ L dose the O1s peak seems a little bit shifted towards higher binding energies. An accurate determination of peak intensity as well as peak BE position was hampered by the bad S/N ratio.

Notwithstanding the fact that the stoichiometry of CO3 as well as the low photo-ionization cross-section of carbon made it difficult to estimate the C1s signal strength, we attribute the O1s signal to the formation of surface carbonate again.

Clearly, the system as such was not suited to study atomic oxygen adsorption on polycrystalline silver. Because CO and CO2 do not react with a clean silver surface but do react with an oxygen predosed silver surface /62/, obviously the species was formed during oxygen exposure but reacted with residual CO (clean-off reaction) and CO2 (carbonate formation).

In fact the reaction with CO2 opens the possibility to a fairly accurate measurement of the initial dissociative sticking probability of oxygen on silver by exposing the silver to a mixture of CO2 and O2 such that all atomic oxygen formed is conserved in CO3 and is not liable to CO oxidation anymore. Because of the stoichiometry of CO3 the O1s S/N ratio will be improved. We did not mix the oxygen with extra CO2 so we can only give a lower estimate of the initial sticking probability. From figure 6.2 a value of ca. $2\ 10^{-3}$ can be derived. This value is inbetween values reported for Ag(111) and Ag(110).

Heating the sample above the decomposition temperature of the carbonate species reduced its formation but did not yield atomic oxygen. This is due to the competitive CO cleaning-off reaction. Some carbonate remained on the surface because of the surface temperature (440 K) which may not be high enough to completely surpress its stationary coverage. The decomposition temperature of the surface carbonate on Ag(110) was taken from /37/. Others /62/ report 485 K whereas on Ag(111) 460 K was observed /2/. Fur-

thermore, our temperature measurement yields a slightly exaggerated value as mentioned above.

Because of the large exposures involved, we used high oxygen pressures (up to 1 Torr). Subsequent evacuation of the preparation chamber did not immediately result in the original UHV. Residual gasses were mainly H2O, CO2 and CO with a total pressure of ca. $10^{-8}$ Torr. Therefore, carbonate formation may be formed during cooling the sample by reaction with the residual CO2 (the neccessity for cooling was explained in chapter 5).

In an attempt to adsorb atomic oxygen, the admitted gas phase oxygen was atomized during exposure by a hot filament in line of sight of the sample. Such attempts have been made earlier /47/. The exact mechanism remains obscure but clearly the gas phase oxygen is excited by the hot filament, and dissociated. These activated species are more reactive towards the silver surface. This can be visualized by figure 2.1 where the dashed line represents the potential curve for two oxygen atoms approaching the surface: no activation barrier is encountered and thus facile chemisorption can take place.

As an "atomizer" we used the hot filament of our mass spectrometer. This filament was situated ca. 2 cm from the sample surface. Oxygen pressures during these kinds of exposures had to be kept below $10^{-5}$ Torr to prevent a filament burn-out.

Figure 6.4a gives the result of a $10^3$ L exposure at 475 K conducted in this way. A distinct peak around 528.4 eV is seen, indicative of atomic oxygen /2,47/. This attribution was substantiated by the reactivity of this oxygen species towards CO /47/: a 30 L dose completely removed the peak at 528.4 eV, see figure 6.4b-d. The oxygen coverage obtained, assuming an on top species is ca. 0.29.

Together with the atomic oxygen peak, a peak at somewhat higher binding energy developed, more clearly seen after all atomic oxygen is removed (figure 6.4d). Assignment to the surface carbonate species was excluded after a thourough investigation of the C1s region which showed no peak intensity at 287.5 eV (the O1s peak intensity can be used to predict the expected C1s intensity. This prediction can be used to adjust the XPS scan time in the C1s region so that such a peak could be seen). Another argument against the assignment to a carbonate species is its BE ( 530.6 eV ) and its FWHM of 3.0 eV. The atomic oxygen is characterized by a BE of 528.4 eV and a FWHM of 2.0 eV, see figure 6.4e.

By carefully performed activated oxygen exposures (the sample rod had been outgassed during the preceding night and depletion of preparation chamber impurities by excessive oxygen dosing before the activated oxygen exposure had occurred) we could exclude carbonate formation at lower temperatures. Exposures at 425 and 375 K yielded the same overal results as at 475 K. The O1s atomic oxygen peak shifted less than 0.2 eV at 425 K but at 375 K a notable peak shift of 0.4 eV to 528.8 eV could be observed. The O1s peak at higher binding energy remained at 530.6 eV. We have no explanation for the O1s BE shift at lower temperatures.

If an oxygen exposure with atomizer was conducted at room temperature, carbonate formation could not be prevented, as evident from the appearance of a C1s peak at 287.5 eV. The O1s region showed a broad peak centered at 530.0 eV with a FWHM of 3.5 eV. This indicates formation of more than one oxygen species. This was substantiated by the CO reactivity of the O1s multiplet: after a 100 L CO dose, the region around 529.4 eV was totally depleted, leaving a peak at 530.5 eV. Because of its reactivity to CO we assign the species at 529.4 eV to atomic oxygen, albeit that its BE is not consistent with the one derived above for this species. Note that we also found a shift toward higher BE of atomic oxygen adsorbed at 375 K. The remaining peak at 530.5 eV is assigned to the well known surface carbonate

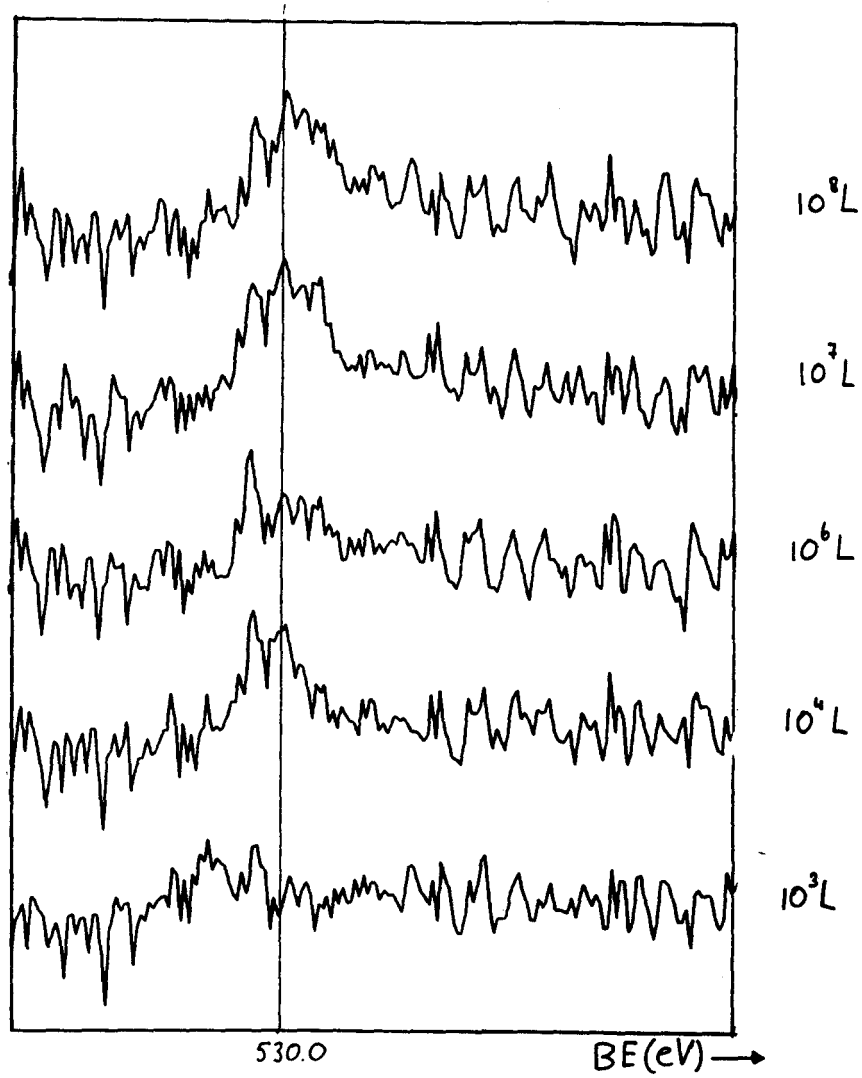


Figure 6.3: Development of the O1s signal as a function of the oxygen exposure at 440 K.

form, with again an inconsistency in O1s BE compared to 530.0 eV derived above.

After removal of the carbonate species by flashing to 500 K, the atomic oxygen peak reappeared at 528.6 eV, consistent with the value of 528.4 eV derived above. With it a peak at 530.6 eV remained which could not be identified as carbonate oxygen. This peak may be responsible for the apparent shift of the carbonate O1s peak to higher binding energies.

Approximately the same results were obtained after sputtering the doublet structure of figure 6.5a with Ar-ions (2 keV, 10 sec, 10 $\mu A/mc^2$). Note that this dose comprises ca. 6 $10^{14}$ ions/$cm^2$ which is approximately the number of surface atoms per $cm^2$. This dose completely removed the carbonate species. The CO sensitive atomic oxygen peak shifted to a value of ca. 528.7 eV, whereas again a peak at 530.6 eV remained. Of course sputtering in this way is hardly quantitative, however, the indicated trend is noteworthy.

Clearly, atomic oxygen can be formed by activating the gas phase oxygen. The formed oxygen adlayer at moderate exposures is the result of a vast increase of the sticking probability of the activated gas phase oxygen for the silver surface. This enhanced sticking probability relaxes the constraint of a very low CO background pressure.

Similar results as described above were obtained by Felter et al. /47/ on Ag(111) by activating the gas phase oxygen with a hot (1500 K) platinum filament. The atomic oxygen found, active in the oxidation of CO, was

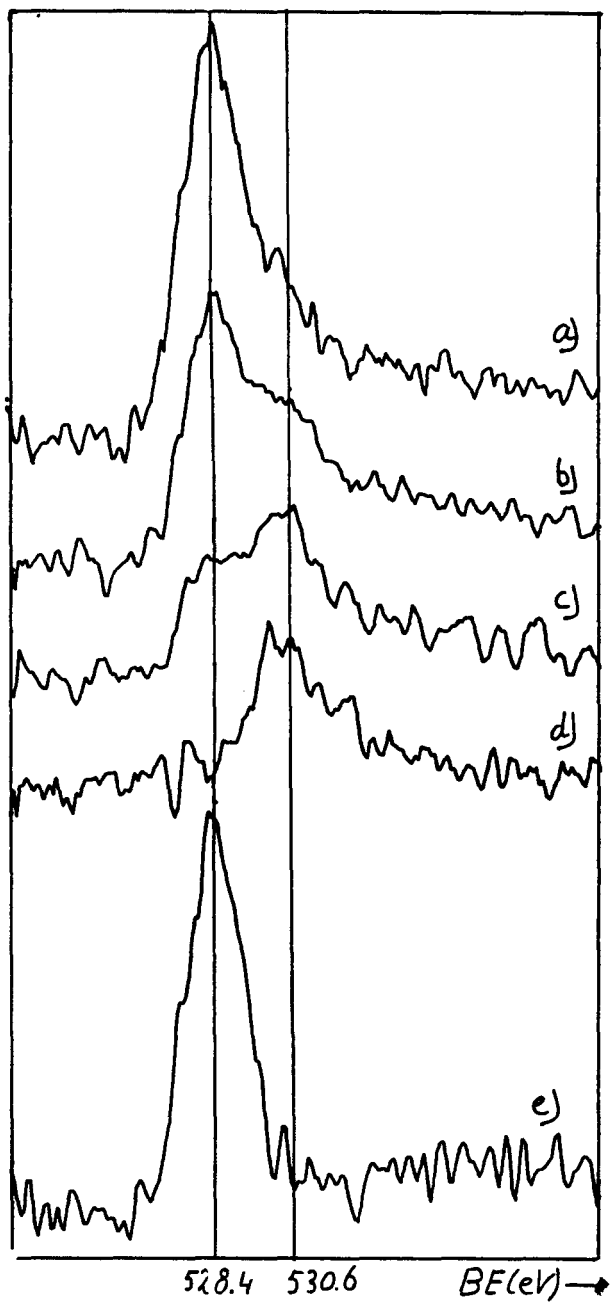


Figure 6.4: a) 1000 L oxygen exposure at 475 K with atomizer.
b) till d) + 10 L CO
e) a-d.

characterized by an O1s BE of 528.5 eV, consistent with our results. Our assignment is further corroborated by other reported O1s binding energies for atomic oxygen /37,2,51/.

It is therefore startling to find also an atomic oxygen species at 529.4 eV. Our indentification was based on the reactivity of this species with CO. Furthermore we showed that it can be transferred into the "normal" atomic oxygen at 528.4 eV by heating (or sputtering). It must be noticed that the atomic oxygen species at 529.4 eV always was accompanied by a carbonate O1s signal at 530.5 eV.

Also in literature binding energies assignments to atomic oxygen remain a matter of dispute: BE of 529.8 eV /38, 529.6 eV /53/ and 528.2 eV /2/ are reported. We seem to have detected both sorts but cannot give an adequate explanation for the variation.

The next attempt was to produce subsurface oxygen. Therefore, the sample was heated till 475 K at which temperature, according to BACKX et al. /36/, subsurface oxygen must be formed on Ag(110) The heated sample was exposed to 5 Torr of oxygen for 20 minutes. A simular exposure led JOYNER et al. /51/ to the indentification of subsurface oxygen on silver foil. The resulting O1s peak is depicted in figure 6.6a. Again a C1s peak at 287.5 eV had developed. Subsequently, the sample was held at 625 K for 10 minutes and again analysed, see figure 6.6b. An oxygen peak centered around 530.8 eV remained with a FWHM of 3.0 eV. No intensity could be discerned anymore in the C1s region. The same oxygen exposure at room temperature did not leave any O1s signal after heating to 625 K. If after oxygen exposure at 475 K the sample was heated to 725 K, no O1s signal could be detected either.

The only reported oxygen species stable up to 625 K is subsurface oxygen. So the O1s peak at 530.8 eV observed here may actually arise from a subsurface oxygen form, which desorbs between 625 K and 725 K. The assignment to subsurface oxygen is further substantiated by the high temperature required for its formation. Furthermore the binding energy of the species agrees reasonably well with the value of 530.3 eV reported by JOYNER /51/. The value of 528.5 found by CAMPBELL /37/ however is in conflict with our observation.

Because of its binding energy position, peak width and also because of its insensitivity to CO and relative resistance towards sputtering, it is likely that the reported species at 530.6 eV during activated oxygen exposures is also subsurface oxygen. The assignment is corroborated by the fact that the species cannot be entirely removed by heating the sample to 625 K. Even after heating to 725 K a minor fraction remained. The binding energy of the species shifted 0.2 eV to higher values after heating.

Felter et al. /47/ found an oxygen species with an O1s binding energy energy of ca. 530.0 eV after activated oxygen exposures. This oxygen species was not reactive towards CO and could not be resolved with UPS, suggesting a dissolved oxygen species since UPS is more surface sensitive than XPS.

To corroborate our assignment we checked for other subsurface characteristics. Backx et al. /36/ showed that subsurface oxygen exchanges with atomic oxygen. Backx et al /50/ and Campbell /2/ showed that subsurface oxygen can be transferred to the surface at elevated temperatures.

To check for the exchange ability of our species at 530.6 eV with atomic oxygen, the oxygen multiplets of figure 6.4a were unravelled into their constituents. If exchange takes place, we expect a depletion of the 530.6 eV signal upon reacting the atomic oxygen away with CO. In order to keep the number of variables as small as possible, the atomic oxygen peak was set at 528.4 eV, FWHM 2.0 eV and the subsurface peak at 530.5 eV, FWHM 3.0

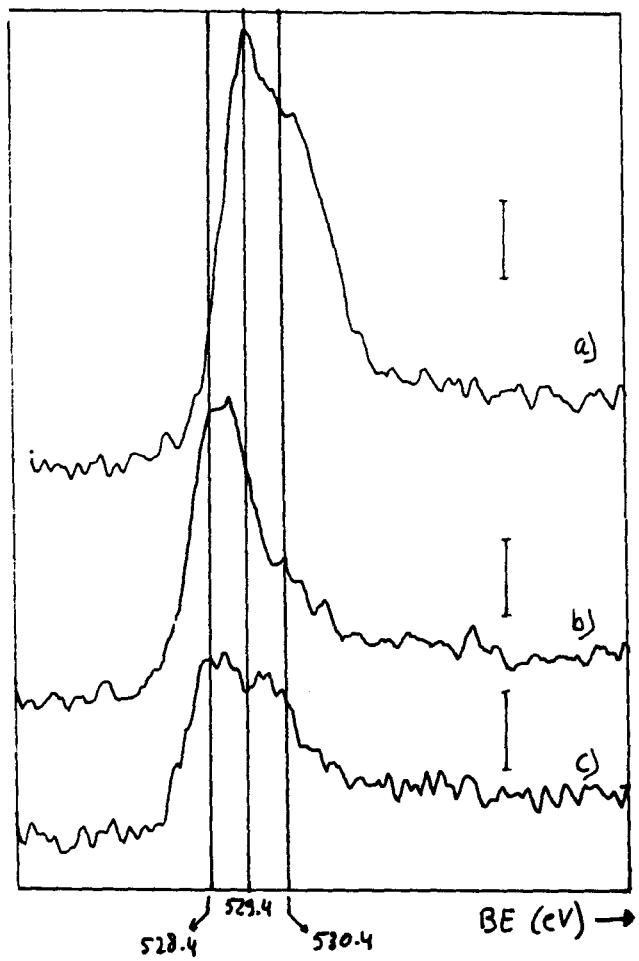


Figure 6.5: a) 1000 L oxygen exposure at room temperature conducted with atomizer
b) after sputtering
c) after 10 minutes at 500 K.

eV. Peak shapes were assumed to be Gaussian. Thus the only variables that remained were the heights of the two constituents. Figure 6.7 gives the result of this synthesis procedure. A small decrease (ca. 25%) of the peak intensity at 530.6 eV points to a partial transformation of this species to atomic oxygen.

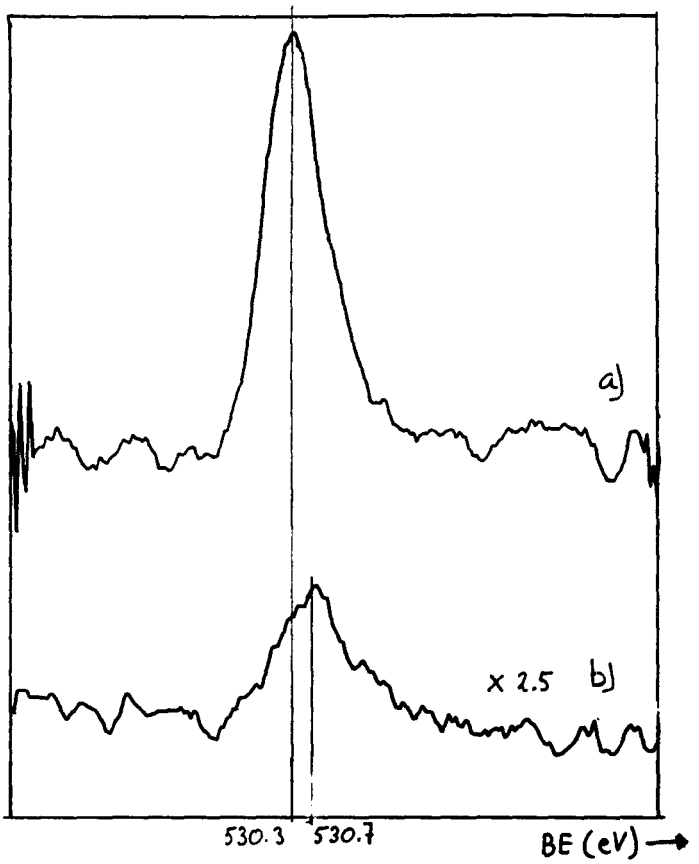


Figure 6.6: a) 5 Torr oxygen for 20 minutes at 475 K without atomizer
b) after 10 minutes at 625 K.

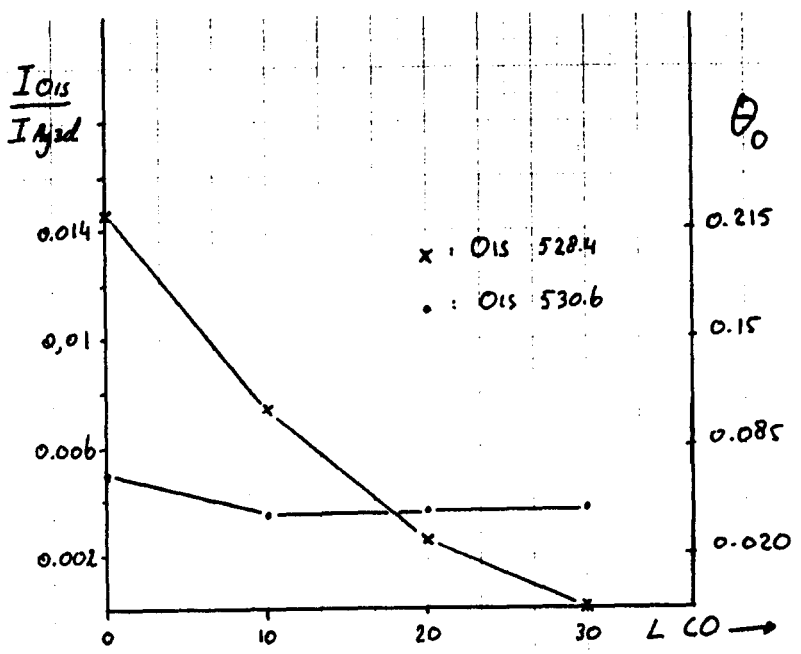


Figure 6.7: Result of curve synthesis of the multiplets depicted in figure 6.4a-d

The amount of the O1s(530.6 eV) species could not be greatly influenced by varying the sample temperature. CO reduction at 325 K and 525 K of a similar( $\theta$=0.34-0.38) oxygen adlayer generated by activated oxygen exposure at 425 K left only 10% more oxygen behind at 325 K.

As noticed in chapter 4, the nature of the subsurface oxygen is still obscure. On our polycrystalline sample we may safely assume a broad distribution of subsurface adsorption sites with a corresponding distribution in adsorption energies, substantiated by the rather broad (3.0 eV) peak associated with subsurface oxygen. The binding energy shift of the subsurface oxygen peak upon heating may then be the result of depletion of less tightly held subsurface species. In fact it may also explain the somewhat higher binding energy found in the non-activated oxygen exposure.

Also at low temperatures (375 K) subsurface oxygen was found after an activated oxygen exposure. BACKX et al. /36/ indicate that appreciable amounts of subsurface oxygen are formed only at temperatures exceeding 440 K. Our value of 375 K seems a little bit low. Note that BACKX et al. did not use activated oxygen exposures. The facile formation of subsurface oxygen with activated oxygen exposures may be due to the high virtual oxygen pressure at these kind of exposures.

We could not determine a lower temperature limit for subsurface formation due to the carbonate O1s signal which obscured the subsurface O1s peak: heating the sample to desorb the carbonate species would result in the occupation of subsurface sites at higher temperatures.

We did not find molecular oxygen adsorption on our polycrystalline sample in the temperature range studied. (R.T. to 725 K). This is consistent with the findings of others /2,36/. However, our apparatus was not very well suited for studying this particular species and we therefore did not search for the species systematically.

## 6.2: The caesium/oxygen co-adsorption system.

Caesium depositions as outlined in chapter 5 were always accompanied by oxygen uptake, evident from the development of a O1s peak in the range 530.2-532.0 eV. This precluded the study of pure Cs-adlayers. Various attempts are listed in table 6.1.

The origin of the oxygen is not clear. It could be that the Cs in the getter source was not pure e.g. because of slight oxidation during installation in the vacuum system. With the mass spectrometer we could not determine whether the yield of the getter source consisted of Cs or Cs-oxides; no signal could be discerned in the mass 133-165 region, probably due to the low sensitivity of the mass spectrometer at these high masses.

Oxygen uptake during alkali deposition was also reported in literature /53,63/, characterized in XPS by a broad O1s peak around 531.5 eV, consistent with our observation. The variation of the O1s BE in various attempts as listed in table 6.1 cannot be correlated to $\theta$Cs, surface temperature, oxygen-caesium stoichiometry or appearance of a C1s signal. Development of a CsOH species cannot be excluded despite the Cs3d3/2 BE of bulk CsOH (737.9 eV, /64/): the latter value may be considerably affected by a two dimensional geometry. We have no explanation for the large spread in O1s binding energies.

| adlayer stoichiometry | Cs3d3/2 BE (eV) | O1s BE (eV) | surface temp. (K) |
|---|---|---|---|
| Cs2.30; θCs=0.11 | 739.5 | 531.2 | 475 |
| CsO; θCs=0.13 | 739.5 | 532.0 | 475 |
| CsO; θCs=0.06 | 739.5 | 531.6 | 475 |
| CsO; θCs=0.10 | 739.3 | 530.3 | 475 |
| CsO1.5; θCs=0.04 | 739.5 | 531.5 | 295 |
| CsO3; θCs=0.03 | 739.7 | 530.2 | 475 |

Table 6.1: Various Cs deposition attempts.

In figure 6.8a the Cs3d signal of the purest Cs layer obtained is depicted. The broad feature around 718 eV is assigned to the Ag3s peak. The Cs3d3/2 BE is consistent with reported values in literature /53,63/.

The Cs-O adlayers were subsequently oxidized. The results are listed in tabel 6.2. The Cs3d doublet after $10^3$ L oxygen exposure to the Cs2.30 layer is shown in figure 6.8b. Figure 6.9 shows the development of the Cs3d3/2 binding energy and the Cs and oxygen coverage as a function of the oxygen exposure to this layer.

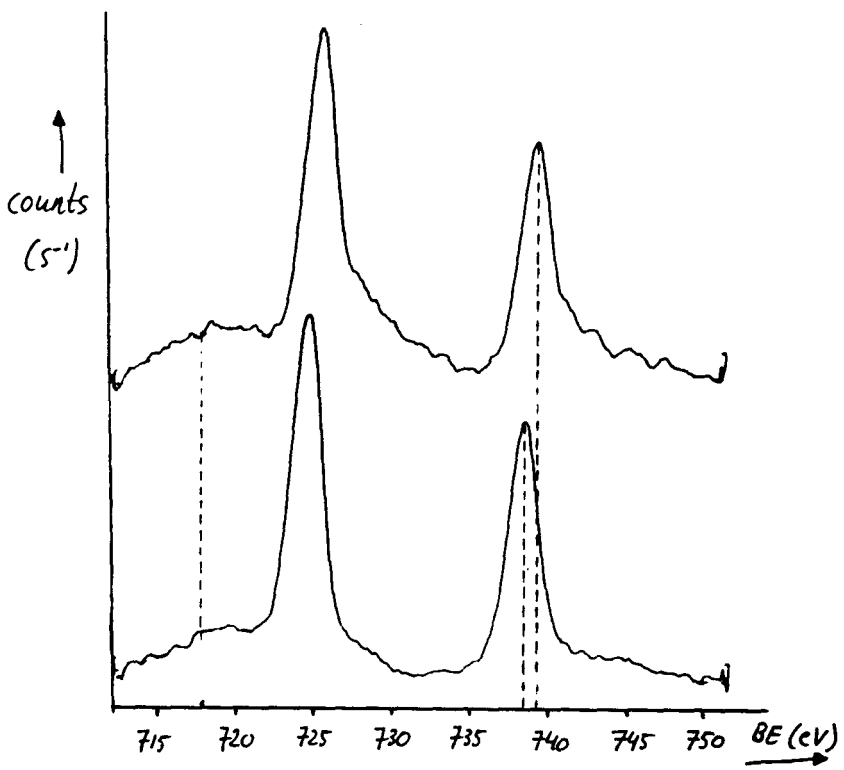


Figure 6.8: a) Cs3d doublet from a $Cs_2O$ layer at 475 K.
b) Cs3d doublet from a CsO layer at 475 K.

| adlayer stoichiometry | Cs3d3/d BE (eV) | O1s BE (eV) | oxygen exp. (L) activated: Y/N |
|---|---|---|---|
| CsO1.9; θCs=0.11 | 738.6 | 530.4 | 10; N |
| CsO2.0; θCs=0.11 | 738.6 | 530.4 | $10^2$ N |
| CsO2.2; θCs=0.12 | 738.4 | 530.3 | $10^3$ N |
| CsO3.5; θCs=0.16 | 738.2 | 531.0 + 528.7 | $10^3$ Y |
| CsO6; θCs=0.08 | 738.2 | 530.7 + 528.5 | $10^3$ Y |
| CsO1.8; θCs=0.11 | 738.2 | 530.0 + 528.2 | $10^2$ Y |
| CsO6; θCs=0.05 | 738.3 | 530.2 + 528.3 | $10^5$ N |
| CsO21; θCs=0.03 | 738.2 | 530.4 + 529.0 | $10^3$ Y |

Table 6.2: Results of oxidation of the Cs adlayers of table 6.1. The first three elements of the table refer to the first adlayer in table 6.1.

As can be seen in figure 6.9, but also in figure 6.8 by direct comparison with the Ag3s peak height, the Cs3d intensity increases upon oxidation. The increase varied in several atempts (10-30%) but was always seen after oxidizing freshly deposited Cs adlayers. The binding energy of the Cs3d3/2 peak decreases ca. 1.2 eV to ca. 738.2 eV after oxygen exposure. The major part of this decrease takes place during the first 10 L of oxygen exposure, see table 6.2.

The Cs3d peak shape changes remarkably upon oxidation: the high binding energy tail seen in figure 6.8a has vanished completely in figure 6.8b. This peak shape change was seen only at the Cs rich Cs2.30 layer; layers containing more oxygen gave rise to a symmetrical Cs3d peak even before oxidation.

**The Cs3d binding energy decrease.**

The decrease in core binding energy of adsorbed alkali metals upon oxidation has been reported before in literature /52,53,63,58/. Despite the large number of groups that observed this decrease, no firm explanation of its origin as yet has been given.

Starting from a simple picture of the chemical shift as derived in paragraph 3.3.2 one expects an increase in binding energy upon oxidation of the electropositive alkali metals. Another effect must be responsible for the observed decrease in Cs3d BE.

AYYOOB et al. /53/ ascribe the Cs3d BE decrease to the formation of a surface alloy between the silver and caesium enhanced by the oxygen induced decrease of radius of Cs. We propose the following alternative explanation.

For Na chemisorption on jellium, it has been calculated /4/ that with respect to a free Na atom, a large decrease (ca. 5 eV) in core level binding energy in chemisorbed Na was due to relaxation effects whereas a smaller (ca. 1 eV) increase was due to the chemical shift. This indicates that major BE shifts may occur due to relaxation effects. In the underly-

ing case, the observed decrease in Cs3d binding energy upon oxidation may be due to a more effective screening of a the Cs3d core hole by the excess negative charge of a nearby oxygen atom thus introducing a major relaxation effect which decreases the apparent Cs3d BE.

### The asymmetrical Cs3d peak shape.

Campbell /54/ also reported considerable AES peak shape changes upon oxidation of pure Cs adlayers, assigned to a change in chemical nature of the species. We would expect also a change in BE if the chemical nature of the species would change. In contradiction to this, we see rather symmetrical Cs3d peaks at the same BE as asymmetric ones.

The asymmetrical peak shape may also be due to enhanced shake-up and shake-off effects by a Cs induced state near the Fermi-edge of silver. The process may be compared with the asymmetrical broadening of the Pt4f peaks, see figure 3.5b. The enhanced density of states at the Fermi edge would be the result of electron donation of the Cs atom to the silver substrate. Upon oxidation the donated electrons would become localized in the oxygen-silver bond and thus reducing shake-up and shake-off processes.

To test this hypothesis, we scanned the Fermi region of the Cs-silver system with UPS. UPS should be able to find the populated part of the Cs induced density of states near the Fermi-edge, necessary for enhanced shake-up and shake-off processes.

The UPS spectrum of our clean silver (see figure 6.10a,b) resembles other reported UPS spectra /52/ albeit that the d-band emission in our case is stronger. This may be due to pronounced angular effects known to exist in UPS and will not be discussed here. The recorded UPS spectra after exposing the silver sample to Cs and oxygen are depicted in figure 6.10c,d. No evidence was found for a large Cs induced state near the Fermi-edge. How-

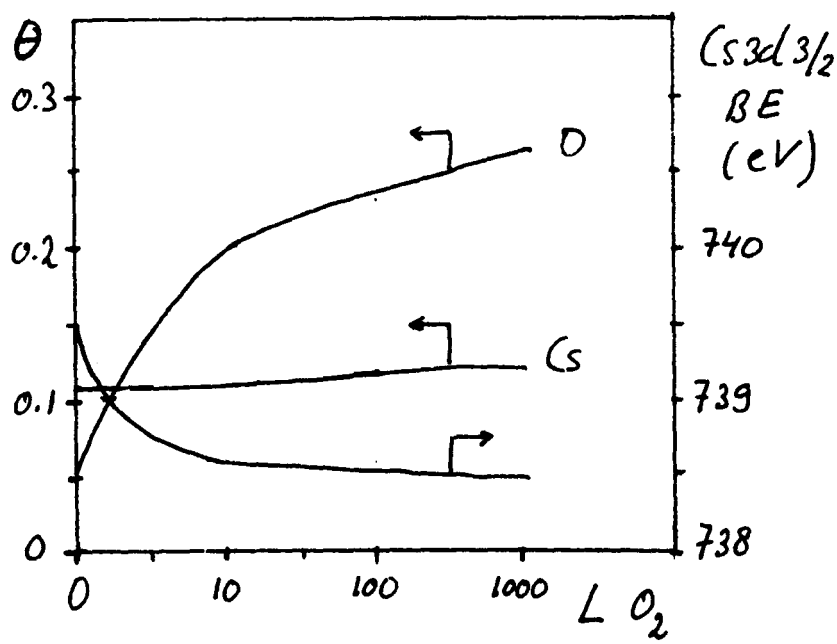


Figure 6.9: Cs and oxygen coverage and decrease in Cs3d3/2 binding energy as a function of the oxygen exposure.

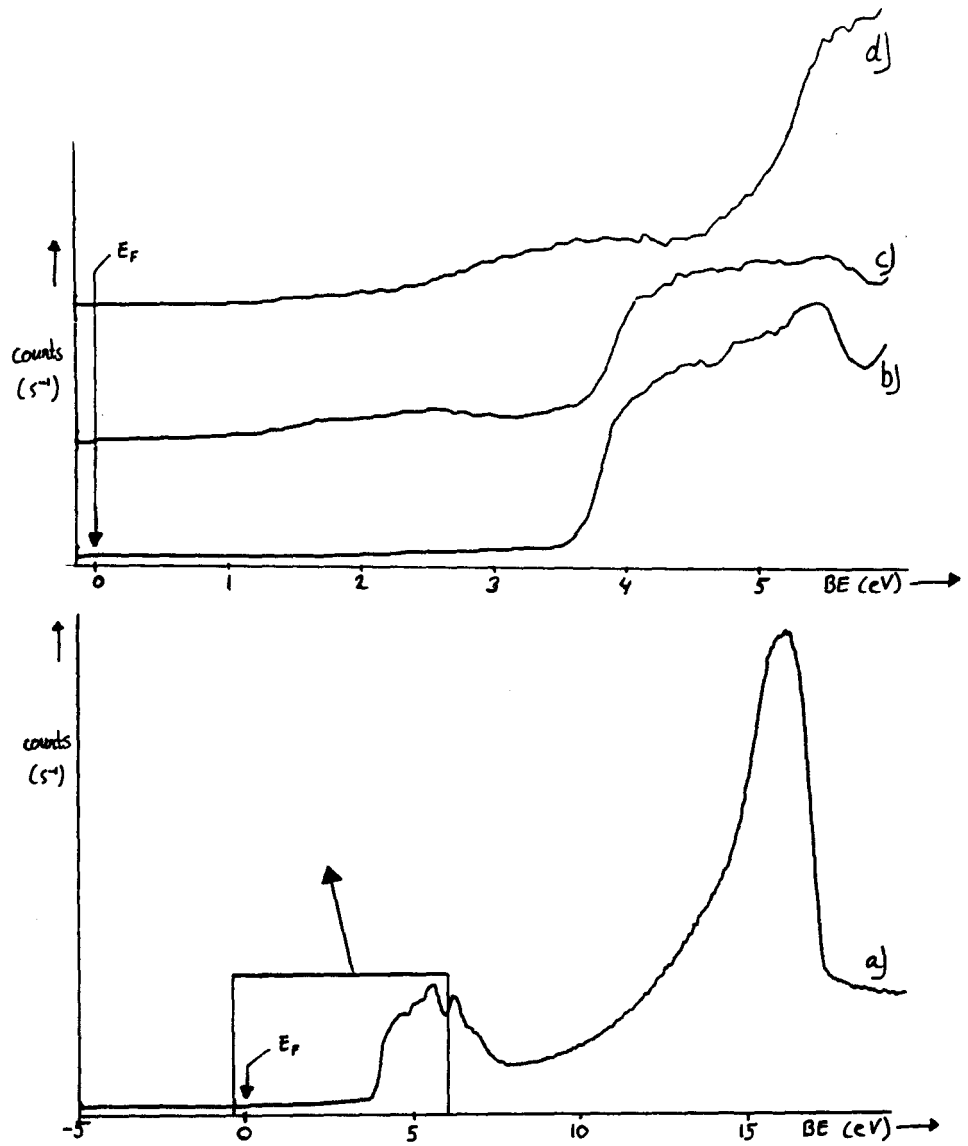


Figure 6.10: He-I UPS measurements of the Fermi region, the Fermi edge is indicated by Ef.
a),b) scan of the clean silver sample.
c) after Cs deposition.

d) after 500 L oxygen exposure.

ever, extrapolating the observed oxygen induced shift of density of states to higher BE values to a (nearly) oxygen free Cs layer would give a considerable density of states near the Fermi-edge.

The failure of finding the expected state may be due to several experimental intricacies. Firstly, it was not so easy to obtain a Cs rich adlayer again. Secondly, a Cs rich adlayer would be destroyed immediately during the UPS measurement. This became clear after several UPS measurement attempts on the VG ESCA-III. The plasma chamber of the UPS He lamp in this apparatus is pumped to UHV in two steps because of the high He pressure (0.1 Torr) involved (see figure 3.17). The rotary pump employed in the first differential pump step showed back diffusion, evident from the appearance of a mixed N2/O2 (air) signal on the mass spectrometer. The backdiffused oxygen always would and did lead to oxygen co-adsorption.

Therefore we do not discard entirely our hypothesis despite the failure of detecting the Cs induced state with UPS.

### The Cs3d intensity increase.

The increase of the Cs3d signal means that XPS "sees" more Cs after oxidation. This may be interpreted as either a spreading out of lumps of a Cs-O compound with dimensions in the order of the IMFP of the photo-electrons or the reappearance on the surface of dissolved Cs. Note that we do not have pure Cs adlayers in which case multilayer formation at low coverages would be hardly imaginable because of the ionic character of the Cs adlayer. Facile Cs uptake in the Ag bulk should be hampered by the large Cs radius, even when completely ionized (see tabel 3.3). Diffusion along grain boundaries at the surface would also not be a credible explanation for the sometimes large Cs3d intensity increase because of the rather large crystallites (20 μm) in the well annealed surface which limits the geometrical fraction of the surface consisting of grain bounderies to a negligible value /40/.

In figure 6.11 the Cs uptake curve at 375 K versus Cs deposition time is given. Multilayer formation in layer by layer fashion should lead to discontinuities in the Cs3d intensity acquired because of the expected change in sticking probability of Cs on Cs compared to Cs on Ag and the partial screening of photo-electrons stemming from subsequent Cs layers. The rather smooth development of the Cs coverage is not in favour of the layer by layer growth as e.g. proposed by GRANT et al. /55/.

An extended view of the Cs3d doublet at two different coverages is shown in figure 6.12. Clearly a high binding energy tail is present at both coverages, more pronounced at the higher coverage. Following Tougaard (see paragraph 3.4.4) we attribute the high BE tail to the position of Cs photo-emitters underneath a layer of dimensions comparable to the IMFP of the photo-electrons.

The smooth Cs uptake curve and the high BE tails of the Cs3d doublet indicate Cs-O particle formation on the silver surface. These lumps are thought to spread out over the surface upon oxygen adsorption leading to the Cs3d intensity increase.

Another argument in favour of the Cs lump formation may be derived from the variation of the absolute Ag3d signal with Cs exposure, see figure 6.13. Note that our previous optimization of the Ag3d signal magnitude as a function of the sample position allowed for reproducible acquisitions of intensities.

As a coarse model for the attenuation of the Ag3d signal we assume a flat Cs layer of thickness tk covering a fraction $\theta'$ of the surface. tk then can be estimated from the observed Ag3d intensity decrease. From equation 3.21 it follows:

$$I_{Ag3d}/I^{\circ}_{Ag3d} = 1 - \theta_{Cs}(1-\exp(-tk/\lambda_{Ag,Cs})) \qquad (6.2)$$

As a measure for the amount of Cs being present we take the dimensionless quantity $\theta' tk/\lambda$. If we plot $I_{Ag3d}/I^{\circ}_{Ag3d}$ as a function of this quantity for various $\theta'$, we obtain figure 6.14. In this figure we have also drawn lines of constant thickness $tk/\lambda$, $tk/\lambda \approx 0.1$ corresponding to one monoatomic layer of Cs. From figure 6.14 it is clear that the measured ratio:

$$I_{Ag3d}/I^{\circ}_{Ag3d} = 0.76 \qquad (6.3)$$

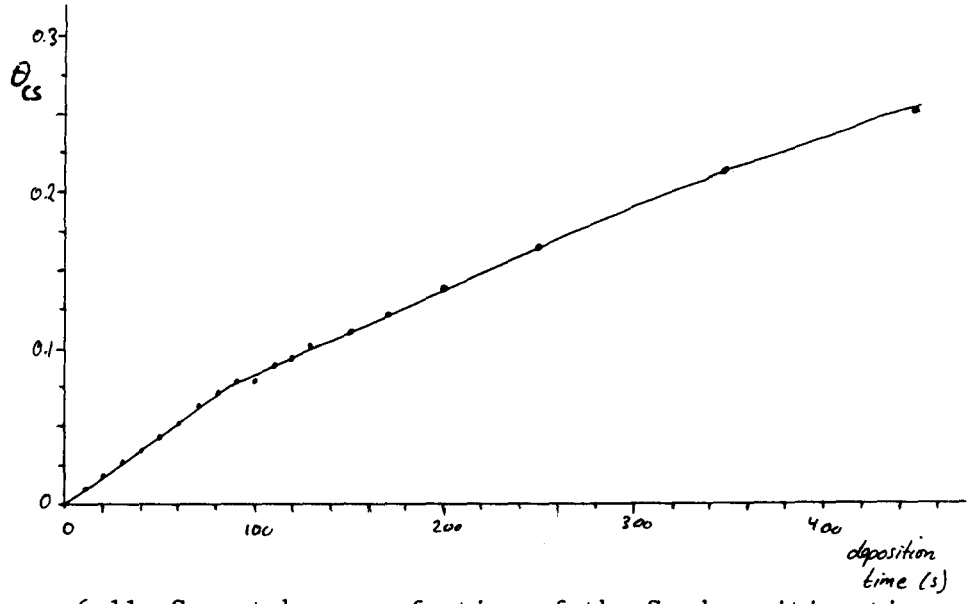


Figure 6.11: Cs uptake as a funtion of the Cs deposition time at 375 K. θCs has been calculated assuming monolayer formation.

cannot be explained by monolayer Cs coverage; it follows that we have to assume a layer thickness of at least ca. 3 Cs atoms (θ'=1) to explain the large attenuation of the Ag3d signal.

**Characterisation of the oxygen species on Cs predosed silver.**

The Cs3d3/2 BE was shown to be insensitive to the amount of co-adsorbed oxygen during Cs deposition. In various attempts this amount varied a factor of 6 relative to that of Cs while the Cs3d3/2 BE remained constant at 739.5 eV. The enormeous decrease in BE after as little as 10 L oxygen exposure is in contrast to this insensitivity moreover because of the fact that this exposure gave rise to a less oxygen containing adlayer compared to various Cs depositions for which no decrease was observed. We conclude from this that during the oxygen exposure of a Cs adlayer a different oxygen species is generated as compared to the one deposited together with Cs during evaporation.

From table 6.2 it becomes clear that O1s binding energies after oxygen exposure appear in two clusters, one around 528.6±0.4 eV and one around 530.6±0.4 eV. The oxygen species around 530.6 eV seems to be responsible for the BE decrease of the Cs3d peak since an O1s peak in this region appears already after the 10 L oxygen dose, simultaneously with the Cs3d BE decrease.

Heating a CsO3 (θCs=0.17) layer to 575, 625 and 675 K subsequently showed a depletion of Cs from the layer resulting in a stoichiometry of CsO2.6 (θCs=0.16), CsO2.8 (θCs=0.09) and CsO4 θCs=0.04) respectively. This shows a fairly simultaneous desorption of Cs and oxygen(O1s≈530.6) as found by CAMPBELL /54/ as well.

We observe various Cs to oxygen stoichiometries but clearly they are all more oxygen rich then the oxygen saturated compound Cs4.40 reported by GRANT et al. /55/. Our stoichiometry is more in agreement with the findings of CAMPBELL /54/ and AYYOOB et al. /53/ who found a Cs to oxygen ratio of 1:3.

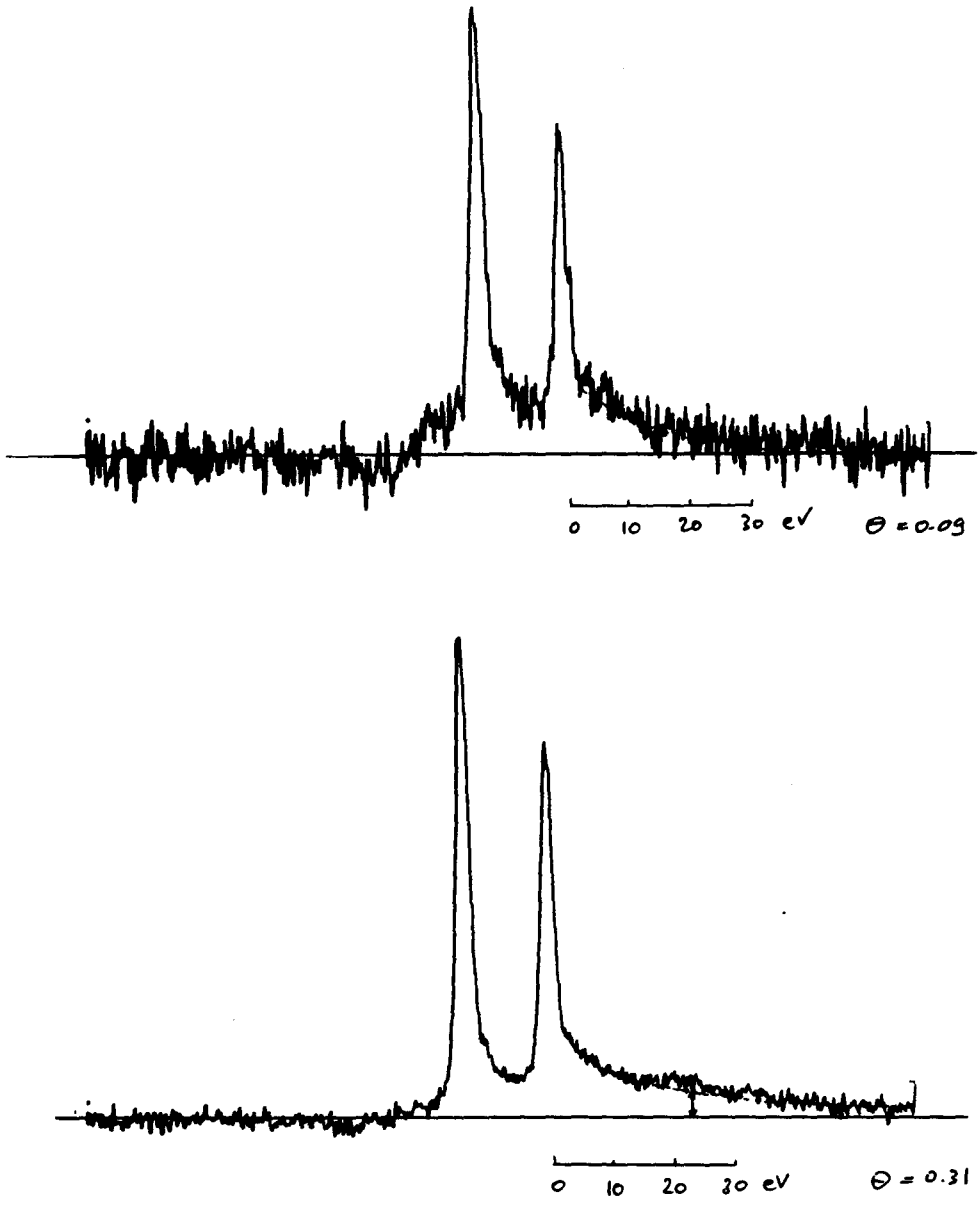


Figure 6.12: a) Cs3d doublet at t= 70 s
b) Cs3d doublet at t= 325 s, scaled to the same height as a).
The Cs3d doublets have been corrected for X-ray satellites and the Ag3s peak has been substracted.

The species around 528.6 eV could be reacted away with CO. This feature together with its BE points towards an identification as atomic oxygen bound in a similar way as to a clean silver substrate. Atomic oxygen was found at Cs:O stoichiometries exceeding 1:3, even at high Cs loadings (θCs=0.16). Following GRANT et al. /55/ this means that even at these high Cs loadings, bare Ag sites must be available for atomic oxygen adsorption. This is corroborated by its simular BE and behaviour towards CO compared to the species adsorbed on the clean silver surface.

Our results are similar to those obtained by GARFUNKEL et al. /52/ for the case of oxidation of sodium adlayers on Ag(100). They also found an immediate decrease of the alkali core level BE together with an increase in

workfunction. The O1s BE of the oxygen species immediately after oxygen adsorption was ca. 529.8 eV, which compares fairly well with our value of 530.6±0.4 eV. Following Garfunkel et al. we attribute the latter O1s peak to a Cs associated oxygen species.

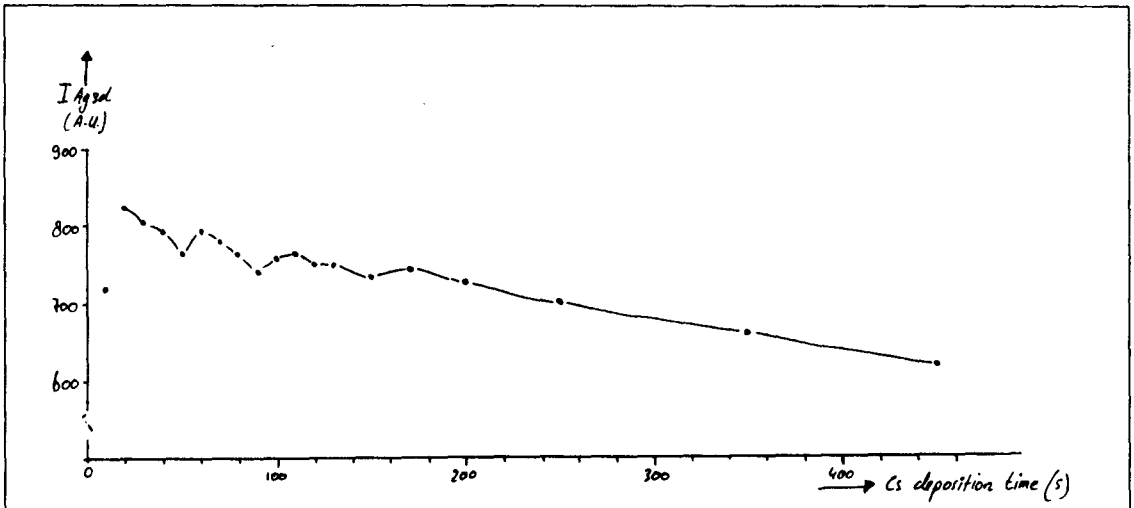


Figure 6.13: Variation of the Ag3d signal strength as a function of the Cs deposition time.

For the Cs/oxygen interaction on the silver surface we propose the following: During deposition, Cs forms lumps with some form of "disolved" oxygen. Lump formation is substantiated by the large attenuation of the Ag3d substrate signal, a smooth Cs uptake against Cs deposition time curve and a high BE tail at the Cs3d doublet. Exposing these lumps to oxygen leads to a major reorganisation of the adlayer, evident from a Cs3d intensity increase and a Cs3d BE decrease. The Cs3d intensity increase is explained by assuming spreading of the original Cs-O lumps by adsorption of gas phase oxygen. The Cs3d BE decrease is the result of enhanced relaxation of the core hole. This effect could exceed the chemical shift of the Cs3d electrons which shows the opposite trend. Activated oxygen exposures lead to an atomic oxygen species comparable to that on clean silver (CO sensi-

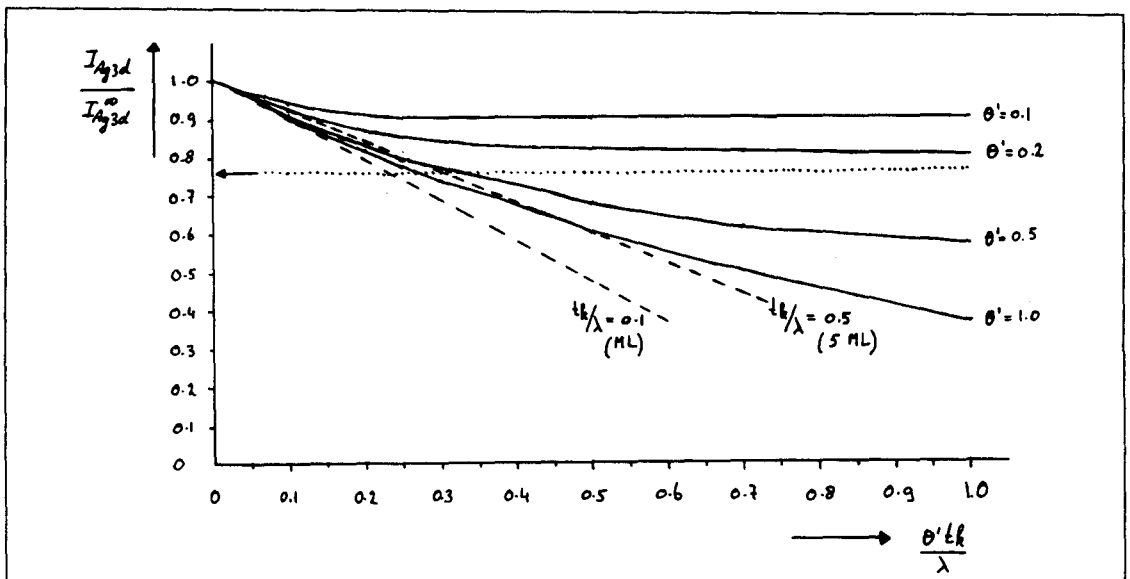


Figure 6.14: Attenuation of the IAg3d signal as a function of the amount deposited Cs and its configuration on the silver surface, see text.

tive, O1s BE), even at high Cs coverages. Thus atomic oxygen is bound to the Cs dosed silver substrate in a similar way as to a clean silver surface.

From XPS alone it is hard to determine the nature of the co-adsorbed oxygen species on a Cs dosed silver surface. The complexity of this adlayer underlines the fact that supplementary techniques will be needed in order to provide a better characterization of this co-adsorption system.

On a clean polycrystalline silver surface we indentified three adsorbed oxygen species:

- A surface carbonate form, characterized in XPS by an O1s peak at 530.0 eV and a C1s peak at 287.5 eV.
- Atomic oxygen, characterized by an O1s binding energy of 528.4 eV and its reactivity towards CO.
- Subsurface oxygen, characterized by an O1s binding energy of 530.6 eV.

It is shown that the competitive CO oxidation reaction and the facile formation of the carbonate species precluded the indentification of atomic oxygen in non-activated oxygen exposures because of the low dissociative sticking probability of oxygen; we measured a value of 10-&3. which is thought to be a lower limit.

Subsurface oxygen was indentified by its high desorption temperature (between 625 and 725 K) and the elevated temperature necessary for its formation (375 K).

Cs deposition, accompanied by unwanted oxygen uptake, occurred in the form of small particles. This model is substantiated by the large attenuation of the substrate Ag3d sigal and the high BE tail of the Cs3d doublet. The Cs-O lumps formed appear to at least partially spread out over the surface upon oxygen exposure. This results in a Cs3d intensity increase of 10-30%. The Cs3d BE decrease (ca. 1.2 eV) following oxygen exposure is probably the result of an enhanced relaxation of the in core hole created in photo-emission

Oxygen co-adsorbed with the Cs is difficult to characterize by XPS alone. We observed two clusters of O1s binding energies around 528.6±0.4 eV and 530.6±0.4eV. We attribute the former to an oxygen species in the direct vicinity of Cs atoms because of its coincident appearance with the Cs3d BE decrease. The latter is assigned to atomic oxygen. Because of its BE and reactivity towards CO it must be bound to the silver substrate in a similar way as to the clean silver surface.

Literature.

/1/: The mechanism of the selective oxidation of ethylene to ethylene oxide.
P.A. Kilty, W.M.H. Sachtler
Catal. Rev. 10 (1974) 1.

/2/: Atomic and molecular oxygen adsorption on Ag(111).
C.T. Campbell
Surf. Sci. 157 (1983) 43.

/3/: Molecular adsorbed oxygen on metals: electron spectroscopic studies.
C.N.R. Rao, P.V. Kamath, S. Yashonath
Chem. Phys. Lett. 88 (1982) 13.

/4/: Theory of chemisorption.
editor: J.R. Smith
Springer-Verlag, 1980

/5/: The nature of the surface chemical bond.
editors: T.N. Rhodin, G. Ertl
North Holland Publishing Comp., 1979

/6/: Classical Electrodynamics.
J.D. Jackson
John Wiley and Sons, 1975.

/7/: Low energy electrons and surface chemistry.
G. Ertl, J. Kueppers
Verlag-Chemie, 1974

/8/: Introduction to photo-electron spectroscopy.
P.K. Gosh
John Wiley and Sons, 1983.

/9/: A simultaneous Energy and Angle resolved Ion Scattering Spectrometer.
G.J.A. Hellings, H. Ottevanger, S.W. Boelens, C.L.C.M. Knibbeler, H.H. Brongersma
Surf. Sci. 162 (1985) 913-920.

/10/: H.A. Kramers
Phil. Mag. 46 (1923) 836.

/11/: X-ray wavelengths.
J.A. Bearden
NYO-10586, U.S. Energy Commission
Oak Ridge Tennessee, 1964

/12/: Practical surface analysis by Auger and X-ray photo-electron spectroscopy.
editors: D. Briggs, M.P. Seah
Wiley and sons, 1983

/13/: Hartree-Slater subshell photoionization cross-sections at 1254 and 1487 eV.
J. Scofield
J. Electron Spectr. Rel. Phen. 8 (1976) 129.

/14/: A simplification of the Hartree-Fock method.
J.C. Slater
Phys. Rev. 81 (1951) 385.

/15/: T. Koopmans

Physica 1 (1933) 104.

/16/: Photo-electron and Auger spectroscopy.
T.A. Carlson
Plenum Press, 1975.

/17/: Binding energies and chemical shifts in ESCA.
U. Gelius
Physica Scripta 9 (1974) 133-147.

/18/: D.J. Kennedy, S.T. Manson
Phys. Rev. A5 (1972) 237

/19/: Relative intensities in photoelectron spectroscopy of atoms and molecules.
R.F. Reilman, A. Msezane, S.T. Manson
J. Electron Spectr. Rel. Phen. 8 (1976) 389-394.

/20/: Quantitative chemical analysis by ESCA.
D.R. Penn
J. Electron Spectr. Rel. Phen. 9 (1976) 29.

/21/: Electron mean free paths for free-electron-like materials.
D. R. Penn
Phys. Rev. B13 (1976) 5248-5254.

/22/: Attenuation lengths of low energy electrons in solids.
C.J. Powell
Surf. Sci. 44 (1974) 29.

/23/: Quantitative electron spectroscopy of surfaces: a standard base for inelastic mean free paths in solids.
M.P. Seah, W.A. Dench
Surf. Interf. Anal. 1 (1979) 2.

/24/: Inelastic effects in photo-emission: microscopic formulation and qualitative discussion.
C. Caroli, D. Lederer-Rozenblatt, B. Roulet, D. Saint-James
Phys. Rev. B8 (1973) 4552-4569.

/25/: The energy dependence of the electron mean free path.
C.D. Wagner, L.E. Davis, W.M. Riggs
Surf. Interf. Anal. 2 (1980) 53.

/26/: Energy and material dependence of the inelastic mean free paths of low energy electrons in solids.
C.J. Powell
J. Vac. Sci. Techn. A3 (1985) 1338.

/27/: DMA-report 311, march 1982
National Physics Laboratorium
M.P. Seah, M.T. Anthony.

/28/: Quantitative photo-electron spectroscopy as applied to non-ideal surfaces.
H.P.C.E. Kuipers
Solid State Ionics 16 (1985) 15.

/29/: Inelastic background and peak area determination in X-ray Photoelectron Spectroscopy (ESCA).
A. Proctor, D.M. Hercules
Appl. Spectr. 38 (1984) 505.

/30/: High resolution Photo-emission spectrum of the valence band of gold.

D.A. Shirley
Phys. Rev. B5 (1972) 4709.

/31/: The quantitative analysis of surfaces by XPS: a review.
M.P. Seah
Surf. Interf. Anal. 2 (1980) 222-239

/32/: Non-destructive in-depth composition information from XPS.
S. Tougaard
Surf. Sci. 172 (1986) L503-506.

/33/: Composition depth information from the inelastic background signal in XPS.
S. Tougaard
Surf. Sci. 162 (1985) 875-885

/34/: Concentration depth profiles by XPS: a new approach.
S. Tougaard, A. Ignatiev
Surf. Sci. 129 (1983) 355-365.

/35/: The adsorption of molecular oxygen species on Ag(110).
M.A. Barteau, R.J. Madix.
Surf. Sci. 97 (1980) 101.

/36/: Adsorption of oxygen on Ag(110) studied by high resolution ELS and TPD.
C. Backx, C.P.M. de Groot, P. Biloen
Surf. Sci. 104 (1981) 300.

/37/: The interaction of O2, CO and CO2 with Ag(110).
C.T. Campbell, M. Paffet
Surf. Sci. 143 (1984) 517.

/38/: Basic studies of the oxygen surface chemistry of silver chemisorbed atomic and molecular species on pure Ag(111).
R.B. Grant, R.M. Lambert
Surf. Sci. 146 (1984) 256

/39/: The effect of lateral interactions on the desorption of oxygen from Ag(110).
M. Bowker
Surf. Sci. 100 (1980) L472

/40/: H.P.C.E. Kuipers, private communications

/41/: Adsorption of oxygen on silver single crystal surfaces.
A. Engelhardt, D. Menzel
Surf. Sci. 57 (1976) 591.

/42/: Adsorption on silver single crystals
I. Oxygen on Ag(110).
M. Bradshaw, A. Engelhardt, D. Menzel
Ber. Buns. Ges. 76 (1972) 500.

/43/: Oxygen adsorption on (110) silver.
W. Heiland, F. Iberl, E. Taglauer, D. Menzel
Surf. Sci. 53 (1975) 383.

/44/: W. Heiland, E. Taglauer
J. Vac. Sci. Techn. 9 (1972) 620.

/45/: Chemisorption of oxygen on the silver (110) surface.
G. Rovida, F. Pratesi
Surf. Sci. 52 (1975) 542.

/46/: Oxygen adsorption on Ag(111) in the temperature range from 100-500 K: UPS, XPS and EELS investigations.
C. Benndorf, M. Francke, F. Thieme
Surf. Sci. 128 (1983) 417.

/47/: An XPS study of the kinetics of CO oxidation over Ag(111).
T.E. Felter, W.H. Weinberg, G. Ya. Lastushkina, A.I. Boronin, P.A. Zhdan, G.K. Boreskov, J. Hrbek
Surf. Sci. 118 (1982) 369.

/48/: Ellipsometry-LEED study of oxygen adsorption and the CO-oxygen interaction on Ag(110).
H. Alberts, W.J.J. v.d. Wal, O.L.J. Gijzeman, G.A. Bootsma
Surf. Sci. 77 (1978) 1.

/49/: Chemisorption of oxygen on the silver (111) surface.
G. Rovida, F. Pratesi, M. Maglielta, E. Ferroni
Surf. Sci. 43 (1974) 230.

/50/: Interaction of O2, CO2, C2H4 and C2H4O with Ag(110).
C. Backx, C.P.M. de Groot, P. Biloen, W.M.H. Sachtler
Surf. Sci. 128 (1983) 81-103.

/51/: A study of the adsorption of oxygen on silver at high pressure by electron spectroscopy.
R.W. Joyner, M.W. Roberts
Chem. Phys. Lett. 60 (1979) 459.

/52/: The co-adsorption of sodium and oxygen on Ag(100): an XPS, UPS and HREELS study.
E.L Garfunkel, X. Ding, G. Dong, S. Yang, X. Hou, X. Wang
Surf. Sci. 164 (1985) 511.

/53/: An XPS study of the adsorption of oxygen on silver and platinum covered with potassium or caesium.
M. Ayyoob, M.S. Hedge
Surf. Sci. 133 (1983) 516.

/54/: Cs-promoted Ag(111): Model studies of selective ethylene epoxidation catalysts.
C.T. Campbell
J. Phys. Chem. 89 (1985) 5789.

/55/: Alkali-metal promotors and catalysis: a single crystal investigation of ethylene epoxidation on Cs doped Ag(111).
R.B. Grant, R.M. Lambert
Langmuir 1 (1985) 29.

/56/: Basic studies of the oxygen surface chemistry on silver: oxygen, dioxygen, oxide and superoxide on Rb dosed Ag(111).
P.J. Goddard, R.M. Lambert
Surf. Sci. 107 (1981) 519.

/57/: Oxidation of lithium monolayers on Ag(111).
S.D. Parker, G.E. Rhead
Surf. Sci. 167 (1986) 271.

/58/: An XPS and UPS study of the interaction of oxygen with sodium dosed Ag(110).
D. Briggs, R.A. Marbow, R.M. Lambert
Surf. Sci. 65 (1977) 314.

/59/: Basic studies of the oxygen chemistry on silver: oxygen, dioxygen and superoxide on potassium dosed Ag(100).
M. Kitson, R.M. Lambert

Surf. Sci. 109 (1981) 60.

/60/: Smoothing and differentation of data by simplified least squares procedures.
A. Savitzky, M.J.C. Golay
Anal. Chem. 36 (1964) 1627.

/61/: The transition from physisorbed to chemisorbed oxygen on silver films studied by photoemission.
J. Eickmans, A. Otto, A. Goldmann
Surf. Sci. 149 (1985) 293-312.

/62/: Photoelectron spectra of adsorbed carbonates.
M.A. Barteau, R.J. Madix
J. Electron Spectr. Rel. Phen. 31 (1983) 101-108.

/63/: XPS and UPS studies of the interaction of CO with adsorbed oxygen on Ag covered with K, Ba and Cs.
M. Ayyoob, M.S. Hedge
J. Chem. Soc., Faraday Trans. I 80 (1984) 2703

/64/: Handbook of X-ray photoelectron spectroscopy.
C.D. Wagner, W.M. Riggs, L.E. Davis, J.F. Moulder
editor: G.E. Muilenberg
Perklin-Elmer Corporation, Minnesota 1979.

/65/: P.A Redhead
Vacuum 12 (1963) 203.

Calculation of the IMFP of photo-electrons in an oxygen overlayer.

The IMFP in SiO2 is well known to be 2.5- 3.0 nm from semi-conductor industry. From this relatively well known value an estimation can be made for the IMFP in an oxygen overlayer on silver.

The bulk density $\rho$ of SiO2 depends on its crystalline form but can be taken as 2500 kg/m$^3$. The approximate oxygen-oxygen distance d in SiO2 can then be evaluated from:

$$(a.1) \qquad d^3 = \frac{M}{2\ \rho\ Na}$$

with M the molecule mass of SiO2 (0.0601 kg) and Na Avogadro's number (6 $10^{23}$). In this calculation we have neglected the Si atom space occupation which is reasonable because of its small ionic radius (0.041 nm) compared to that of oxygen (0.14 nm).

The silver-silver distance on a (111) surface is 0.272 nm which is also the oxygen-oxygen distance in an oxygen overlayer if we assume one oxygen atom per silver atom.

According to SEAH /23/ the functional dependence between t and $\lambda$ is:

$$(a.2) \qquad \lambda^2 \propto d^3$$

Thus for an oxygen overlayer on Ag(111), $\lambda$ may be taken as ca. 3.0 nm.